uOttawa

L'Université canadienne
Canada's university

FACULTÉ DES ÉTUDES SUPÉRIEURES ET POSTOCTORALES

uOttawa

L'Université canadienne
Canada's university

FACULTY OF GRADUATE AND POSDOCTORAL STUDIES

Thushan Pathmalingam
AUTEUR DE LA THÈSE / AUTHOR OF THESIS

M.Sc. (Chemistry)
GRADE / DEGREE

Department of Chemistry
FACULTÉ, ÉCOLE, DÉPARTEMENT / FACULTY, SCHOOL, DEPARTMENT

Systematic Approach to the Development and Synthesis of Multi-nuclear Complexes Possessing Novel Magnetic Behavior
TITRE DE LA THÈSE / TITLE OF THESIS

M. Murugesu
DIRECTEUR (DIRECTRICE) DE LA THÈSE / THESIS SUPERVISOR

CO-DIRECTEUR (CO-DIRECTRICE) DE LA THÈSE / THESIS CO-SUPERVISOR

A. Beauchemin

S. Barry

Gary W. Slater
Le Doyen de la Faculté des études superieures et postdoctorales / Dean of the Faculty of Graduate and Postdoctoral Studies

A Systematic Approach to the Development and Synthesis of Multi-nuclear Complexes Possessing Novel Magnetic Behaviour

By

Thushan Pathmalingam

A thesis submitted to the School of Graduate Studies and Research

In Partial Fulfillment of the Requirements for the Degree of Master of Science

Ottawa-Carleton Chemistry Institute
Department of Chemistry
University of Ottawa
Ottawa, Ontario, Canada

August 2010

Candidate

Thushan Pathmalingam

uOttawa
L'Université canadienne
Canada's university

Supervisor

Dr. Muralee Murugesu

Library and Archives
Canada

Published Heritage
Branch

395 Wellington Street
Ottawa ON K1A 0N4
Canada

Bibliothèque et
Archives Canada

Direction du
Patrimoine de l'édition

395, rue Wellington
Ottawa ON K1A 0N4
Canada

Your file Votre référence
ISBN: 978-0-494-73773-6
Our file Notre référence
ISBN: 978-0-494-73773-6

NOTICE:

The author has granted a non-exclusive license allowing Library and Archives Canada to reproduce, publish, archive, preserve, conserve, communicate to the public by telecommunication or on the Internet, loan, distribute and sell theses worldwide, for commercial or non-commercial purposes, in microform, paper, electronic and/or any other formats.

The author retains copyright ownership and moral rights in this thesis. Neither the thesis nor substantial extracts from it may be printed or otherwise reproduced without the author's permission.

AVIS:

L'auteur a accordé une licence non exclusive permettant à la Bibliothèque et Archives Canada de reproduire, publier, archiver, sauvegarder, conserver, transmettre au public par télécommunication ou par l'Internet, prêter, distribuer et vendre des thèses partout dans le monde, à des fins commerciales ou autres, sur support microforme, papier, électronique et/ou autres formats.

L'auteur conserve la propriété du droit d'auteur et des droits moraux qui protège cette thèse. Ni la thèse ni des extraits substantiels de celle-ci ne doivent être imprimés ou autrement reproduits sans son autorisation.

In compliance with the Canadian Privacy Act some supporting forms may have been removed from this thesis.

While these forms may be included in the document page count, their removal does not represent any loss of content from the thesis.

Conformément à la loi canadienne sur la protection de la vie privée, quelques formulaires secondaires ont été enlevés de cette thèse.

Bien que ces formulaires aient inclus dans la pagination, il n'y aura aucun contenu manquant.

Canada

Table of Contents

1.3 Magnetism

List of Figures

List of Tables

List of Abbreviations

OEC	Oxygen Evolving Complex
SMM	Single-Molecule Magnet
D	zero- field splitting parameter
S	Spin ground state
U	Energy barrier
SCM	Single-Chain Magnet
Me	Methyl
Et	Ethyl
Ph	Phenyl
MeOH	Methanol
EtOH	Ethanol
MeCN	Acetonitrile
iPrOH	Isopropanol
$CHCl_3$	Chloroform
DCM	dichloromethane
DMF	Dimethyl formamide
DMA	Dimethyl amide
H_2dho	1-hydroxypropan-2-one oxime
H_2dmo	3-hydroxy-3-methylbutan-2-one oxime
H_2deo	3-ethyl-3-hydroxypentan-2-one oxime
H_2cpo	1-(1-hydroxycyclopentyl)ethanone oxime
H_2dpo	1-hydroxy-1,1-diphenylpropan-2-one oxime
Hndo	1-(dimethylamino)propan-2-one oxime
H_2salox-H	2-hydroxybenzaldehyde oxime
H_2salox-Me	1-(2-hydroxyphenyl)ethanone oxime
H_2salox-Et	1-(2-hydroxyphenyl)propan-1-one oxime
H_3oxol	2,5-dihydroxy-2,5-dimethylhexan-3-one oxime
H_3tri-ox	(1-(bis((E)-2-(hydroxyimino)propyl)amino)propan-2-one oxime
NH_2OH	Hydroxylamine
$Mn(ClO_4)_2$	Manganese perchlorate
$Mn(CH_3COO)_2$	Manganese acetate
$Mn(Cl)_2$	Manganese chloride
$Mn(Br)_2$	Manganese bromide
Et_3N	Triethylamine
Et_4NOH	Tetraethylammonium hydroxide
NaOH	Sodium hydroxide
NaOMe	Sodium methoxide
XRD	X-Ray Diffraction

Additional Information

Mn(II)	Yellow ball
Mn(III)	Violet ball
Mn(IV)	Green ball
Sodium	Cyan ball
Oxygen	Red ball
Nitrogen	Blue ball
Chlorine	Green ball
Carbon	Omitted
Jahn-Teller axis	Bold bonds

Contributions:

- Tara Burchell solved crystal structures for complexes **1** – **2**, **4** – **21** and Ilia Korobkov for **3.**
- Rodolphe Clerac performed magnetic measurements and calculations on **1 – 2**, **4 – 11** and **14 – 18.**
- Serge Gorelsky for the DFT calculations on **1**.

Abstract

The chapters in this thesis are sequentially arranged in increasing nuclearity and atomic configuration (i.e. linear Mn_3, triangular Mn_3, Mn_6, Mn_7, Mn_9, Mn_{18}, and Mn_{23}). In order to synthesize these molecules tuneable, multi-dentate oximate ligands were employed. These compounds were characterized exclusively by X-ray crystallography and their magnetic properties by SQUID measurements. The latter permits us to determine the spin ground state and the magnetic anisotropy and hence ultimately establish whether the molecules exhibit the single-molecule magnet (SMM) behaviour. In addition to the atomic structure, a magneto-structural correlation was conducted for the 21 manganese clusters. In an attempt to achieve high energy barrier SMMs two essential requirements; large spin ground state and uniaxial magnetic anisotropy were manipulated. Each chapter was discussed in regards to achieving SMM behaviour by tweaking one or both requirements. There are two basic magnetic repeating units which lay the foundation for large Mn aggregates; linear Mn_3 and triangular Mn_3. The former can be used to produce linear 1-D chains of Mn_3 polymer. The latter can be used to synthesize Mn_6, Mn_7, Mn_9, Mn_{18} and Mn_{23} clusters.

Fundamental Unit	Larger Aggregates
▬▬ **Linear Mn_3 unit**	1-D $NaMn_3$
▲ **Triangular Mn_3 unit**	Mn_6 Mn_7 Mn_9 Mn_{18} Mn_{23}

Chapter 1

1.1 Introduction

There is a continuous need for inorganic chemists to engineer new molecular materials which exhibit unique magnetic behaviour based on transition metal complexes with wide variety of implications.[1] More specifically, manganese has been the metal of choice in this field due to the intrinsic magnetic properties which arise from the d^7 valence electrons.[2] In order to generate a cluster or aggregate of metal ions, a bridging ligand is required. These bridging units are generally derived from oxygen donors such as oxides, hydroxides, alkoxides, and carboxylate as well as nitrogen donors, such as amines and amides. Carboxylate moieties are one of the most studied bridging ligands in manganese chemistry.[3] This thesis exclusively explores the combination of both oxygen and nitrogen donor ligands, namely oximes (-NO) to generate metal aggregates. These bridging ligands allow the metal ions to communicate through a magnetic exchange coupling pathway by means of orbital overlap. The two basic magnetic repeating units that lay the foundation for self-assembly of larger Mn clusters in this thesis are linear Mn_3 and triangular Mn_3. The latter can be used to synthesize Mn_6, Mn_7, Mn_9, Mn_{18} and Mn_{23} clusters. These compounds were designed in the pursuit of high energy barrier single-molecule magnets (SMMs). The two essential requirements for observing SMM behaviour in small molecules is large spin ground state and uniaxial magnetic anisotropy.[4] Each chapter will be discussed in regards to achieving SMM behaviour by manipulating one or both requirements. As a magneto-chemist, it is essential to understand how the magnetic behaviour arises, as well as how to synthetically control and target the crystal growth at the molecular level.

1.2 Manganese Coordination Chemistry

Manganese is the third most abundant transition metal on the earth's crust and exists as Mn(II) aqua ions in sea water. In minerals, it is found as oxides, such as pyrolusite ($Mn^{IV}O_2$), hausmannite ($Mn^{II/III}{}_3O_4$), and rhodochrosite ($MnCO_3$).[5] Manganese is an essential trace nutrient in all forms of life. Manganese-containing polypeptides include arginase, the diphtheria toxin and superoxide dismutase (Mn-SOD).[6] The Mn-SOD enzyme is present in all organisms living in an aerobic environment, using it to deal with the toxic effects of superoxide. Mother nature has also incorporated manganese into cyano-bacterial, algae and higher plant species which can catalyze the oxidation of water into dioxygen species.[7] The splitting of water molecules to molecular oxygen is catalyzed by the oxygen evolving complex (OEC) which is located in the photo-system II protein. There are numerous models proposed for the OEC (i.e. the cubane[8], 3+1[9] and 2+2[10] model).

In an ever growing high-tech industry, magnetic materials play a critical role in our lives and therefore it is important to understand the basic concepts of magnetism. Magnetism was first discovered by the ancient Greeks and was used as a compass for navigational purposes.[11] Since then, magnetic materials have been widely used in medical devices, magnetic separators, loudspeakers, microphones, sensors, and data storage devices. Traditional magnetic materials are typically composed of three-dimensional arrays of atoms or ions i.e. transition metal or mixed metals containing the spin units.

Manganese lies at the top of the group VII elements on the periodic table. It contains two *s* electrons outside the 3*d* shell with five electrons. It can readily form Mn(II) ion with the removal of the 4*s* electrons. Manganese has rich redox chemistry with several accessible oxidation states ranging from one to seven. The most common geometry for the Mn(III) ion is Jahn-Teller distorted octahedral (D_{4h}) or square pyramidal (C_{4v}). The arrangement of electrons in Mn(III) d^4 for various geometries is shown in Figure 1.

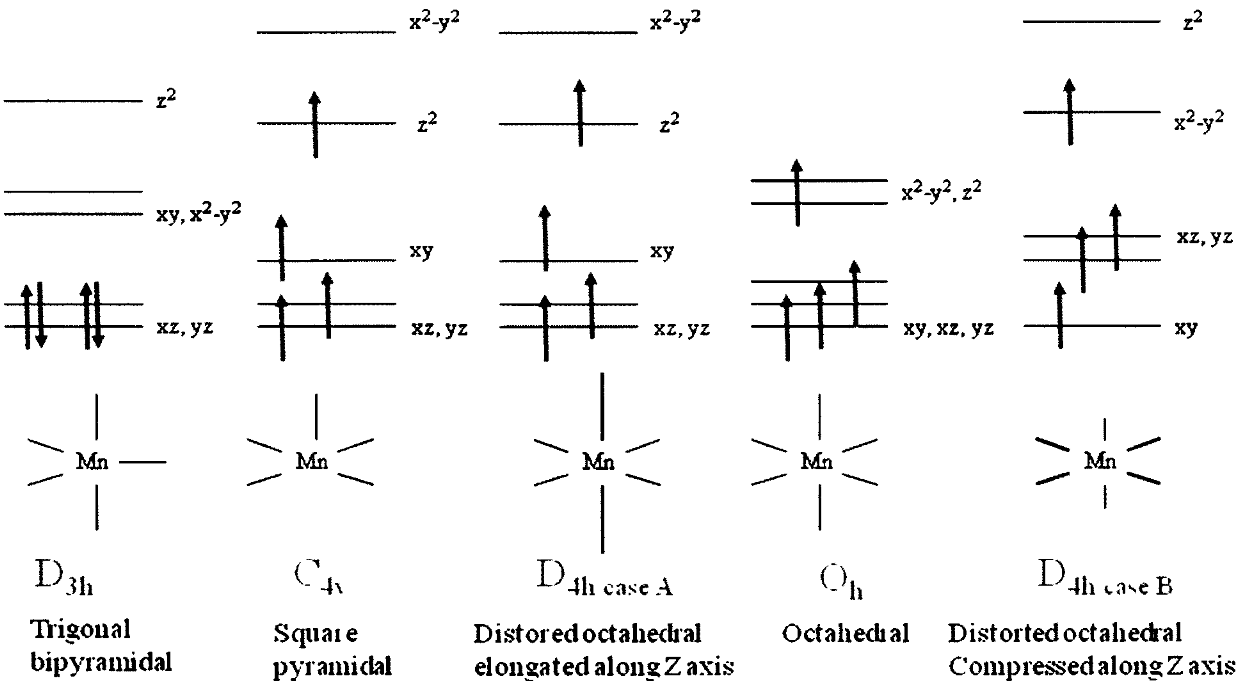

Figure 1. The arrangement of electrons in Mn(III) d^4 for various geometries. In case A the metal to ligand distances are shorter in the *xy* plane and in case B it's shorter in the *z* axis.

The work presented in this thesis focuses on the synthesis and characterization of novel multi-nuclear complexes of manganese. This work is conducted in pursuit of innovative magnetic materials (i.e. single-molecule magnets). The prerequisite of these materials is the unpaired electrons which are obtained from the transition metals and the nature of interaction between metal ions.

1.3 Magnetism

There are two fundamental types of magnetism on the atomic level; diamagnetism and paramagnetism.[12] All of the complex magnetic behaviour arises from either one of these. All atomic and molecular materials exhibit some form of diamagnetic behaviour with the exception of the hydrogen radical. Diamagnetism is characterized by repulsion of a substance out of an applied magnetic field. This behaviour arises from the interaction of the paired electrons with the magnetic applied field. Diamagnetic susceptibility is independent of the temperature and the strength of the applied field. Paramagnetism, on the other hand, is characterized by the attraction of a substance into an applied magnetic field. This behaviour arises as a result of the interaction of the unpaired electrons of the molecular orbital with the applied magnetic field. Typically, paramagnetic materials contain one or more unpaired electrons and the strength of interactions are temperature dependent. The non-zero spin angular moment associated with the unpaired electrons gives rise to the magnetic moment. The bulk magnetic properties result from a long range interaction of the unpaired electrons between the paramagnetic atoms. The consequence of these interactions is materials that are either magnetic or non-magnetic depending on the alignment and proximity of the spin units.

1.3.1 Classes of Magnetism

Bulk magnetic behaviour can essentially be explained using one of the four primary classes of magnetisms; paramagnetism, ferromagnetism, anti-ferromagnetism, and ferrimagnetism. These four classes are derived from the interaction of the adjacent magnetic spin units at absolute zero as shown in Figure 2.

In paramagnetism, the spins of the electrons are not influenced by the neighbouring electrons, thus not altering the magnetic moment. Upon applying a magnetic field, the spin units will align in a certain orientation and in the absence of the applied field, the spins will randomize due to weak coupling of the electron atomic orbitals. In Ferromagnetism, the spins of the electrons are aligned in a parallel fashion resulting in a net magnetic moment. In an antiferromagnet, the spins of the electrons are aligned in an anti-parallel fashion resulting in no net magnetic moment. At absolute zero, the antiferromagnets exhibit diamagnetic behaviour in an applied magnetic field. Antiferromagnetism is the commonly observed type of magnetism in bulk materials. Ferrimagnets are a special case of antiferromagnets, however they contain alternating spins of different magnitude, resulting in a net magnetic moment.

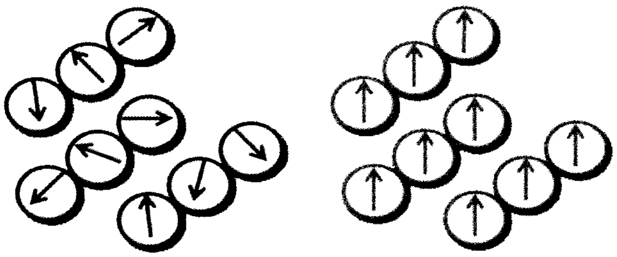

Paramagnet Ferromagnet

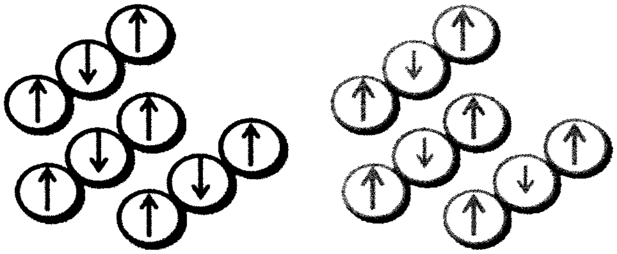

Antiferromagnet Ferrimagnet

Figure 2. Depiction of the magnetic moment alignment for the four principal classes of magnetism.

1.3.2 Temperature Dependence of Magnetization

Magnetic interactions can be characterized by their responses to variations in temperature and applied magnetic field. Each of the four principal classes of magnetism has a characteristic response curve giving information about the type and strength of the magnetic interaction. Magnetic susceptibility (χ) is a quantitative measure of the response of a material to an applied magnetic field and is described using equation 1, where M is magnetization and H is the applied field.

$$\chi = \frac{M}{H} \qquad \text{Eq. 1}$$

The magnetic properties of a material can be examined using the magnetic susceptibility measurement as a function of the temperature as shown in Figure 3. It is difficult to determine whether the material is para- or ferromagnetic using this technique. This problem can be solved by examining the magnetic susceptibility product as a function of temperature which clearly specify the various types of magnetic behaviour (Figure 4).

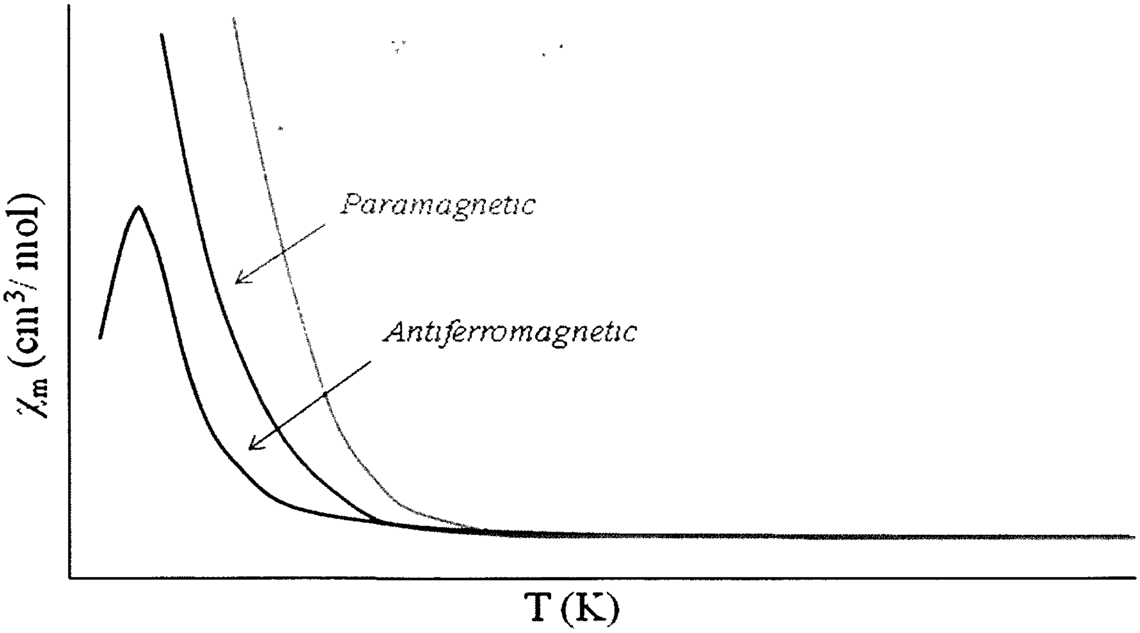

Figure 3. Magnetic susceptibility as a function of temperature for the three types of magnetic material.

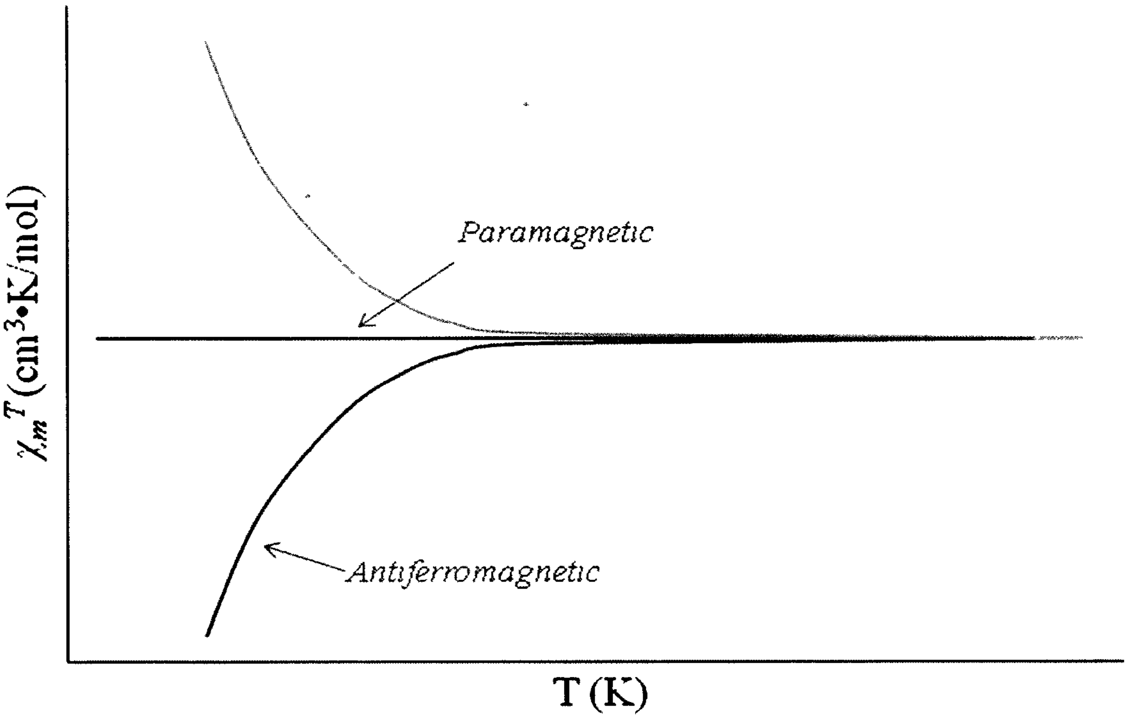

Figure 4. Plot of the magnetic susceptibility product as a function of temperature for the three classes of magnetism.

1.4 Single-Molecule Magnets

Bulk magnets have existed for ages and are known to consist of 3-D lattices of metallic alloys or metal oxides. However, the development of magnetic materials based on a molecular bottom-up approach is much more recent. This approach involves the construction of cluster molecules composed exclusively of metal ions and organic molecules. For the past two decades, there has been a growing interest in the field of molecular-based magnets; specifically in the development of single molecule magnets (SMMs).[13] Potential applications of SMMs include quantum computing, high-density information storage, and magnetic refrigeration. The behaviour of SMMs is derived and dictated by the intrinsic properties of the molecule as opposed to a traditional magnet, which is derived from the 3-D array of particles containing millions of spins.

SMMs are discrete molecules which exhibit the super-paramagnet-like property of slow magnetization relaxation and thus behave like magnets below the blocking temperature (< 5 K).[14] In order for a molecule to be classified as an SMM it must possess a large spin ground state *S*, which can be attained from the unpaired electrons of the metal centers and contain a significant anisotropy of the easy-axis (Ising type), with a large and negative zero-field splitting parameter (*D*). These two factors generate the energy barrier (*U*) for the reversal of magnetization vector, given by $S^2|D|$ and $(S^2 - 1/4)\ |D|$, for integer and half-integer *S* values, respectively[14] (Figure 5).

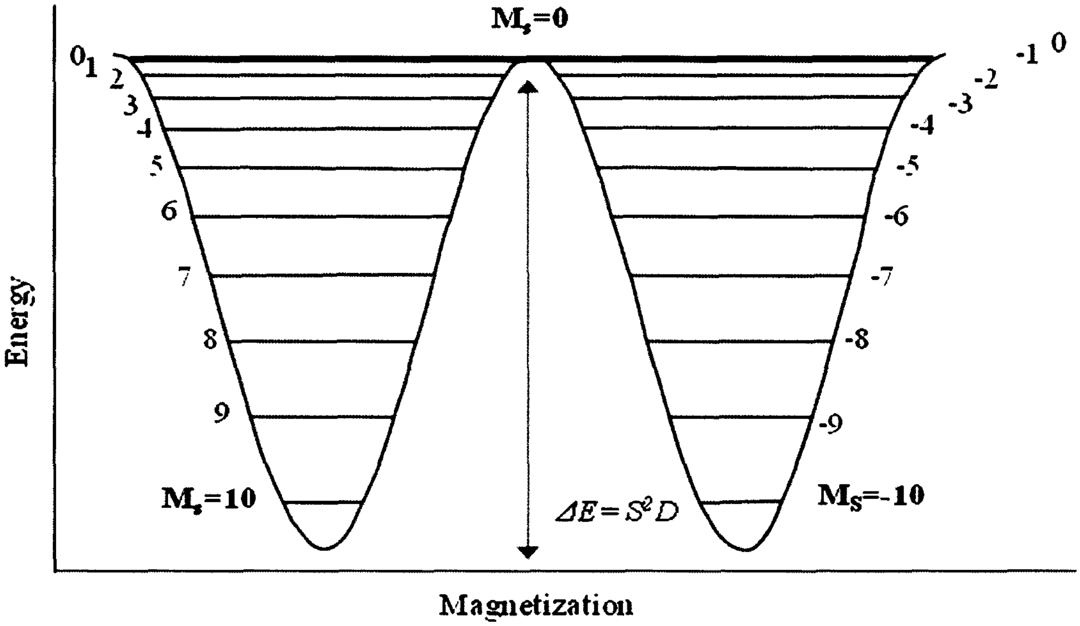

Figure 5. Bistability energy barrier for the magnetization in the absence of the magnetic field, between the spin 'up' ($M_S = 10$) and 'down' ($M_S = -10$) state.

One of the prerequisite for SMMs is the metal centers with unpaired electrons that establish magnetic exchange interactions resulting in a net spin. These interactions can be ferromagnetic, when they favour a parallel alignment of the spins, and anti-ferromagnetic when they favour an anti-parallel alignment. Large spin ground states in poly-nuclear complexes can be achieved by exclusively ferromagnetic interactions; however, they are most commonly encountered by a combination of ferro- and anti-ferromagnetic interactions. In this particular case the final alignment of the spins is the result of a compromise between the opposing exchange interactions. An excellent example of this phenomenon is shown with Mn_{12} Cluster (Figure 6); the first and most studied SMM to date.[15]

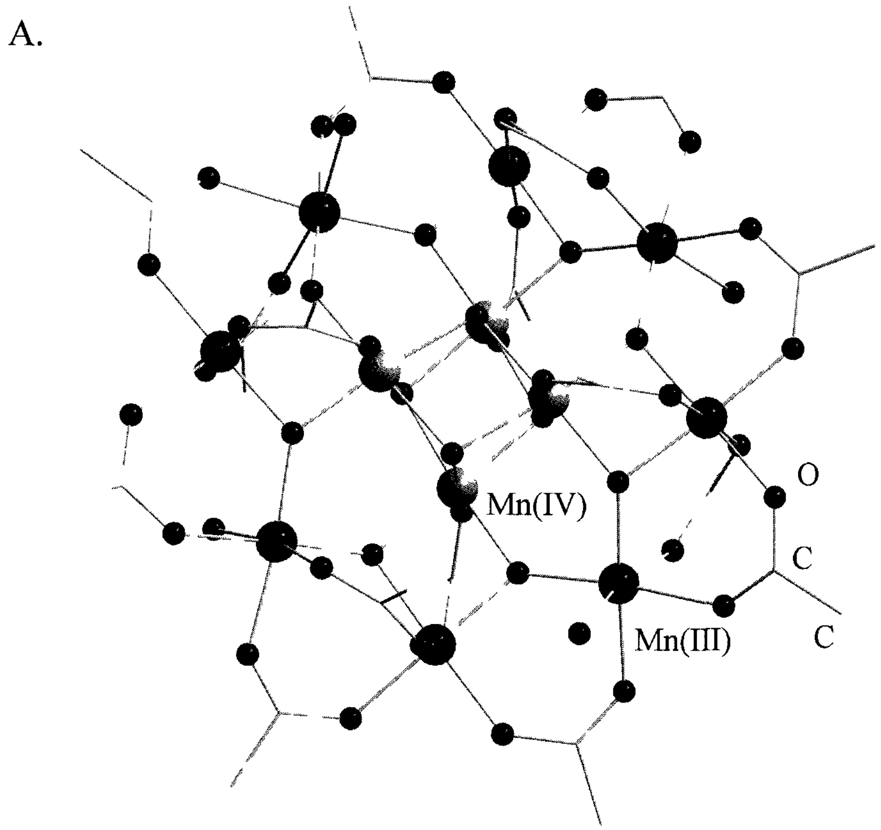

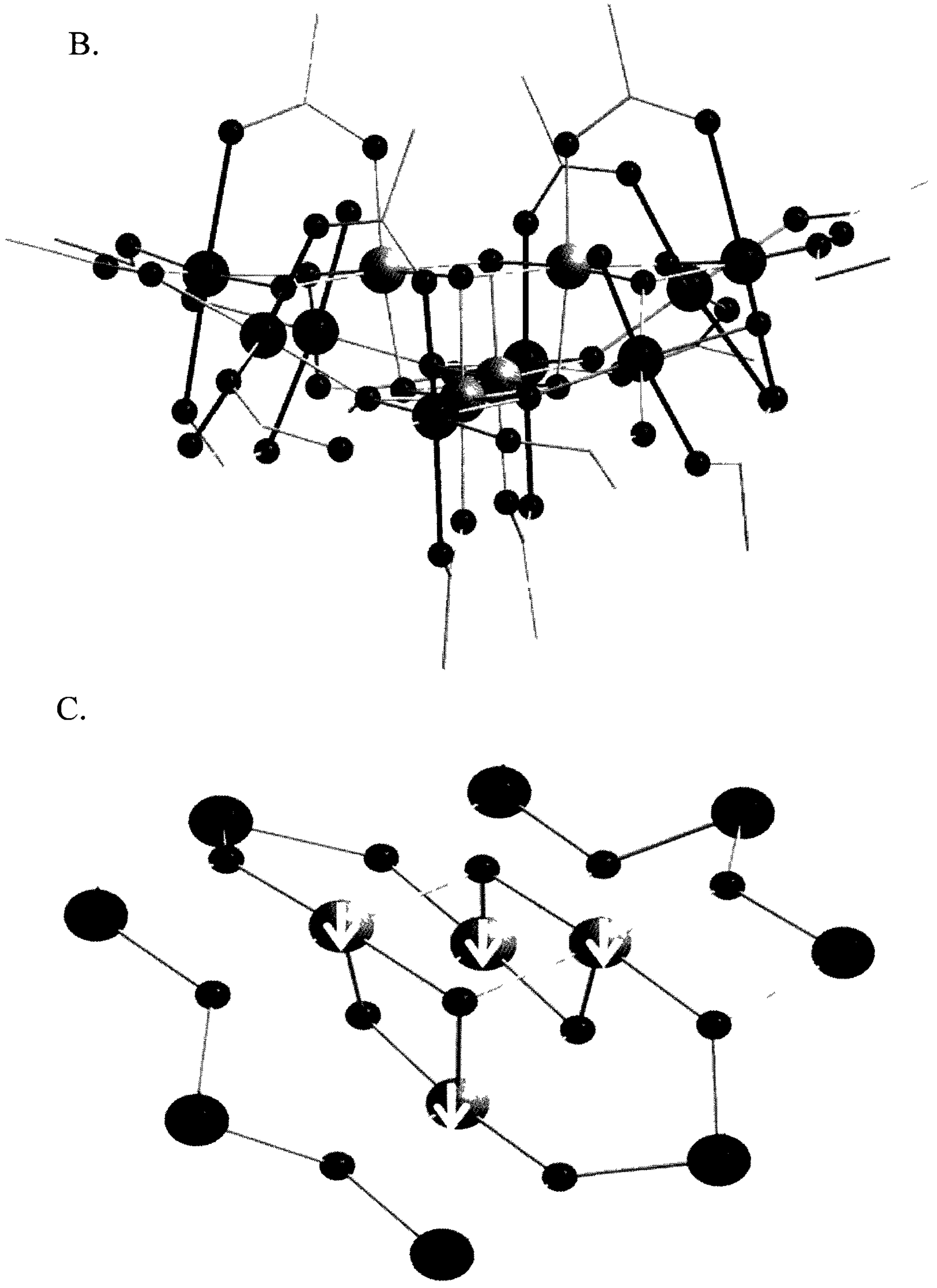

Figure 6. A. view of Mn_{12} along the *c* axis; B. view along the *b* axis; C. Core structure depicting the orientation of the spins on the metal centers. Colour code: Violet- Mn(III) , Green- Mn(IV) and Red- O. Bold bonds represent Jahn-Teller elongations.

In 1993, R. Sessoli et. al. reported a complex, $[Mn_{12}O_{12}(O_2CMe)_{16}(H_2O)_4]$, which exhibited the properties of a SMM.[15] Mn_{12} complex is comprised of eight Mn(III) ions, each contributing a spin of 2, and four Mn(IV) ions, each contributing a spin of 3/2. The outer core of the complex is arranged in a non-planar ring where the spin carriers, interconnected *via* μ_3-oxides, are ferromagnetically coupled to yield a spin ground state of 16. The organic component of the SMM is composed of peripheral acetate groups and water molecules as shown in Figure 6A. The inner core is arranged in a cubic fashion, where the Mn(IV) ions are ferromagnetically aligned to give an S = 6. The overall interaction between these two sets of Mn ions leads to an antiferomagnetic coupling to yield a net spin ground state, $S_T = 10$. All 8 Mn(III) ions are in high spin d^4 configuration with octahedral coordination geometry undergoing Jahn-Teller distortion. This distortion results in an elongation of the axial bond around the Mn(III) ions, giving rise to a large anisotropy. Approximately all of the elongated bonds are parallel, shown in black (Figure 6B), hence contributing to the sum of a large and negative easy axis type magnetic anisotropy for the entire molecule. For $H_z = 0$, the magnetic energy levels are labeled by the quantum number m_s ($-S < M_s < S$, where S = total spin), which represents the projection of S onto the easy axis. Therefore, in an energy barrier separating the spin "up" and "down" states, the magnitude of this barrier is approximately $|D| S^2$ (Figure 5). Due to this potential energy barrier, SMMs show slow magnetic relaxations at low temperatures. This behavior can be experimentally observed by the appearance of at least one frequency-dependent out-of-phase peak in the ac magnetic susceptibility plot (Figure 7) and of a hysteresis loop in the magnetization versus applied field scans.

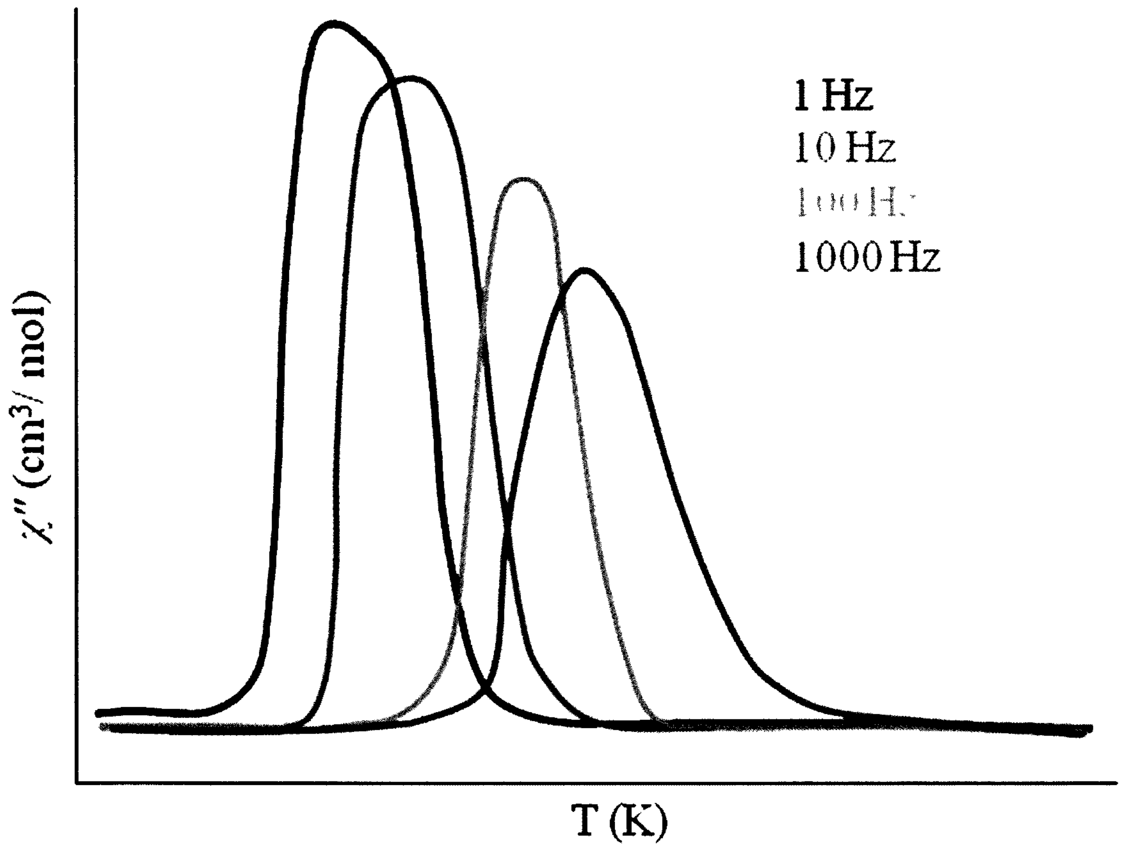

Figure 7. Arbitrary ac magnetic susceptibility *vs*. temperature plot showing the frequency dependence out-of-phase peaks for 1 to 1000 Hz.

1.5 Ligand Design

The objective of this research is to develop and synthesize multi-nuclear manganese complexes. In order to achieve this goal, an appropriate organic molecule must be designed to chelate, bridge, encapsulate and stabilize the inorganic core consisting of metals. The purpose of this approach is to increase the net spin ground state of the molecule by increasing the number of metal ions containing the spins of the electrons. In addition, the organic molecules allow the metal centers to communicate through the molecular orbitals; this is also known as the super-exchange pathway. The conventional organic ligands used in the literature are carboxylic acids, RCO_2H, such as acetates, benzoate, etc. After an extensive literature search, oximate-based ligands were found to be ideal for the formation of large metal aggregates. There are numerous factors to take into consideration when designing ligands: overall size, number of chelating sites, nature of chelating sites (O, N and S), and co-ordination strains (favouring five- or six-membered ring systems). With this in mind, oxime-based ligands were designed to incorporate the aforementioned factors to understand the magnetic correlations.

Using this synthetic strategy, we have investigated the use of tuneable, multi-dentate oximate-based chelating ligands. To date, the majority of previously reported oximate-based metal complexes have been synthesized using either commercially available ligands or those that have been prepared using Schiff base reactions. In order to gain controllability and tunability of the oximate ligands, we have used a new synthetic approach involving direct hydroamination of alkynes. The chosen oximate chelate has been carefully designed to incorportate various R groups on the alpha carbon to the oxime functional group (ligands I-V with R,R = H,H; Me,Me; Et,Et; cyclopentyl and Ph,Ph, respectively). This may influence the nature and strength of the magnetic interactions between the metal ions. Eleven oxime-based ligands were synthesized (with the exception of VII which is commercially available) and classified according to their coordination ring number, as shown in Figure 8. Class A (I- VI) and B (VII-IX) ligands are capable of forming five-membered and six-membered coordination rings with the metal ions, respectively. Class C (X- XI) ligands share the characteristics of class A and B ligands, where five- or six-membered coordination rings are possible (Table 1).

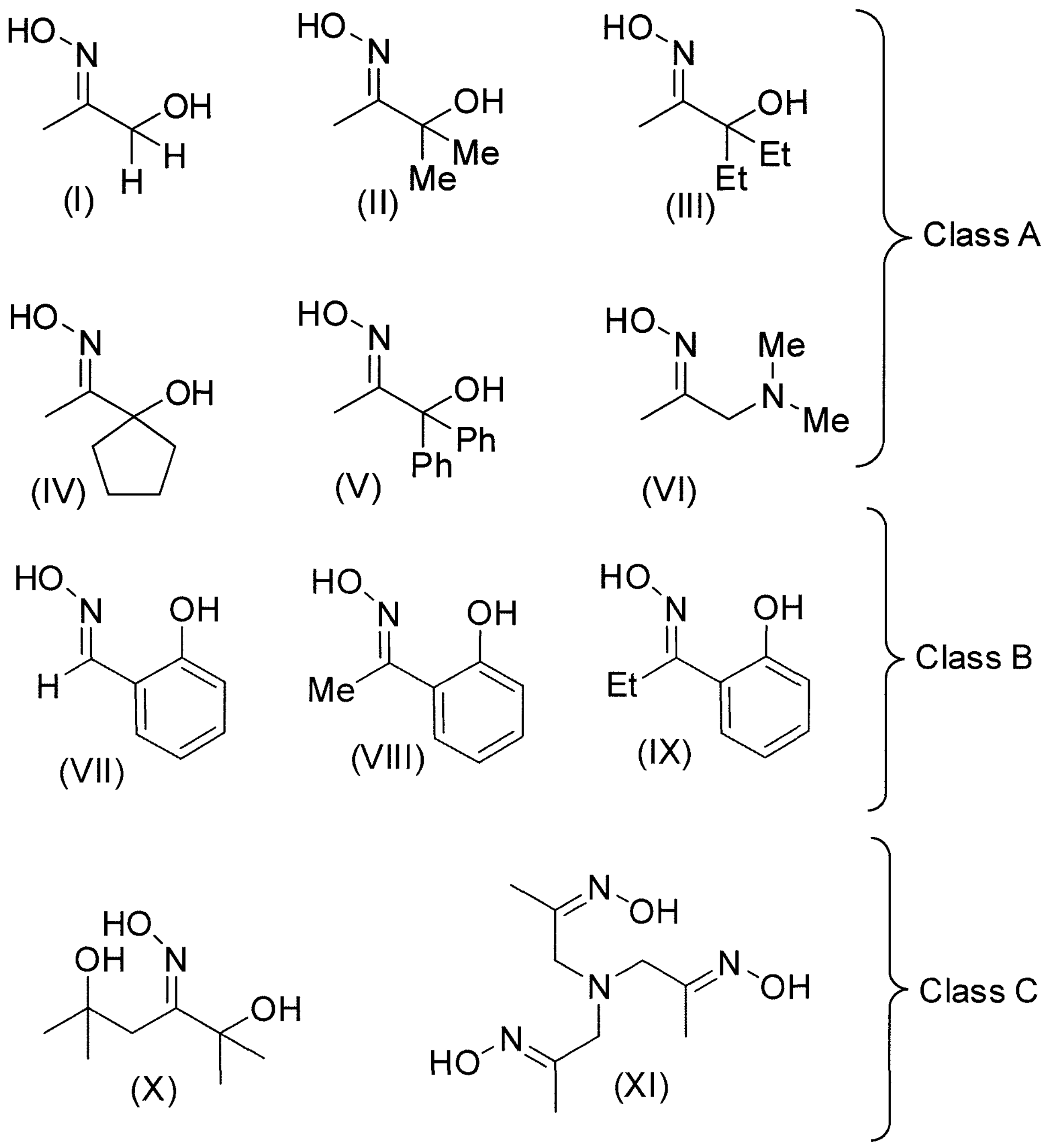

Figure 8. Oxime-based ligands I- XI divided into three classes: A, B and C according to their coordination ring number.

Table 1. Oxime ligands (I-XI) with the classification, full chemical name, abbreviations and the five- or six-membered coordination ring assignment.

Class	Ligand #.	Name	Abbrev.	coordination ring
A	I	1-hydroxypropan-2-one oxime	H_2dho	5
A	II	3-hydroxy-3-methylbutan-2-one oxime	H_2dmo	5
A	III	3-ethyl-3-hydroxypentan-2-one oxime	H_2deo	5
A	IV	1-(1-hydroxycyclopentyl)ethanone oxime	H_2cpo	5
A	V	1-hydroxy-1,1-diphenylpropan-2-one oxime	H_2dpo	5
A	VI	1-(dimethylamino)propan-2-one oxime	Hndo	5
B	VII	2-hydroxybenzaldehyde oxime	H_2salox-H	6
B	VIII	1-(2-hydroxyphenyl)ethanone oxime	H_2salox-Me	6
B	IX	1-(2-hydroxyphenyl)propan-1-one oxime	H_2salox-Et	6
C	X	2,5-dihydroxy-2,5-dimethylhexan-3-one oxime	H_3oxol	5 and 6
C	XI	1-(bis((E)-2-(hydroxyimino)propyl)amino)propan-2-one oxime	H_3tri-ox	5 or 8

Ligand I-VI, X and XI were obtained upon heating alkynol starting material as purchased with aqueous NH_2OH overnight (Table 2). The reaction proceeds with high Marknovnikov regioselectivity and can routinely be made on the gram-scale to afford the desired oxime.[16] The proposed mechanism involves the Cope-type hydroamination followed by bimolecular proton transfer (Figure 9). This novel synthetic strategy enables us to vary the R groups depending on the starting material. The oxime-based ligands appear to be promising materials for the formation of cluster complexes with numerous coordination capabilities. The schematic diagram below demonstrates the possible coordination modes of the ligand I to XI (Figure 10). The most interesting sites of coordination are the -NO bridge between the metal ions and we believe that these bridging heteroatom moieties may influence the magnetic interactions between the spin carriers because of the torsion angles. The latter influences the orbital overlap and as a result causing the ferro and antiferro interaction.

Table 2. Starting material for ligands I to VI and VIII to XI along with the yields.

Starting Material	Product	% Yield
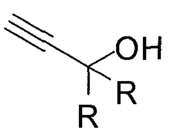	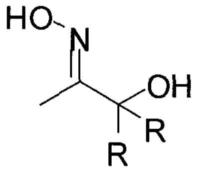 I-V	I- 84% II- 75% III- 74% IV- 81% V- 78%
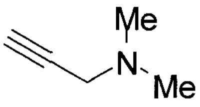	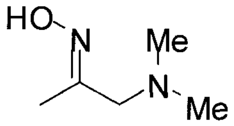 VI	71%
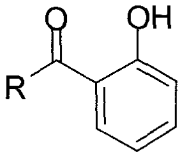	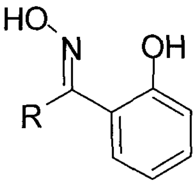 VIII- IX	VIII- 77% IX- 81%
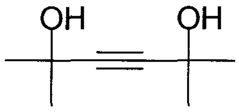	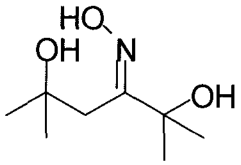 X	65%
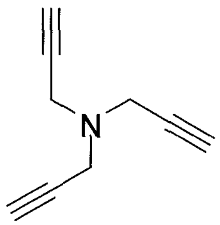	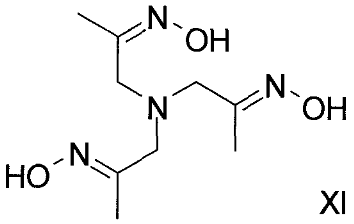 XI	60%

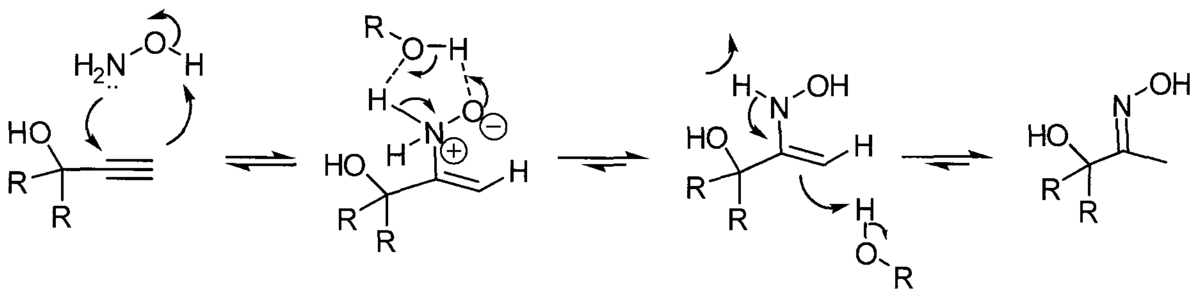

Figure 9. General reaction mechanism of hydroamination of alkynol.

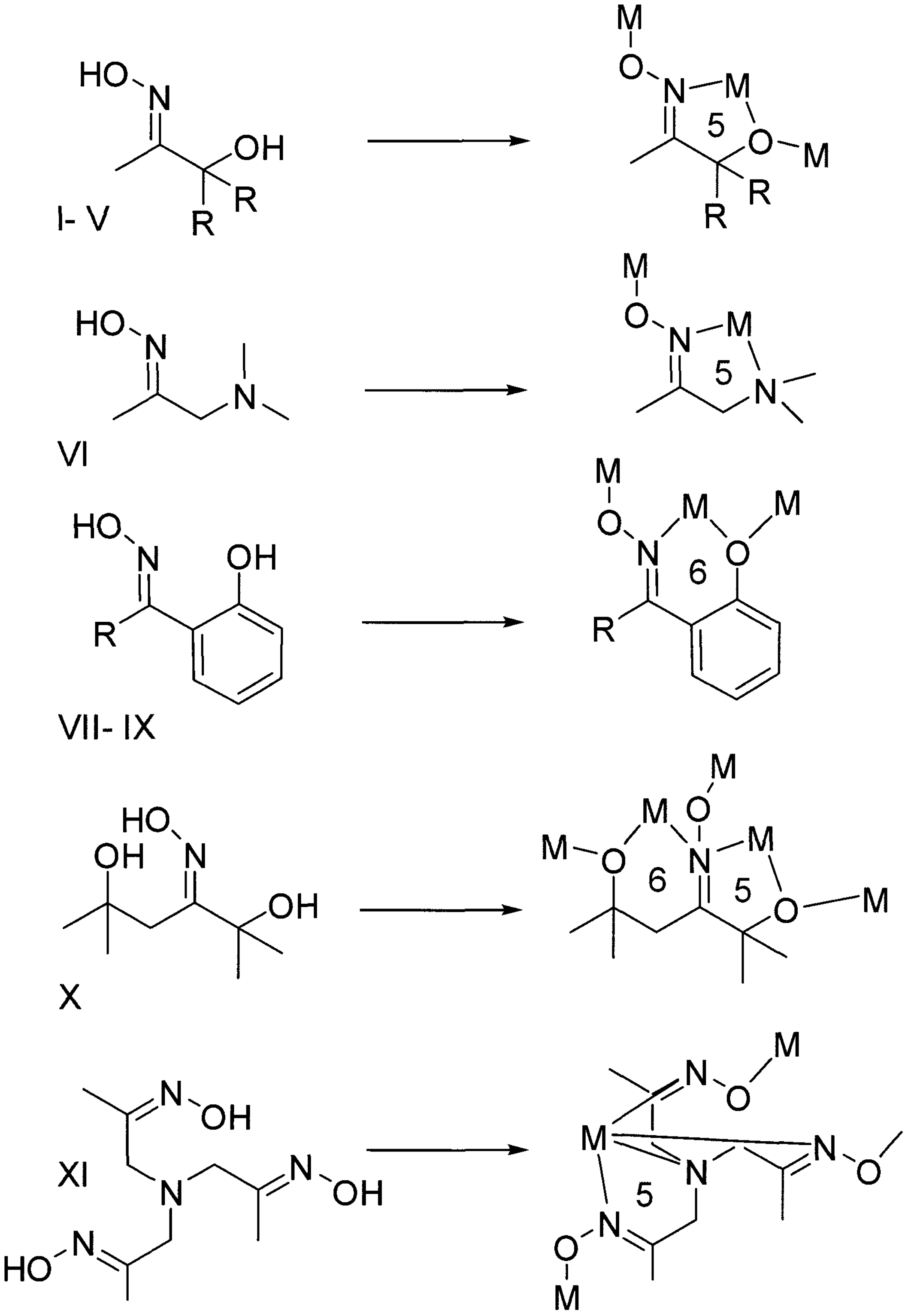

Figure 10. Possible coordination mode of the ligands depicting the five- or six- membered coordination rings.

1.6 Synthetic Strategy

The general synthetic strategy towards achieving multi-nuclear complexes was to use a poly-dentate ligand as mentioned in the previous section. To promote the coordination of the ligands to metal ions, triethylamine and/ or sodium hydroxide was required as a base. This allowed the deprotonation of the alcohol and oximate groups resulting in the coordination of the free metal cations to the ligand anions forming stable five- or six-membered coordination rings. Manganese (II) salts such as $Mn(ClO_4)_2$, $Mn(Cl)_2$, $Mn(CH_3COO)_2$, and $Mn(Br)_2$ were chosen as starting material to synthesize higher nuclearity complexes. The overall synthetic strategy is illustrated by the following equation:

$$\mathrm{Mn(anion)_2\bullet\, xH_2O + H_2L} \xrightarrow[\text{Solvent}]{\text{Base}} \mathrm{[Mn^{II\ or\ III\ or\ IV}{}_n(L)_n]\bullet\, xSolvent} \qquad \text{Eq. 2}$$

Multiple reactions were carried out in various solvents such as MeOH, EtOH, iPrOH, CH_2Cl_2, CH_3Cl_3, MeCN, DMF, DMA, toluene, benzene and diethyl ether. The reaction mixture was left undisturbed from days to weeks to allow the process of crystallization to occur. The objective of this approach is to obtain single crystals that are suitable for X-ray diffraction crystallography (XRD). XRD is a method used to determine the arrangement of atoms in a crystal. A crystal is defined as a solid material in which the atoms are arranged in a highly ordered repeating fashion forming a unit cell. In order to produce suitable crystals for XRD, the appropriate reaction conditions must be determined (i.e. metal : ligand : base ratio along with pure or mixed solvent ratio).

1.7 Thesis Overview

The upcoming chapters are arranged in increasing manganese nuclearity: linear Mn_3, triangular Mn_3, Mn_6, Mn_7, Mn_9, Mn_{18} and Mn_{23}. This thesis will demonstrate a designed approach to the synthesis and development of multi-nuclear complexes. Each chapter consists of one or more crystal structures which have been characterized structurally and magnetically. A magneto-structural correlation was obtained to understand the nature and strength of the interactions. As mentioned in Section 1.3, the essential ingredients for observing SMM behaviour in small molecules are large spin ground state and magnetic anisotropy. Each chapter will be discussed in detail with regards to achieving such behaviour by tweaking one or both parameters.

Chapter 2

2.1 Ferromagnetic Linear Mn_3 complexes

Three Mn_3 complexes arranged in a linear fashion will be discussed in detail with regards to the structural feature and magnetic behaviour in this chapter. The coordination chemistry of manganese is generally dominated by low-valent Mn(II), Mn(III) or mixed-valent Mn complexes in the literature. To date, only a handful of high-valent; Mn(IV), compounds have been synthesized, all of which contain O^{2-}, OH^- bridging ligands.[18] To our knowledge, no examples of exclusively chelating ligand bridged Mn(IV) polynuclear (n>2) complexes have been reported. This is presumably due to the difficulty of stabilizing Mn(IV) ions in the absence of a metal oxide core. An exclusively chelating ligand bridged high-valent complex, $[Mn^{IV}_3(dpo)_6]\cdot 2MeCN$, **1** has been synthesized in which all three Mn ions are ferromagnetically-coupled to exhibit an $S_T = 9/2$ spin ground state.[19] However, complex **1** does not exhibit SMM behaviour due to the absence of magnetic anisotropy, which generally arises from Mn(III) ions. In theory, this molecule has met the first requirement for an SMM, which is a high spin ground state but failed to meet the second; magnetic anisotropy. According to the DFT calculations it is possible to reduce the central Mn(IV) to Mn(III) and by doing so, introduce anisotropy to the linear system. In the quest to synthesize the reduced analog of **1**, class C ligand, H_3oxol was employed in the hopes of observing SMM behaviour. H_3oxol ligand contains two potential pockets of coordination sites, one forming five and the other six-membered rings. Complex **2**, $[Mn^{II}(imidazole)_4OH][Mn^{IV}_3(Hoxol)_6]\cdot MeOH$ was synthesized and characterized magnetically with $S_T = 9/2$ and exhibits no magnetic anisotropy. By switching the base from triethylamine to sodium hydroxide in the reaction condition complex **3**, $[Na[Mn^{III}Mn^{IV}_2(Hoxol)_6]\cdot MeOH\cdot H_2O]_n$

was synthesized. The linear Mn_3 units are linked by a sodium cation forming the 1-D chain. Theoretically, **3** has met both requirements for an SMM, with the central Mn(III) ion and the two peripheral Mn(IV) ions ferromagnetically coupled to yield an $S_T = 5$. Experimentally, **3** exhibited the properties of an SMM with a tail of a peak for ac magnetic susceptibility with an out of phase component.

2.2 Structure of $[Mn^{IV}_3(dpo)_6]{\bullet}2MeCN$, 1

In order to synthesize this unique complex we have developed an alternative approach, contrary to the common practice of utilizing strong oxidizing agents such as MnO_4^- in acidic conditions which lead to oxo bridged complexes. By allowing aerial oxidation of Mn(II) ions in mildly basic conditions and aprotic solvents, we avoid the formation of undesirable metal-oxide side products and ligand protonation and promote high-valent Mn ions and the deprotonation of ligand molecules, as required for chelation. Complex **1**, $[Mn^{IV}_3(dpo)_6]{\bullet}2MeCN$ was synthesized using a class A tridentate ligand, H_2dpo which contains bulky groups (R = Ph, Ph) that induce large torsion angles between spin carriers *via* bridging oximate groups, and influence the nature and strength of magnetic interactions between the metal ions. The structure of the centrosymmetric complex **1** consists of a trinuclear $Mn(IV)_3$ core capped by six dpo^{2-} ligands (Figure 11). The three Mn centers are linked solely *via* the oximate groups in a linear fashion with a 180° [Mn1-Mn2-Mn1] angle. The octahedral coordination environments of the metal centers are completed by O and N atoms from the ligands (Figure 12). In contrast to previously reported Mn trimers, **1** is the first example of a high valence linear trinuclear complex. In addition, it exhibits higher torsion angles than other trinuclear oximate bridged complexes (0-20°).[20] The average torsion angle between the terminal and the central manganese ions [Mn1-N-O-Mn2] was determined to be 51.3°. The increase in torsion angles is due to the presence of bulky substituents on the oximate ligand.

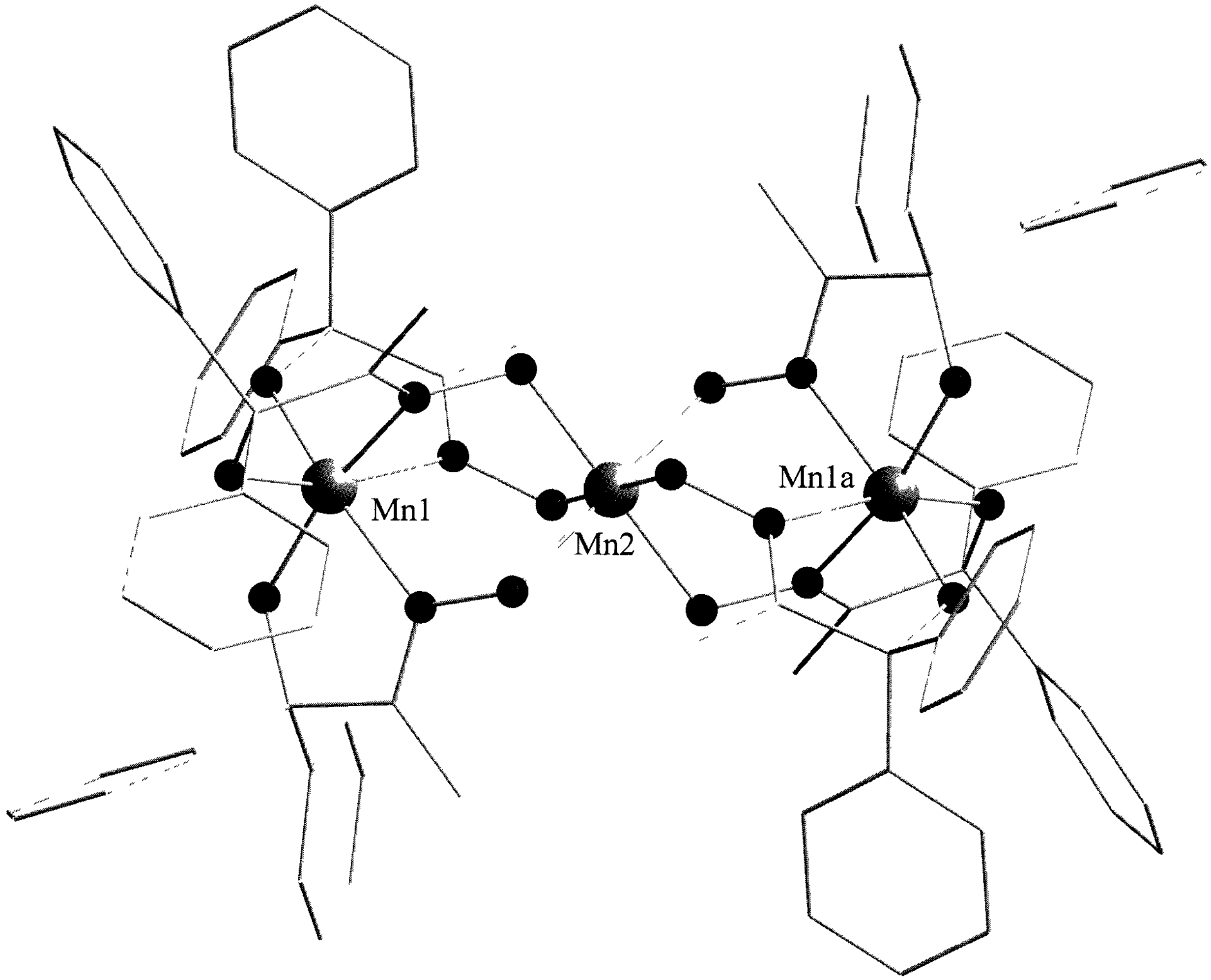

Figure 11. Molecular structure of a linear $[Mn^{IV}_3]$ complex **1** using class A ligand (H_2dpo).

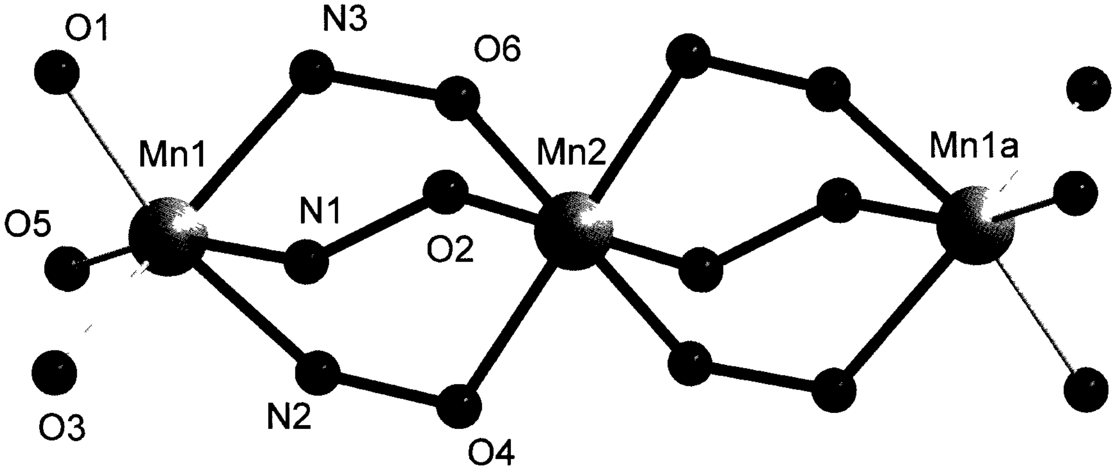

Figure 12. Central core of **1**, revealing the (Mn-N-O-Mn) superexchange pathway between the metal centres.

2.2.1 Density Functional Calculation

In order to establish the electronic structure of **1** and the influence of the ligand's bulky groups on the torsion angles, DFT calculations at the BPE/TZVP level were performed.[21] The calculated optimized structure of **1** has S_6 symmetry and is in good agreement with the X-ray structure [calculated (X-ray) Mn1-N: 2.02 (1.99), Mn1-O: 1.86 (1.82) and Mn2-O: 1.95 (1.91) Å]. The ground state was calculated to be $S_T = 9/2$ with three unpaired electrons on each Mn ion. The calculated Mn oxidation states are consistant with those determined by charge considerations and bond valence sum calculations (Table 3). The NPA-derived atomic charges of the Mn ions are +1.03 and +1.24 a.u. for Mn1 and Mn2, respectively. Such low charges for the Mn(IV) atoms indicate significant covalency of the Mn-N and Mn-O bonds in the complex. Indeed, the Mayer bond orders for Mn1-N, Mn1-O, and Mn2-O are 0.58, 1.03, and 0.78, respectively. This covalency helps to stabilize the high oxidation state of the Mn ions via ligand-to-metal charge donation (2.65 e^- to the 3d orbitals and 0.26 e^- to the 4s orbital of Mn1 and 2.46 e^- to the 3d orbitals and 0.26 e^- to the 4s orbital of Mn2).

The cyclic voltammogram of the complex in MeCN contains one irreversible one-electron reduction wave at -0.60 V (vs. Fc/Fc$^+$) indicating that only one Mn ion is reduced. The higher positive charge of Mn2 (2.99), relative to Mn1 (2.62), makes this ion a better electron acceptor. In agreement with this, the α-spin LUMO of the complex has the 45% Mn2 3d orbital contribution while the two Mn1 ions contribute only 6%. As a result, the DFT calculation of the reduced complex produces a Mn(IV)-Mn(III)-Mn(IV) configuration (S_T = 5) with the central Mn ion in a high-spin d^4 electron configuration. Such an electron configuration undergoes Jahn-Teller distortion at Mn2 and the MnO_6 octahedral environment becomes axially elongated with 1.98 Å (eq.) and 2.19 Å (axial) Mn2-O bond distances.

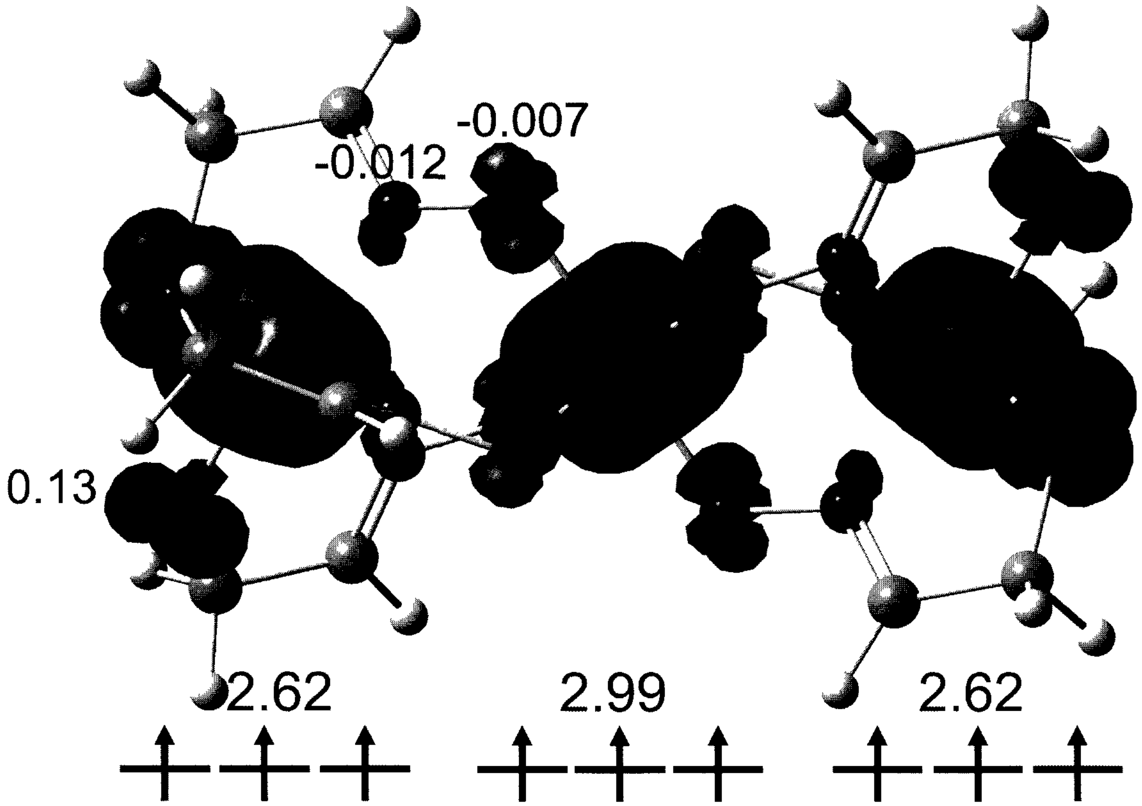

Figure 13. Spin density distribution for the simplified complex **1** (R = H, not Ph) for clarity. NPA-derived atomic spin densities are shown for Mn, N, and O atoms.

In order to probe the effects of ligand substituents on the geometry and electronic structure of **1**, a series of DFT calculations were performed for simplified ligands. In these calculations, the 12 Ph groups and 6 Me groups were replaced by H atoms. (Figure 13) The removal of the Me groups does not affect the Mn2-O-N-Mn1 torsion angles significantly but the removal of the Ph groups causes the torsion angles to decrease from avg. 52° to 43°. Thus, the steric hindrance caused by the Ph groups of the oximate ligand plays a key role in imposing the higher torsion angles which, in turn, helps to stabilize the structure.

2.2.2 Magnetism of $[Mn^{IV}_3(dpo)_6]\bullet 2MeCN$, 1

Magnetic susceptibility of **1** has been measured in an applied magnetic field of 1000 Oe and is plotted as χT vs. T in Figure 14. As the temperature decreases from 300 to 7 K, the χT product gradually increases from 6.7 cm^3K/mol to a maximum of 13.1 cm^3K/mol then slightly decreases to 12.4 cm^3K/mol at 1.8 K. The increase of the χT product above 7 K is consistant with dominant ferromagnetic interactions present within the trinuclear Mn(IV) complex and the observed maximum value of χT is in agreement with an $S_T = 9/2$ ground state (expected value: 12.375 cm^3K/mol with $g = 2$). It is worth noting that the final decrease at low temperature is presumably due to very weak magnetic anisotropy and/or to the inter-molecular antiferromagnetic interactions. As shown above, the molecular structure of **1** reveals that the main magnetic interactions between the metals centers are mediated by the -NO group from the dpo^{2-} ligands. In order to quantify the magnitude of the intra- and inter-molecular magnetic interactions an isotropic Heisenberg trinuclear model of $S = 3/2$ spins was employed and the inter-molecular magnetic interactions were treated in the frame of the mean field approximation.[22]

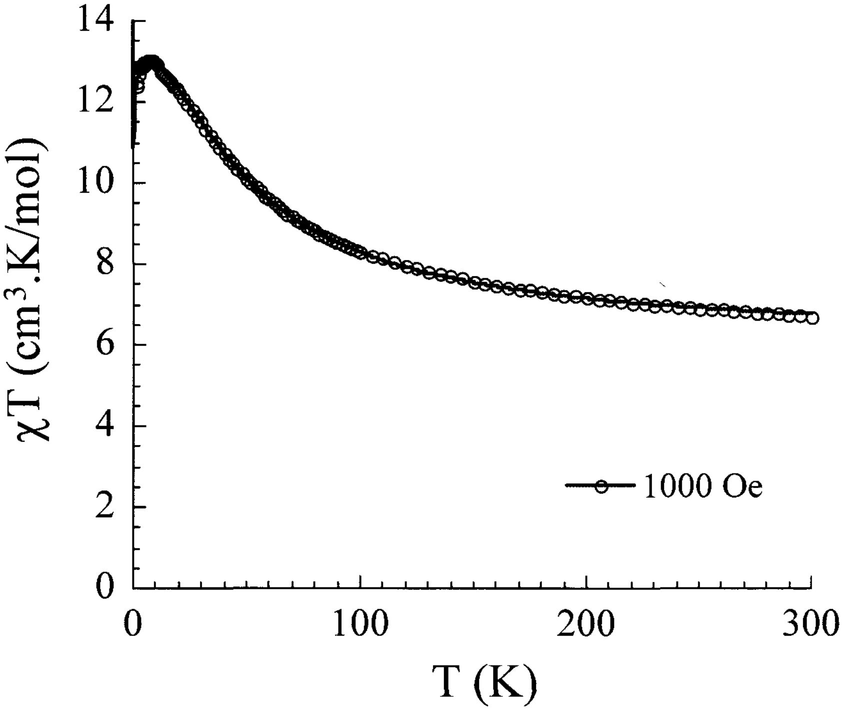

Figure 14. Plot of χT *vs.* T for complex **1** at 1000 Oe. The solid line is the best fit obtained with the Heisenberg trinuclear model described in the text.

The temperature dependence of the magnetic susceptibility was calculated in the low field approximation using the following spin Hamiltonian: $H = -2J(S_1S_2 + S_2S_3)$ where J is the exchange interactions between Mn(IV) ions in complex **1** and S_i the spin vector for each metal ion ($S_i = 3/2$ for Mn(IV) with $i = 1\text{-}3$). The application of the van Vleck equation[23] to Kambe's vector coupling scheme[24] gives an excellent fit of the experimental data from 300K to 10K. In order to fit the low temperature χT product below 10 K, inter-molecular interactions (J') were introduced in the frame of the mean field theory.[22]

This approach leads to an excellent least-squares fit of the experimental data down to 1.8 K and affords the following parameters: $J/k_B = +11.5$ (1) K, $g = 2.06$ (1) and $J'/k_B = -0.06$ (1) K. This magnetic behaviour exhibits a ground state of $S_T = 9/2$ with the first ($S = 7/2$) and second ($S = 5/2$) excited states being 34.2 and 69.7 K higher in energy, respectively.

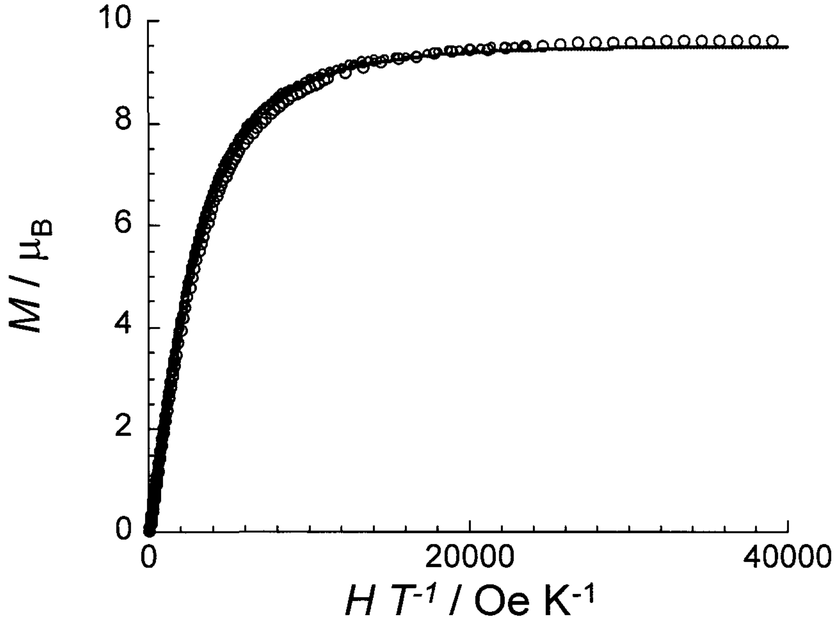

Figure 15. *M vs. H/T* plot at various temperatures between 1.8 and 8 K. The solid line is the best fit obtained with an $S = 9/2$ Brillouin function.

The field dependence (up to 7 T) of the magnetization at different temperatures (1.8 to 8 K) have also been measured as shown in Figure 15. The magnetization at 1.8 K saturates above 4 T at 9.6 μ_B in good agreement with the $S_T = 9/2$ ground state. The clear saturation of the magnetization suggests the absence of a significant magnetic anisotropy and also the presence of a well defined $S_T = 9/2$ ground state with well separated excited states as shown by the analysis of the χT vs. T data. To further confirm the $S_T = 9/2$ ground state, the M vs. H/T data have been fitted to an $S_T = 9/2$ Brillouin function that leads to an excellent theory/experiment agreement with a g factor of 2.11 (4). The ac susceptibility measurements have also been performed, however, no out-of-phase signal has been detected and thus **1** does not exhibit SMM behavior. To our knowledge there is only one linear trinuclear SMM reported to date,[25] which comprises one central Mn(III) ion and two peripheral Mn(II) ions coupled ferromagnetically with an $S = 7$ spin ground state. The magnetic anisotropy of the *SMM* originates mainly from the central Mn(III) ion. The DFT calculations and electrochemical studies of **1** clearly show that the central Mn(IV) ion is likely to be reduced to a Mn(III) ion. We believe a reduction to Mn(III) will introduce magnetic anisotropy to complex **1**, which would in turn exhibit SMM properties.

2.3 Structure and Magnetism of $[Mn^{II}(imidazole)_4OH][Mn^{IV}_3(Hoxol)_6]$•MeOH, 2

Complex **2**, $[Mn^{II}(Imz)_4OH][Mn^{IV}_3(Hoxol)_6]$•MeOH was synthesized using a class C tetra-dentate ligand, H_3oxol, which contains one oxime group and two alcohol groups with two coordination pockets. This ligand was developed in pursuit of larger nuclearity complexes which can potentially coordinate up to five metal centers. However, in complex **2** only one pocket is occupied by manganese resulting in a linear $Mn(IV)_3$ arrangement similar to complex **1**. The Mn_3 core is capped by six $Hoxol^{2-}$ ligands, which is stabilized by the five-membered coordination rings (Figure 16). The terminal Mn(IV) ions are octahedrally coordinated to three oxygen and three nitrogen atoms and the central Mn(IV) ion is coordinated to six oxygen atoms. Complex **2** crystallizes out with a Mn(II) monomer coordinated to four imidazole and one hydroxide molecule. For **2**, the average torsion angle between the terminal and the central manganese ions [Mn1-N-O-Mn2] was determined to be 50°.

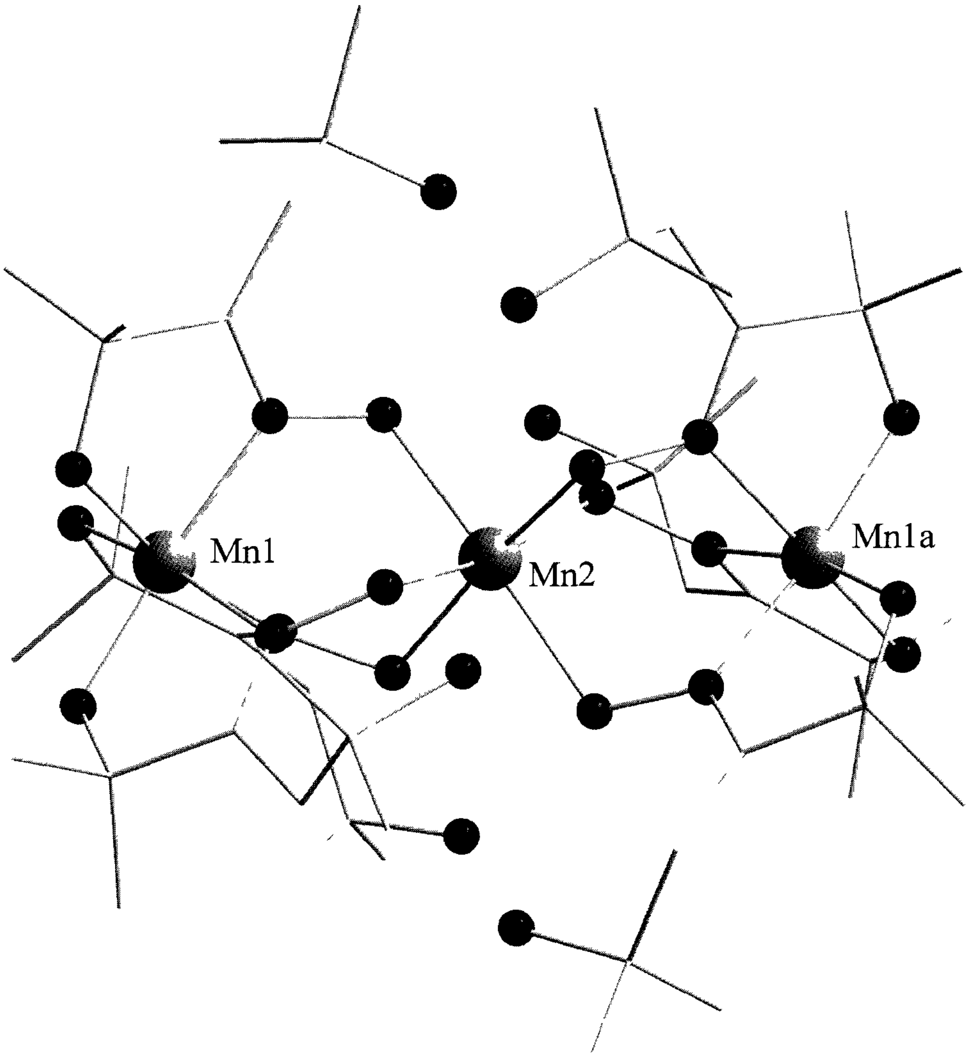

Figure 16. Molecular structure of a linear [$Mn^{IV}{}_3$] complex **2** using class C ligand (H_2oxol).

Magnetic susceptibility of **2** has been measured and plotted as χT *vs.* T in Figure 17. At room temperature, the χT product is 10.5 cm^3K/mol and as the temperature decreases from 300 to 15 K, the χT product gradually increases to reach a maximum of 14.9 cm^3K/mol then slightly decreases to 11.2 cm^3K/mol at 1.8 K. The increase in χT product reveals the presence of dominant ferromagnetic interaction within the Mn_3 unit. At low temperatures, the final decrease of the χT product below 15 K is likely the result of inter-molecular antiferromagnetic interactions. An isotropic Heisenberg trinuclear model of S = 3/2 spins for Mn(IV) ion has been considered with an S_T = 9/2. The Mn(II) monomer has been described by an S = 5/2 curie law. The best set of parameters found is: $J/k_B = +9.6(2)$ K, $g_{av} = 1.99(1)$ and $zJ'/k_B = -0.10(1)$ K.

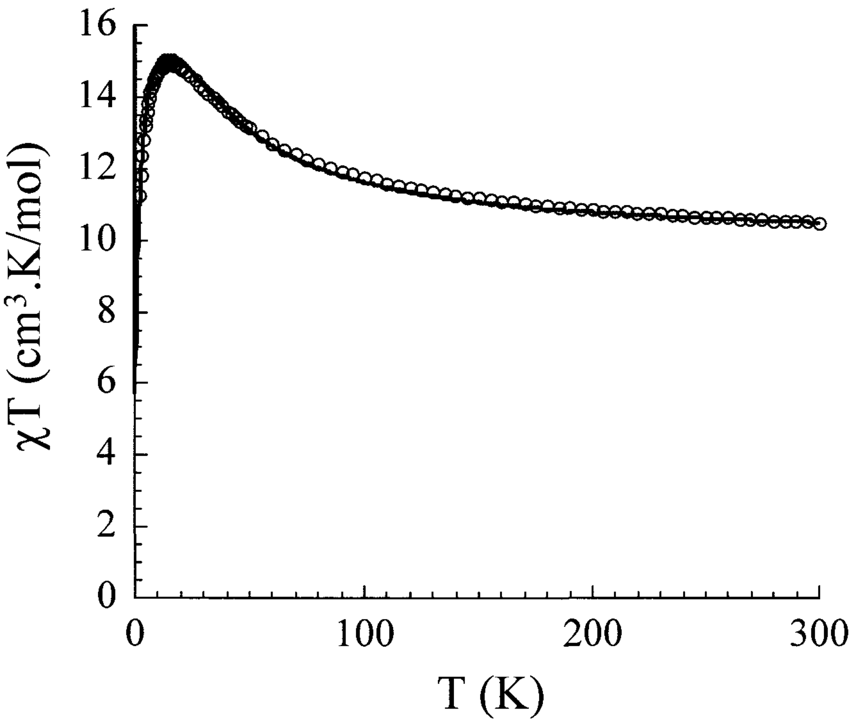

Figure 17. Plot of χT *vs.* T for complex **2** at 1000 Oe. The solid line is the best fit obtained with the Heisenberg trinuclear model.

The field dependence of the magnetization in the 1.8 – 8 K range confirms this ground state and analysis. The magnetization at 1.8 K under 7 T reaches a maximum of 12.4 μ_B without clear saturation in good agreement with an S_T = 9/2 ground state of the trinuclear unit and the S = 5/2 of the isolated Mn(II) monomer. The absence of saturation of the magnetization suggests the presence of (i) a significant magnetic anisotropy and/or (ii) of the inter-complex interactions as shown by the analysis of the χT *vs.* T data. As expected **2**, does not exhibit hysteresis or an out-of-phase component of ac susceptibility above 1.8 K. The first requirement is met in order to observe the features of an SMM, which is large spin ground state, $S = 9/2$, however, the second requirement is not. Generally, Mn(IV) ions are isotropic in nature and do not provide sufficient magnetic anisotropy to the system.

2.4 Structure and Magnetism of $[Na[Mn^{III}Mn^{IV}_2(Hoxol)_6]{\bullet}MeOH{\bullet}H_2O]_n$, 3

In an attempt to synthesize the reduced analog of **2**, the reaction conditions were varied in terms of metal source, base and solvents. Complex **3,** $[Na[Mn^{III}Mn^{IV}_2(Hoxol)_6]{\bullet}MeOH{\bullet}H_2O]_n$ was obtained by switching the base from triethylamine to sodium hydroxide. The Mn_3 unit is arranged in a linear fashion linked by a sodium cation to form the 1-D chain (Figure 19). The Mn_3 core is capped by six $Hoxol^{2-}$ ligand similar to **2**, however the terminal Mn(IV) ion is coordinated to Na^{1+} ion *via* μ-oxygen of the $Hoxol^{1-}$ ligand (Figure 18). The central Mn ion is found in the 3+ oxidation state and is confirmed by the bond valence sum calculation. There is also a prominent Jahn-Teller elongation of the bond along an axis shown in bold line. The average torsion angle was determined to be 47.5° between the terminal and the central Mn ions [Mn1-N-O-Mn2].

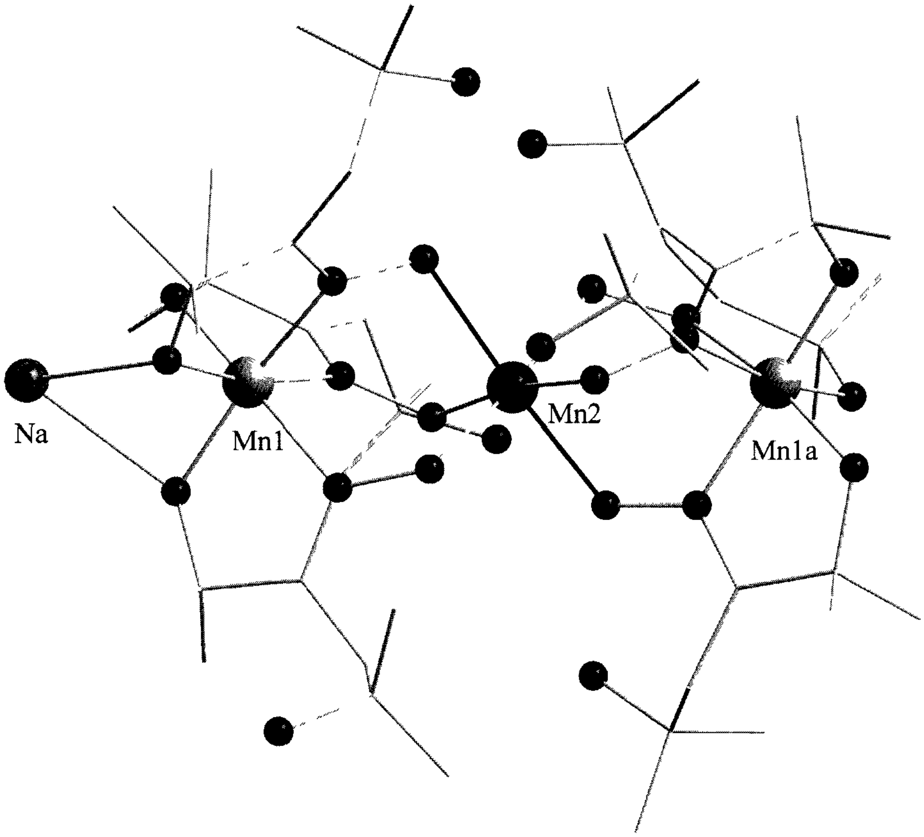

Figure 18. Molecular structure of a linear Na[$\mathrm{Mn^{III}Mn^{IV}_2}$] repeating unit of **3**.

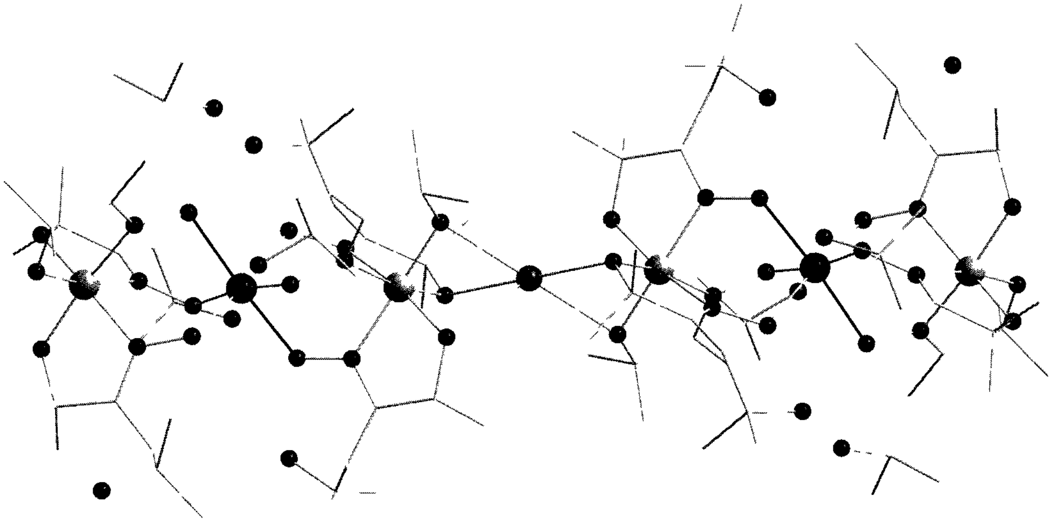

Figure 19. [$\mathrm{Mn_3}$] unit linked *via* $\mathrm{Na^+}$ cation to form a 1-D chain of **3**.

The magnetic susceptibility χT product at 300 K is 7.9 cm^{3}K/mol which is close to the theoretical value for a mixed valent Mn(III)Mn(IV)$_2$ species (6.8 cm^{3}K/mol). The χT product gradually increases as the temperature is lowered from 300 K to 18 K to reach a maximum of 14.0 cm^{3}K/mol then rapidly decrease to 5.2 cm^{3}K/mol at 1.8 K (Figure 20). The increase in χT product is indicative of dominant ferromagnetic interaction within the Mn$_3$ unit similar to **1** and **2**. At low temperature, the final decrease of the χT product below 18 K is likely due to inter-molecular antiferromagnetic interactions. Two Mn(IV) ions each contribute a spin S = 3/2 and one Mn(III) ion contribute a spin, S = 2. The overall net spin ground state of the molecule is S_T = 5. Ac magnetic susceptibility measurements were conducted in order to determine whether **3** exhibits SMM property (Figure 21). In the out-of-phase component χ'' measurement, a tail of a peak is observed at very low temperature frequency ranging from 10 - 1500 Hz; however it is difficult to quantify the energy barrier without a full peak with maxima.

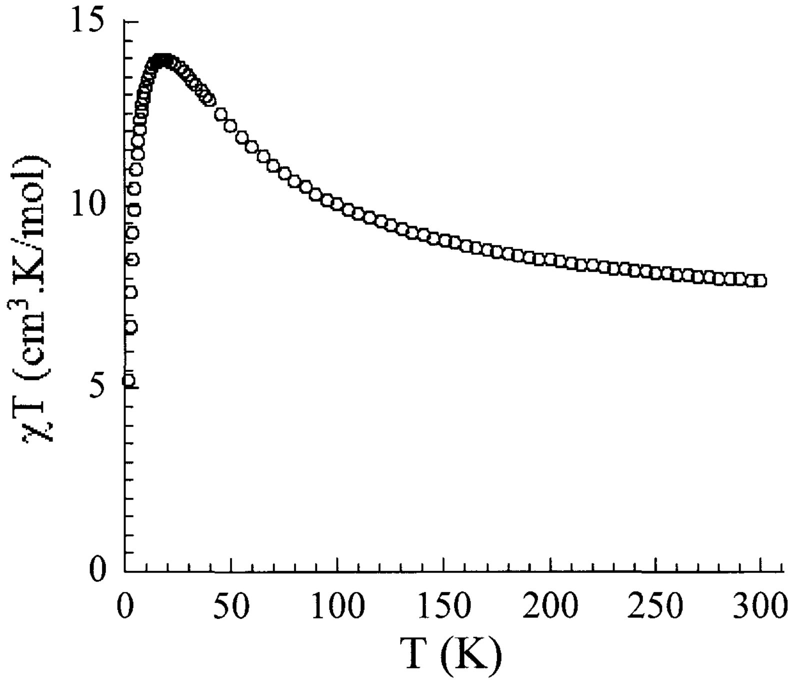

Figure 20. Plot of χT *vs.* T for complex **3** at 1000 Oe.

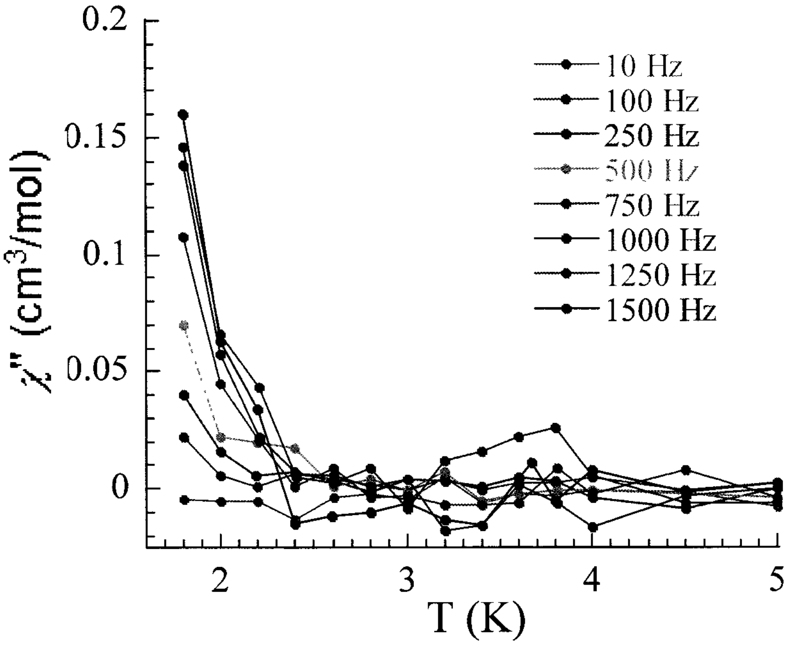

Figure 21. Plot of *ac* magnetic susceptibility out-of-phase component χ'' for complex **3**.

2.5 Discussion

Three linear Mn_3 complexes have been characterized structurally and magnetically. Complex **1** was synthesized using class A ligand, H_2dpo, and Complexes **2** and **3** was synthesized using class C ligand, H_3oxol. The net spin ground state of **1**, **2** and **3** are S_T = 9/2, 9/2 and 5, respectively. The suggested oxidation states of each Mn ion for complexes **1-3** according to the bond valence sum calculations are shown in Table 3. The suggested oxidation state for the central Mn ion for **2** is 3+, however, magnetically, it was determined to be 4+. The experimental data have been fitted using the Mn(IV)Mn(III)Mn(IV) Heisenberg model, however, it gave a lower g value of 1.88. The $Mn(IV)_3$ model gave the best fit with a *g* value of 1.99, which is more accurate.

Table 3. Bond valence sum calculation with the suggested oxidation states for **1-3**.

	Terminal Mn1 and 1a				Central Mn2			
Complex	Mn(II)	Mn(III)	Mn(IV)	Ox. state	Mn(II)	Mn(III)	Mn(IV)	Ox. state
1	4.26	4.00	4.02	4	4.03	3.69	3.87	4
2	4.53	4.26	4.29	4	3.06	2.80	2.94	3
3	4.36	4.10	4.13	4	3.12	2.85	2.99	3

All three complexes possess relatively large torsion angles, ranging from 47-54° and this is primarily due to the large substituents on the alpha carbon to the oxime group (i.e. for ligand V- Ph, Ph and ligand X- Me, Me). Complexes **1** and **2** do not exhibit the properties of an SMM due to the absence of magnetic anisotropy; however, by reducing the central Mn ion to 3+ the properties of the molecules can be switched. Theoretically, **3** should exhibit the properties of an SMM and this was indeed observed experimentally with the shifting of peaks in the out-of-phase component at low temperature for the ac susceptibility measurements. It is difficult to obtain the energy barrier for **3** because of the absence of full peaks; only the tail of the peak was observed.

In order to increase the SMM behaviour of **3**, the terminal Mn(IV) ions should be reduced to Mn(III) ions to maximize the magnetic anisotropy to the Mn_3 linear system.

Table 4. Selected bond distances and torsion angles for **1** - **3**.

Complex	**1**	**2**	**3**
Mn(1)...Mn(2)	3.557(14)	3.548(23)	3.541(25)
Mn(1)-N(3)-O(6)-Mn(2)	48.8	49.7	47.8
Mn(1)-N(1)-O(2)-Mn(2)	53.5	51.4	47.4
Mn(1)-N(2)-O(4)-Mn(2)	51.7	48.8	47.2
Mn(1)-O(1)	1.826(7)	1.818(88)	1.827(70)
Mn(1)-O(5)	1.826(8)	1.839(81)	1.838(73)
Mn(1)-O(3)	1.834(8)	1.872(81)	1.839(92)
Mn(1)-N(1)	1.996(8)	1.967(104)	2.001(114)
Mn(1)-N(2)	1.989(8)	2.002(106)	1.971(98)
Mn(1)-N(3)	1.997(9)	1.977(101)	1.986(95)
Mn(2)-O(2)	1.911(6)	2.041(80)	2.135(93)
Mn(2)-O(4)	1.910(7)	2.034(81)	1.987(81)
Mn(2)-O(6)	1.915(6)	1.970(74)	1.902(72)

Table 5. Magnetic fit parameters for complexes **1** - **3**.

Complex	J (K)	g	χT*	S_T
$[Mn^{IV}_3(dpo)_6]$•MeCN **1**	+11.5(1)	2.06(1)	6.7	9/2
$[Mn^{II}(Imz)_4OH][Mn^{IV}_3(oxol)_6]$•MeCN **2**	+9.6(2)	1.99(1)	10.5	9/2
$[Na[Mn^{IV}_2Mn^{III}(oxol)_6]$•MeOH•$H_2O]_n$ **3**	-	-	7.9	5

* cm^3K/ mol at 300 K

Chapter 3

3.1 Inducing Ferromagnetism in $Mn(III)_3$ Triangles

Manganese triangles are known to be anti-ferromagnetic in nature[26]; however, in the last few years, ferromagnetic triangles were isolated by fine tweaking the surrounding chelating agent. The origin of ferromagnetism is a difficult phenomenon to elucidate and many researchers including G. Christou, H-L. Tsai and E.K. Brechin and co-workers have postulated that these behaviours are based on high torsion angles which are hypothetically induced by the substituent on the chelating agents. In recent years, we have witnessed an increase in research effort towards the synthesis of ferromagnetic $Mn(III)_3$ triangles due to their interesting physical properties and their potential use as molecular magnets.[27] As mentioned in section 1.3, the main factors required for observing SMM behaviour in small molecules are high spin ground state (S) and significant negative zero-field splitting (D), which, in combination, give rise to the energy barrier (U) for the reversal of the magnetization. The maximum value of the energy barrier is given by $U = S^2|D|$ or $(S^2\text{-}1/4)\ |D|$ for integer and half-integer spin, respectively.[14] Since the spin ground state is the main component of the latter equations, ferromagnetism is an important aspect in engineering molecular nano-magnets. This was shown by E.K. Brechin and co-workers' Mn_6[13] cluster consisting of two stacked triangles producing $S_T = 12$ and $U_{eff} = 86$ K, which currently holds the record for the highest energy barrier. Although many examples of high-nuclearity, mixed-valent Mn(II)/Mn(III)/Mn(IV) SMMs have been reported,[28] those containing the triangular motif are rare and only a few examples of purely ferromagnetic $Mn(III)_3$ systems were isolated in the last few years. Many hypothesized that the origins of ferromagnetic behaviour in triangles are induced by the methyl group of the H_2salox-Me ligand.[29] Our synthetic approach to understanding this phenomenon is by ligand modification around the Mn(III)$_3$ magnetic unit. Using this strategy, a magneto-structural correlation can be obtained to probe the nature and the strength of the interaction.

With this in mind, we have developed a systematic approach to the assembly of $[\mathrm{Mn}^{\mathrm{III}}{}_3(\mu_3\text{-O})]^{+7}$ with five- and six- membered chelating rings using Class A ligands (II and IV) and Class B ligands (VII and VIII), respectively. In doing so, we were able to synthesize Mn(III)$_3$ triangles with five- and six- membered chelating ring along the edges of the two Mn(III) ions giving rise to the dihedral angles (Figure 22). A correlation was observed between the equatorial ligands, the dihedral angles and the nature of the coupling interactions. The six-membered chelating ring allows for greater flexibility, inducing larger torsion angles and giving rise to ferromagnetic interactions. The oxime-based ligands are essential for synthesizing such molecules. Furthermore, understanding how this behaviour arises is an important aspect in the field of magnetism.

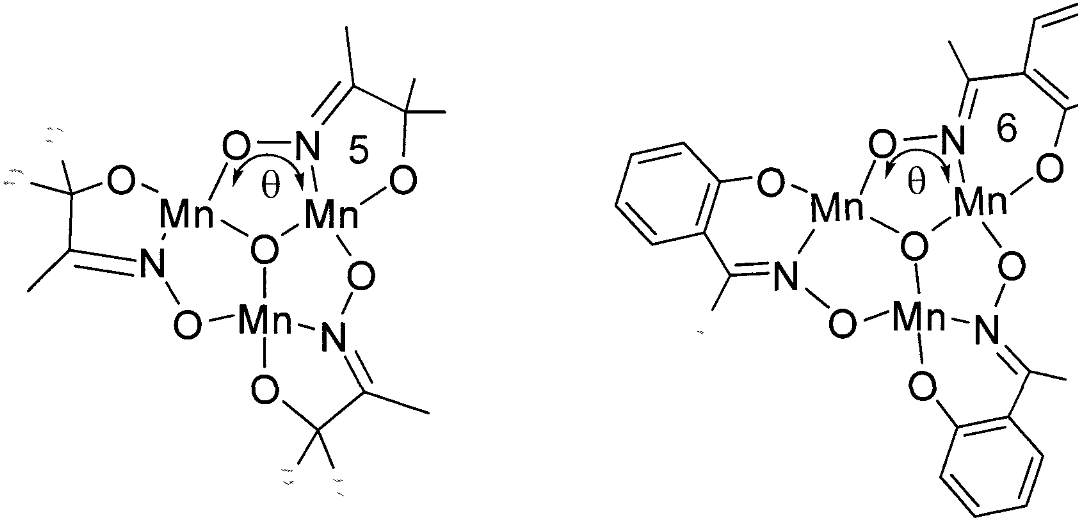

Figure 22. *Left:* Mn$_3$ triangle with class A ligands (II and IV). *Right:* Mn$_3$ triangle with class B ligands (VII and VIII).

Eight Mn(III)$_3$ triangular complexes (**4** - **11**) were characterized structurally and magnetically. A systematic approach to synthesizing the Mn(III)$_3$ triangles was employed, where the ferromagnetic interactions were induced by means of ligand modification. This extensive study shows the ferromagnetic behaviour arising from two factors; a six-membered coordination ring and a high dihedral angle along the oxime bridge, Mn-NO-Mn. Understanding the origin of ferromagnetic interaction in Mn$_3$ triangles allows us to predict the magnetic behaviour based solely on the structural features of the complex.

3.2 Structure and Magnetism of $[Mn^{III}_3(\mu_3\text{-}O)(cpo)_3(ClO_4)(MeOH)_3]$, 4

Complex **4**, $[Mn^{III}_3(\mu_3\text{-}O)(cpo)_3(ClO_4)(MeOH)_3]$, consists of three Mn(III) ions arranged in an equilateral triangular configuration (Figure 23). All three Mn ions possess a distorted octahedral geometry with C_3 symmetry linked *via* the central μ_3-oxide atom (O1). The Mn...Mn distance for **4** is 3.26 Å as shown in Table 6. The inorganic core $[Mn^{III}_3(\mu_3\text{-}O)]$ is surrounded by three equatorial ligands ($Leq.^{-2}$ = cpo^{-2}) arranged in a near-planar fashion coordinating to the three Mn(III) ions through the oxime bridges [Mn-N-O-Mn]. The cpo^{-2} ligand generates five-membered coordination rings which are less flexible than six resulting in a small torsion angle of 18.6° along the Mn-N-O-Mn moiety. The top face of the core is weakly linked to a perchlorate anion, which acts as a tripodal chelating agent bridging/ stabilizing the Mn$_3$ unit. In addition, the bottom face of the triangular core is weakly coordinated to three axial ligands (L ax. = MeOH). This gives rise to Jahn-Teller elongation along the axial positions of the distorted octahedral Mn(III) ions. The oxidation state of each Mn ion is 3+ and is confirmed by bond valence sum calculations (Table 8) and charge considerations. The Mn(III)$_3$ core is held rigidly by a central

μ_3-oxygen which is below the Mn_3 plane by 0.30 Å and as a result, the elongated axis is in near-parallel fashion.

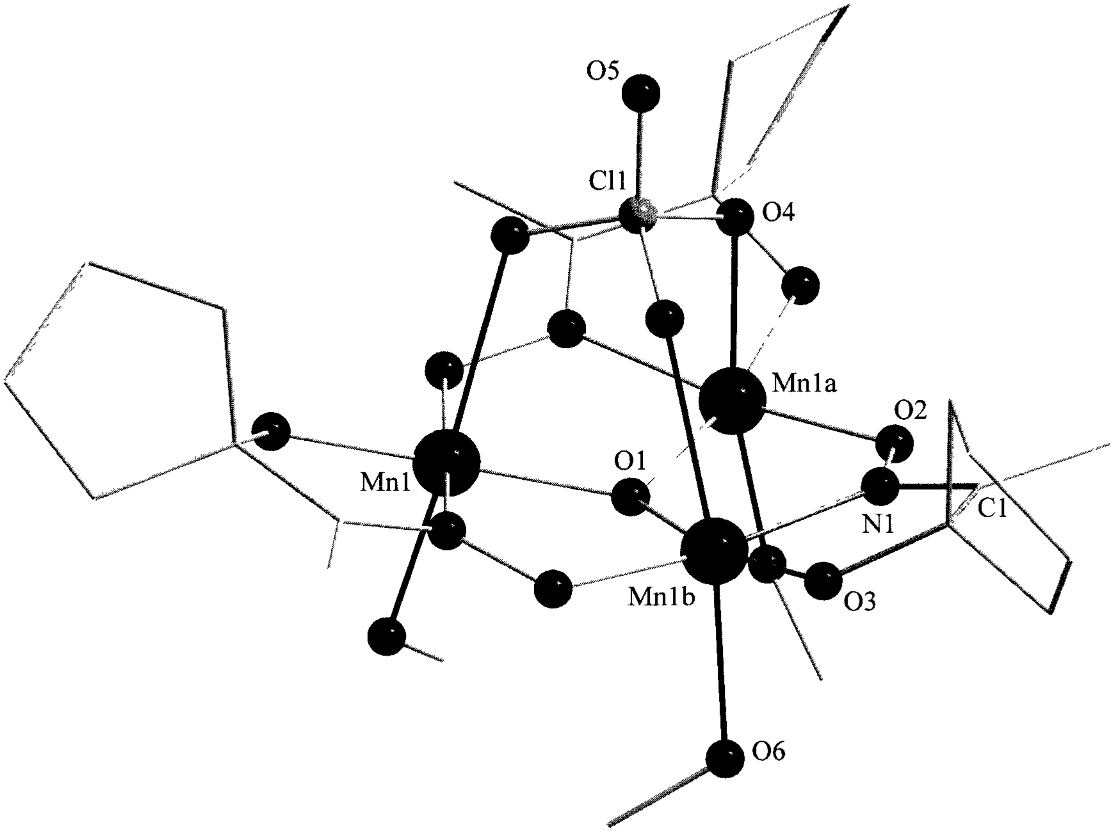

Figure 23. Molecular structure of $[Mn^{III}_3(\mu_3\text{-}O)(cpo)_3(ClO_4)(MeOH)_3]$, **4**.

Magnetic susceptibility measurements were performed between 1.8 K and 300 K (Figure 24). At room temperature, the χT product is 8.4 cm^3K/mol which is slightly lower in comparison to the expected value of 9.0 cm^3K/mol for three non-interacting Mn(III) ions (g = 2.00; C = 3.00 cm^3K/mol). This slightly low value is the result of the intra-molecular antiferromagnetic interaction in the $[Mn_3]$ core. The χT product decreases from 300 K to 1.8 K to reach a value of 0.9 $cm^3K/$ mol at 1000 Oe indicating a dominant antiferromagnetic interaction. The experimental data have been fitted down to 10 K using an isotropic Heisenberg $S = 2$ regular triangle model taking the following Hamiltonian:

$$H = -2J(S_1 \bullet S_2 + S_1 \bullet S_3 + S_2 \bullet S_3) \quad \text{Eq. 3}$$

The best set of parameters found is $J/k_B = -3.1(1)$ K and $g = 1.99(1)$. The ground state of the Mn_3 unit is not completely clear. In a pure Heisenberg model the ground state would be $S = 0$ but due to the significant anisotropy of the Mn(III) it is here difficult to conclude as the χT product below 10 K seems to clearly extrapolate below 3 cm^3K/mol suggesting a ground state clearly lower than 2.

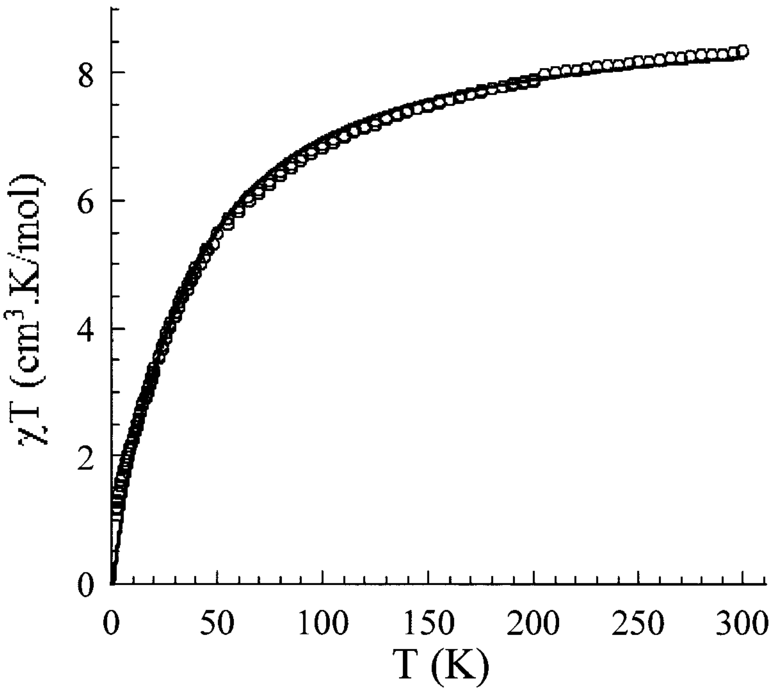

Figure 24. Plot of χT *vs.* T for complex **4** at 1000 Oe. The solid line is the best fit obtained with the Heisenberg trinuclear model.

3.3 Structure and Magnetism of $[Mn^{III}_3(\mu_3\text{-}O)(cpo)_3(ClO_4)(Imz)_3]$, 5

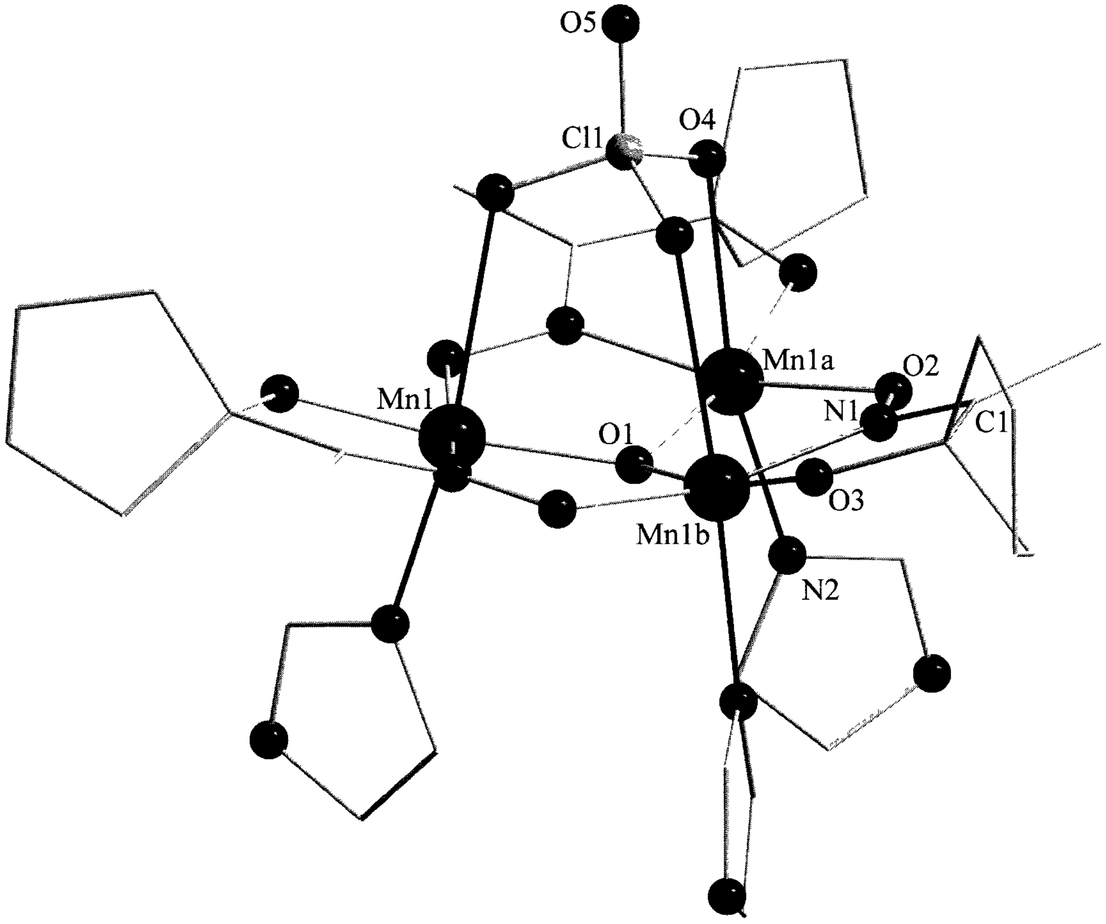

Figure 25. Molecular structure of $[Mn^{III}_3(\mu_3\text{-}O)(cpo)_3(ClO_4)(Imz)_3]$, **5**.

Complex **5**, $[Mn^{III}_3(\mu_3\text{-}O)(cpo)_3(ClO_4)(Imz)_3]$, consists of three Mn(III) ions arranged in an equilateral triangular configuration similar to **4**. However, the bottom face of the Mn_3 core is weakly coordinated to three imidazole (Imz) molecule as opposed to three methanol molecules (Figure 25). All three Mn ions possess a distorted octahedral geometry with C_3 symmetry linked *via* the central μ_3-oxide atom (O1). The Mn...Mn distance for **5** is 3.22 Å as shown in Table 6. The oxidation state of each Mn ion is 3+ and is confirmed by bond valence sum calculations and charge considerations. The Mn(III)$_3$ core is held by a central μ_3-oxygen which is below the Mn$_3$ plane by 0.32 Å and as a result, the elongated axis is in near-parallel fashion.

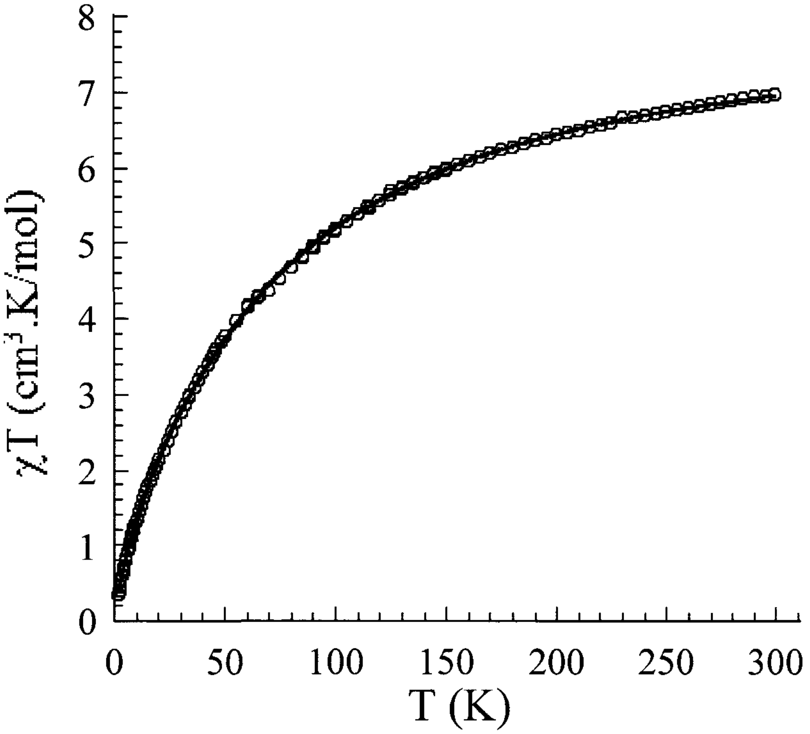

Figure 26. Plot of χT *vs.* T for complex **5** at 1000 Oe. The solid line is the best fit obtained with the Heisenberg trinuclear model.

At room temperature, the χT product at 1000 Oe is 7.2 cm^{3}K/mol which is low in comparison to the expected value of 9.00 cm^{3}K/mol for three non-interacting Mn(III) ions (g = 2.00; C = 3.00 cm^{3}K/mol). This result suggests the presence of significant antiferromagnetic interaction between Mn(III) S = 2 metal ions as confirmed by the thermal dependence of the χT product (Figure 26). When the temperature is lowered to 1.8 K the χT product decreases reaching 0.36 cm^{3}K/ mol. Down to 1.8 K, the experimental data have been fitted using an isotropic Heisenberg S = 2 triangle model similar to **4**. The best sets of parameters found are J/k_B = -6.3(1) K, g = 2.0(2) and ρ = 0.42 cm^{3}K/mol. A ρ parameter had to be introduced in the model to take into account the residual Curie paramagnetism observed at low temperature. The ρ value indicates that a very small amount of paramagnetic by-product is present in the compound which is always seen when compounds have a diamagnetic ground state. The ground state of the Mn_3 unit seems to be 0 as expected in a pure Heisenberg model suggesting the absence of significant magnetic anisotropy of the Mn(III).

3.4 Structure and Magnetism of $[Mn^{III}_3(\mu_3\text{-}O)(cpo)_3(ClO_4)(Phpy)_3]$•4.5 MeCN, 6

Complex **6**, $[Mn^{III}_3(\mu_3\text{-}O)(cpo)_3(ClO_4)(Phpy)_3]$•4.5MeCN, consists of three Mn(III) ions arranged in an equilateral triangular configuration similar to **4** and **5**. However, the bottom face axial ligands have been replaced with bulkier molecule, phenylpyridine (L ax. = Phpy). Again, all three Mn ions possess a distorted octahedral geometry with C_3 symmetry linked *via* the central μ_3-oxide atom (O1). The Mn...Mn distance and torsion angle along the the Mn-N-O-Mn moiety for **4** is 3.24 Å and 5.0°, respectively. The top face of the core is weakly linked to a perchlorate anion, which acts as a tripodal chelating agent bridging/ stabilizing the Mn_3 unit (Figure 27). This gives rise to Jahn-Teller elongation along the axial positions of the distorted octahedral Mn(III) ions. The oxidation state of each Mn ion is 3+ and is confirmed by bond valence sum calculations (Table 5) and charge considerations. The $Mn(III)_3$ core is held rigidly by a central μ_3- oxygen which is below the Mn_3 plane by 0.22 Å.

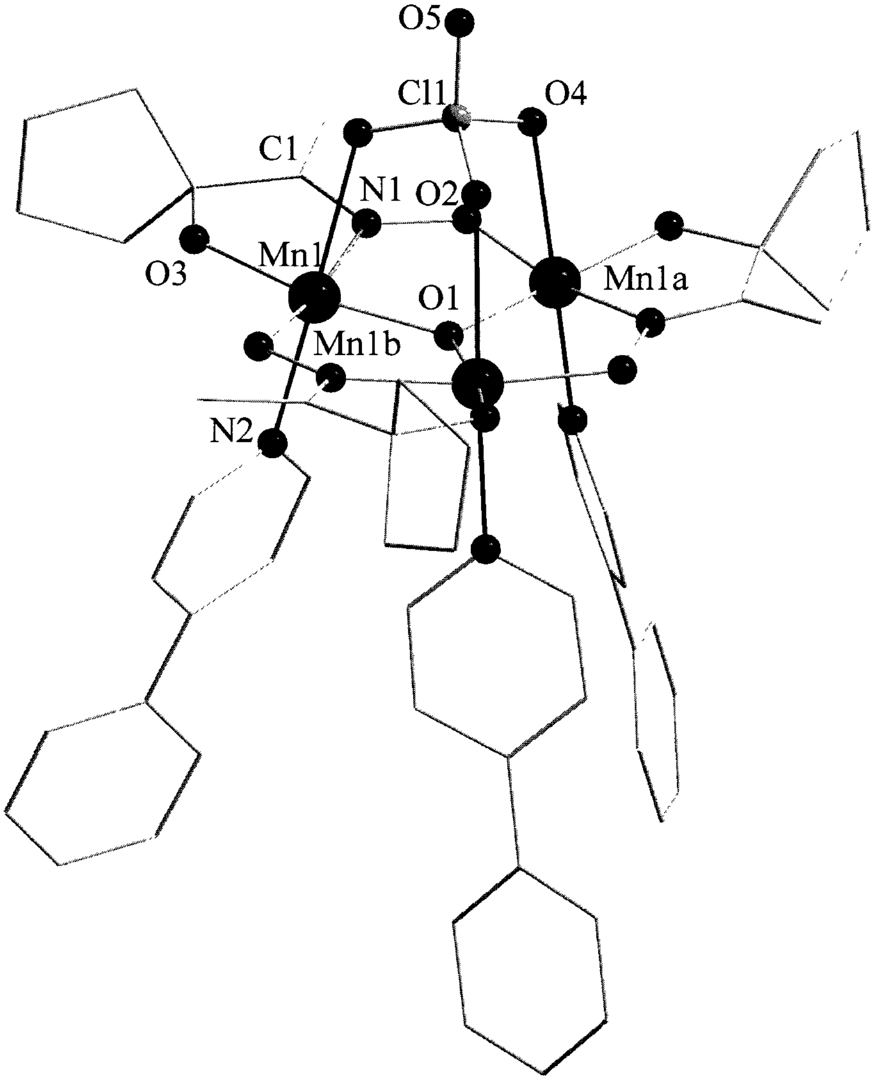

Figure 27. Molecular structure of $[Mn^{III}_3(\mu_3\text{-}O)(cpo)_3(ClO_4)(Phpy)_3]\cdot 4.5MeCN$, **6**.

At room temperature, the χT product is 8.1 cm^3K/mol that is low in comparison to the expected value of 9.00 cm^3K/mol for three non-interacting Mn(III) ions (g = 2.00; C = 3.00 cm^3K/mol). This result suggests the presence of significant antiferromagnetic interaction between Mn(III) S = 2 metal ions as confirmed by the thermal dependence of the χT product (Figure 28). When the temperature is lowered, χT decreases reaching 0.17 cm^3K/mol at 1.8 K for the compound measured in solution. Down to 2 K, the experimental data have been fitted using an isotropic Heisenberg S = 2 regular triangle model similar to **4** and **5** triangle models.

The best sets of parameters found are J/k_B = -4.2(1) K and g = 1.98(2). The g factor is slightly lower than 2 as previously reported for Mn(III) sites. The ground state of the Mn_3 unit seems to be 0 as expected in a pure Heisenberg model suggesting the absence of significant magnetic anisotropy of the Mn(III).

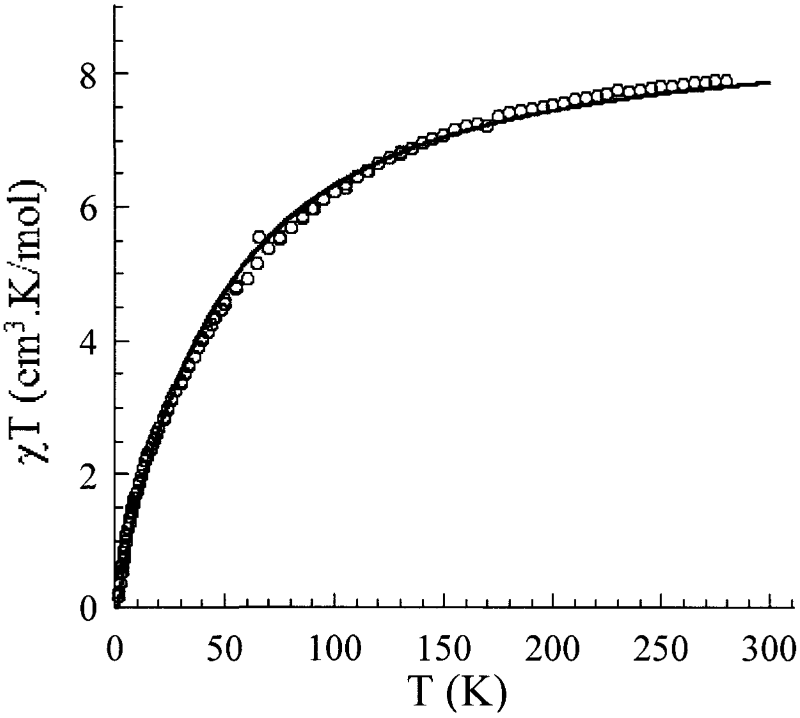

Figure 28. Plot of χT *vs.* T for complex **6** at 1000 Oe. The solid line is the best fit obtained with the Heisenberg trinuclear model.

3.5 Structure and Magnetism of $[Mn^{III}_3(\mu_3\text{-}O)(dmo)_3(ClO_4)(MeOH)_3]$, 7

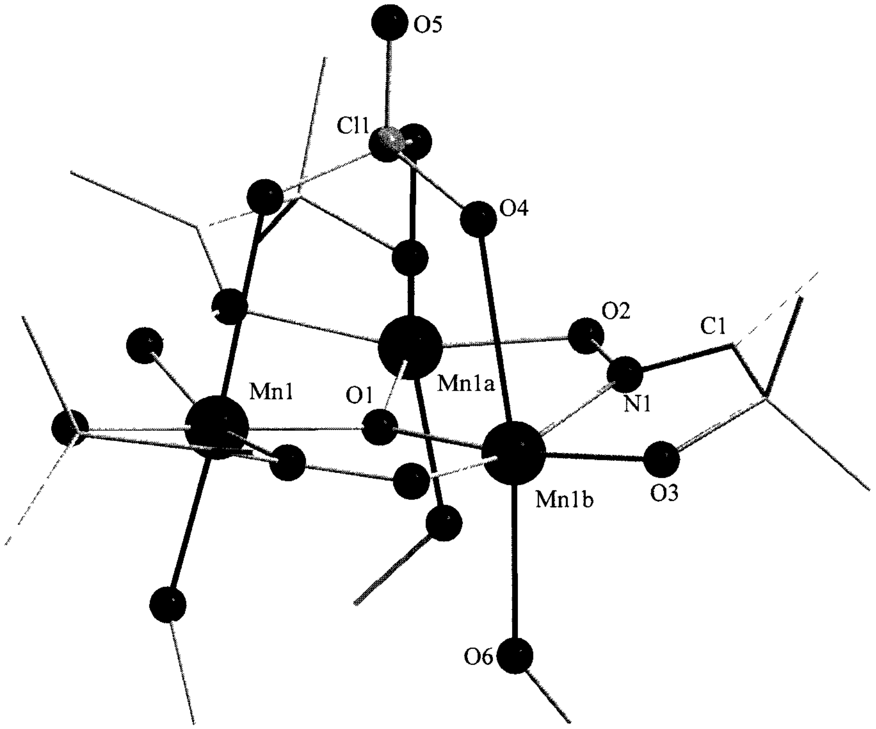

Figure 29. Molecular structure of $[Mn^{III}_3(\mu_3\text{-}O)(dmo)_3(ClO_4)(MeOH)_3]$, 7.

Complex 7, $[Mn^{III}_3(\mu_3\text{-}O)(dmo)_3(ClO_4)(MeOH)_3]$, consists of three Mn(III) ions arranged in an equilateral triangular configuration (Figure 29). The inorganic core $[Mn^{III}_3(\mu_3\text{-}O)]$ is surrounded by three equatorial ligands ($Leq.^{-2}$ = dmo^{-2}) which is arranged in a near-planar fashion coordinating to the three Mn(III) ions through the oxime bridges [Mn-N-O-Mn]. The dmo^{-2} ligand generates five- membered coordination rings, in turn, producing a small torsion angle of 6.4° along the Mn-N-O-Mn moiety. The top face of the core is weakly linked to a perchlorate anion. The bottom face of the core is weakly coordinated to three axial ligands (L ax. = MeOH). The $Mn(III)_3$ metal centers are linked by a central μ_3-oxygen which is below the Mn_3 plane by 0.21Å.

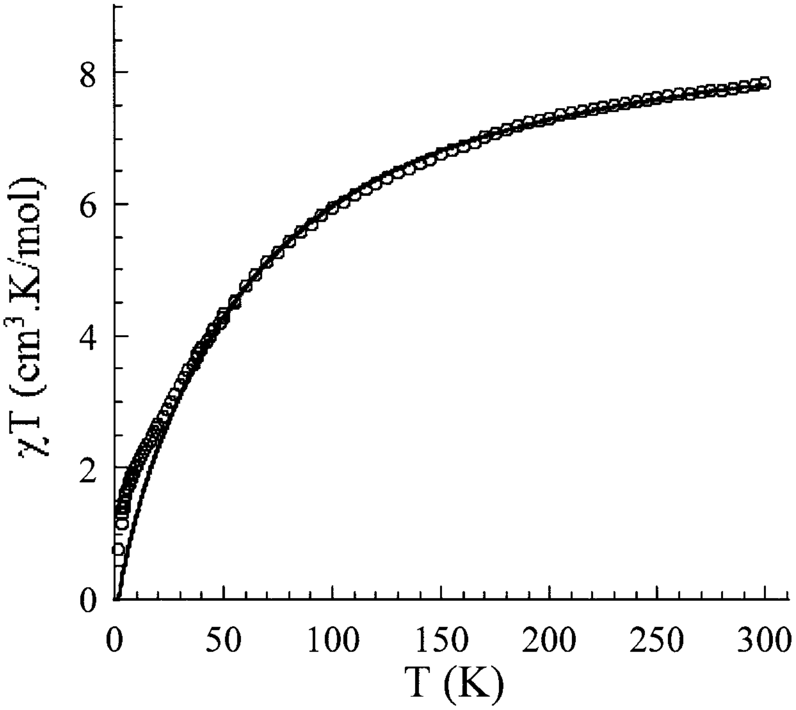

Figure 30. Plot of χT *vs.* T for complex **7** at 1000 Oe. The solid line is the best fit obtained with the Heisenberg trinuclear model.

At room temperature, the χT product is 7.8 cm^{3}K/mol. When the temperature is lowered, the χT product decreases reaching 0.78 cm^{3}K/mol at 1.8 K indicating strong antiferromagnetic interactions between $S = 2$ Mn(III) spins (Figure 30). Down to 40 K, the experimental data have been fitted using a isotropic Heisenberg $S = 2$ regular triangle model as shown eq. 3. The best set of parameters found is $J/k_B = -5.1(1)$ K and $g = 1.99(1)$ as expected for Mn(III) sites (red line in the Figure 30 fitted down to 40 K). The ground state of the Mn_3 unit is not completely clear. In a pure Heisenberg model, the ground state would be $S = 0$ but due to the significant anisotropy of the Mn(III) it is difficult to conclude as the χT product below 25 K seems to clearly extrapolate below 3 cm^{3}K/mol suggesting a ground state lower than 2.

3.6 Structure and Magnetism of $[\mathrm{Mn^{III}}_3(\mu_3\text{-O})(\mathrm{dmo})_3(\mathrm{ClO_4})(\mathrm{EtOH})_3]$, 8

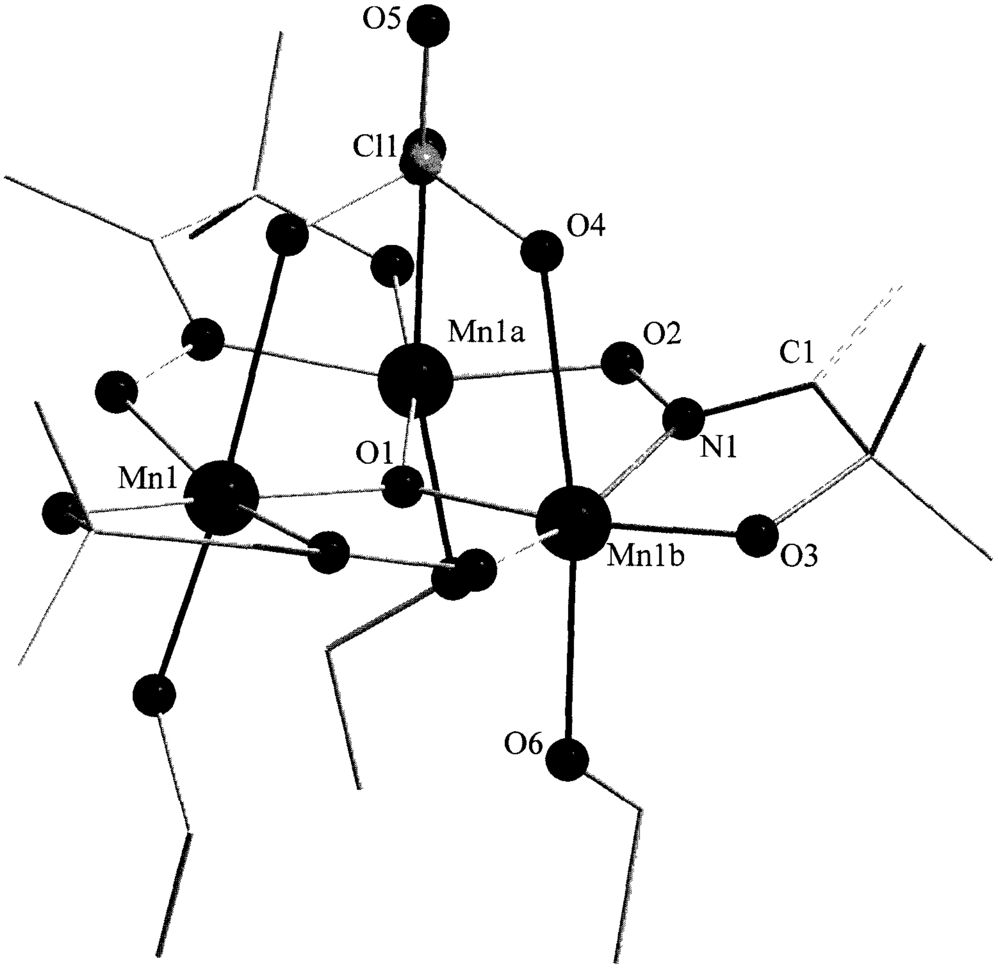

Figure 31. Molecular structure of $[\mathrm{Mn^{III}}_3(\mu_3\text{-O})(\mathrm{dmo})_3(\mathrm{ClO_4})(\mathrm{EtOH})_3]$, **8**.

Complex **8**, $[\mathrm{Mn^{III}}_3(\mu_3\text{-O})(\mathrm{dmo})_3(\mathrm{ClO_4})(\mathrm{EtOH})_3]$, consists of three Mn(III) ions arranged in an equilateral triangular configuration similar to **7**. However, the bottom face of the $\mathrm{Mn_3}$ core is weakly coordinated to three EtOH molecules (Figure 31). All three Mn ions possess a distorted octahedral geometry with C_3 symmetry linked *via* the central μ_3-oxide atom (O1), which is below the $\mathrm{Mn_3}$ plane by 0.32 Å.

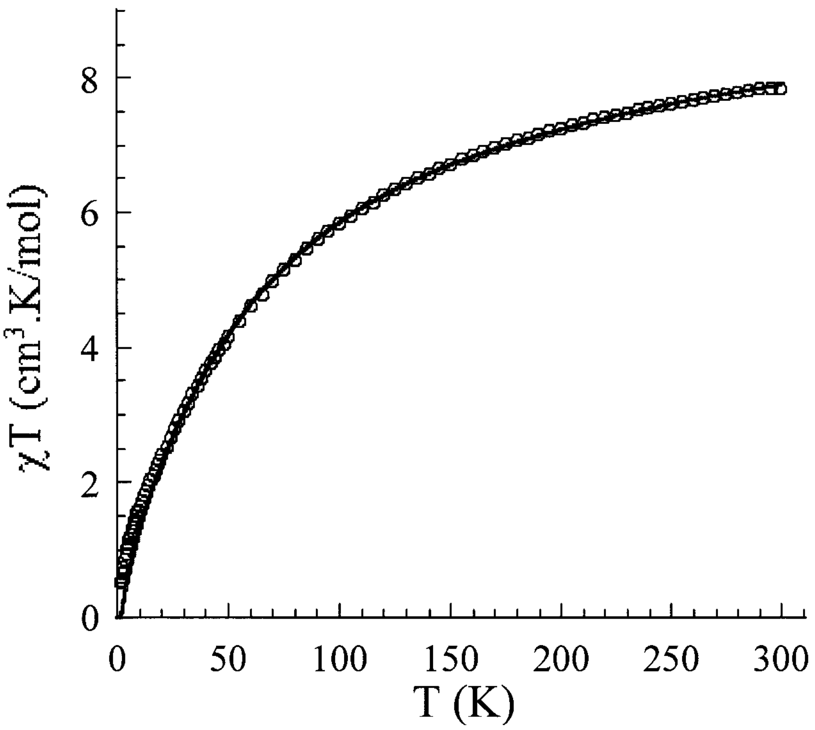

Figure 32. Plot of χT *vs.* T for complex **8** at 1000 Oe. The solid line is the best fit obtained with the Heisenberg trinuclear model.

The χT product at room temperature is 7.8 cm^{3}K/mol. When the temperature is lowered, the χT product decreases to 0.52 cm^{3}K/mol at 1.8 K (Figure 32). Down to 10 K, the experimental data have been fitted using an isotropic Heisenberg $S = 2$ regular triangle model. The best sets of parameters found are $J/k_B = -5.2(1)$ K and $g = 1.99(1)$. In a pure Heisenberg model the ground state would be $S = 0$ but due to the significant anisotropy of the Mn(III) it is here difficult to conclude as the χT product below 10 K seems to clearly extrapolate below 3 cm^{3}K/mol suggesting a ground state lower than 2.

3.7 Structure and Magnetism of $[Mn^{III}_3(\mu_3\text{-}O)(dmo)_3(ClO_4)(Imz)_3]$, 9

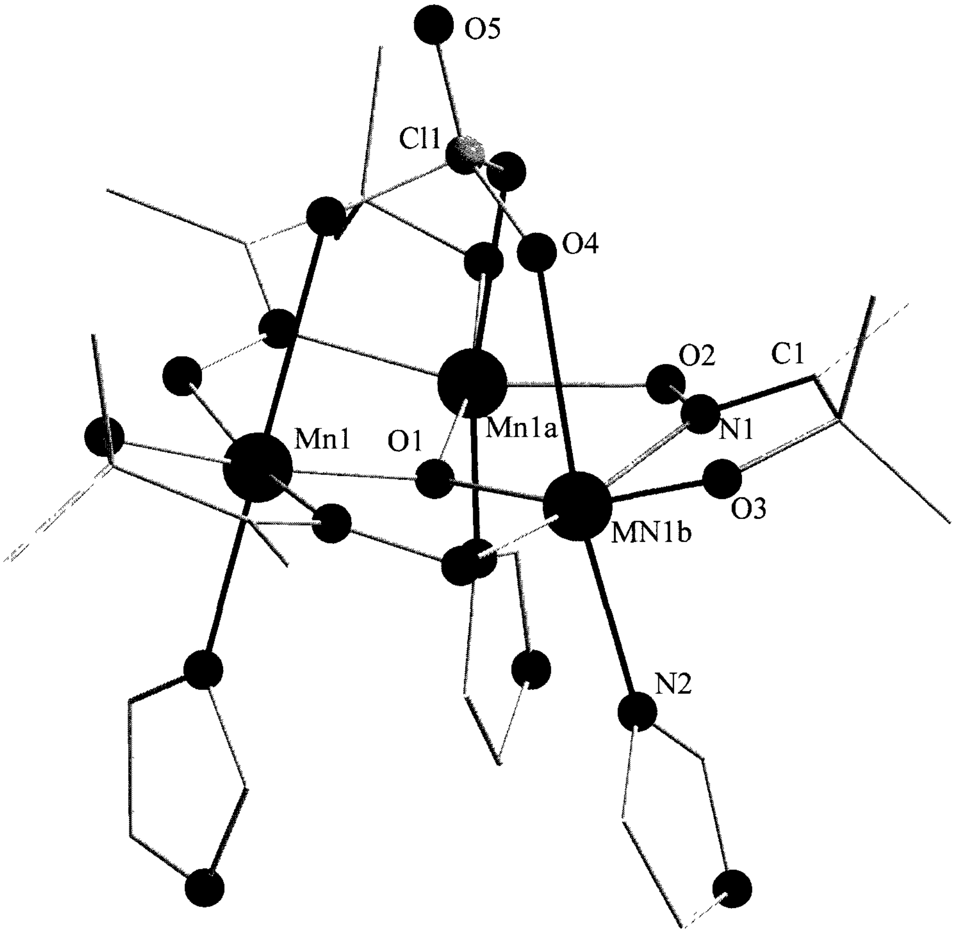

Figure 33. Molecular structure of $[Mn^{III}_3(\mu_3\text{-}O)(dmo)_3(ClO_4)(Imz)_3]$, **9**.

Complex **9**, $[Mn^{III}_3(\mu_3\text{-}O)(dmo)_3(ClO_4)(Imz)_3]$, consists of three Mn(III) ions arranged in an non-equilateral triangular configuration (Figure 33). It is similar to **7** and **8** except the bottom face of the Mn_3 core is weakly coordinated to three imidazole molecules. All three Mn ions possess a distorted octahedral geometry, which is linked *via* the central μ_3-oxide atom (O1), which is below the Mn_3 plane by 0.28 Å.

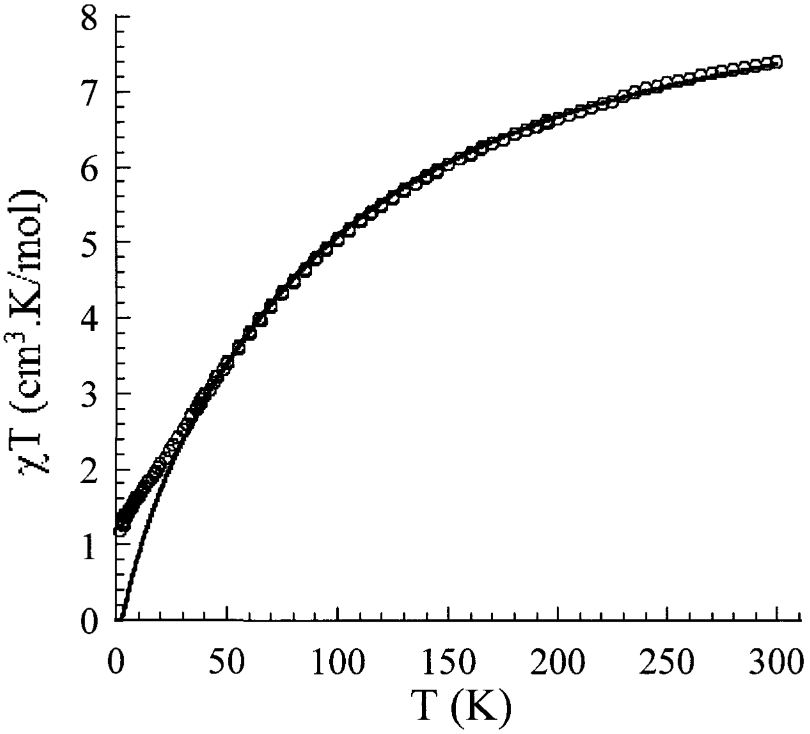

Figure 34. Plot of χT *vs.* T for complex **9** at 1000 Oe. The solid line is the best fit obtained with the Heisenberg trinuclear model.

At room temperature, the χT product is 7.4 cm^{3}K/mol. When the temperature is lowered, the χT product decreases to 1.1 cm^{3}K/mol at 1.8 K indicating strong antiferromagnetic interactions between $S = 2$ Mn(III) spins (Figure 34). Down to 35 K, the experimental data have been fitted using a isotropic Heisenberg $S = 2$ regular triangle model. The best set of parameters found is $J/k_B = -7.7(1)$ K and $g = 2.00(1)$ as expected for Mn(III) sites (red line shows the fit down to 35 K). The ground state of the Mn_3 unit is not completely clear. In a pure Heisenberg model the ground state would be $S = 0$ but due to the significant anisotropy of the Mn(III) it is here difficult to conclude as the χT product below 25 K seems to clearly extrapolate below 3 cm^{3}K/mol suggesting a ground state lower than 2.

3.8 Structure and Magnetism of $[Mn^{III}_3(\mu_3\text{-}O)(salox\text{-}H)_3(ClO_4)(Phpy)_3]$, 10

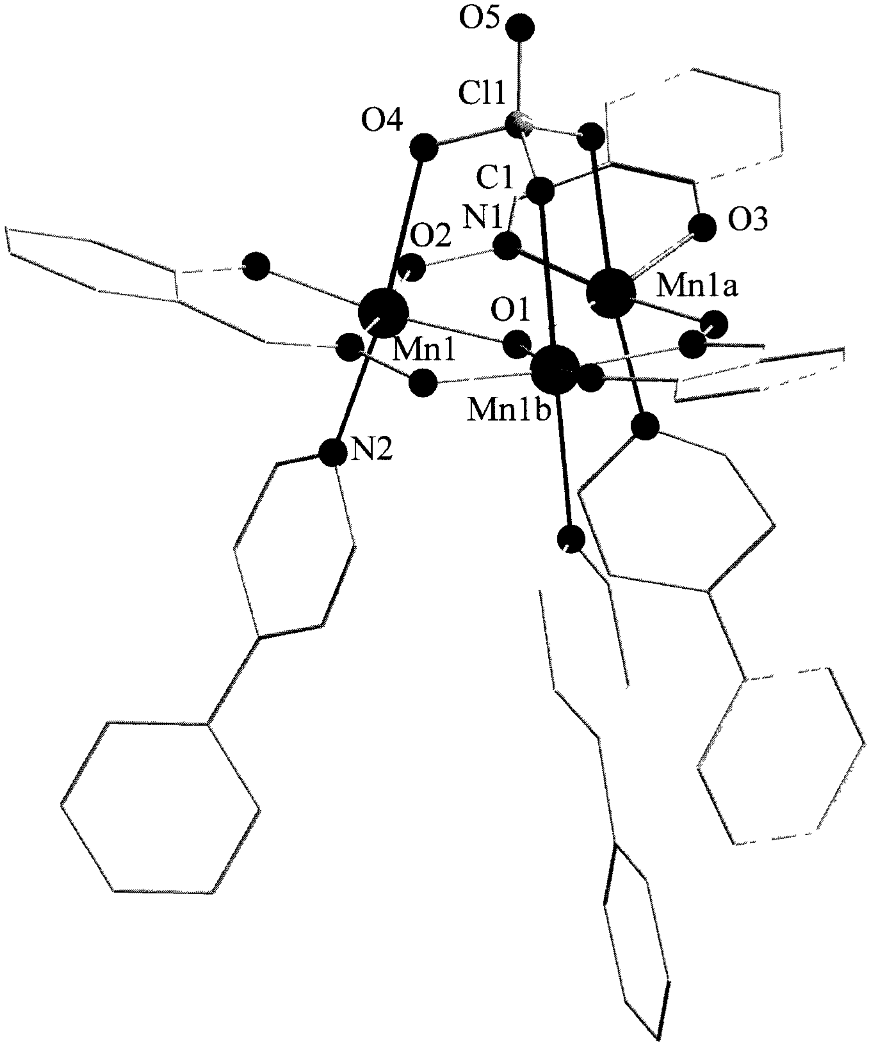

Figure 35. Molecular structure of $[Mn^{III}_3(\mu_3\text{-}O)(salox\text{-}H)_3(ClO_4)(Phpy)_3]$, **10**.

Complex **10**, $[Mn^{III}_3(\mu_3\text{-}O)(salox\text{-}H)_3(ClO_4)(Phpy)_3]$, consists of three Mn(III) ions arranged in an equilateral triangular configuration linked by a central μ_3-oxygen (Figure 35). This complex is similar to **6**, however the equatorial ligand is switched to a class B ligand (Leq.= salox-H^{-2}). The Mn_3 core is surrounded by three salox^{-2} ligands which forms flexible six-membered chelating rings as shown in green bonds in Figure 35. However, small torsion angle of 14.3° was observed along the oxime bridges [Mn-N-O-Mn]. The top and bottom face remains unchanged as **6**, which is weakly linked to a perchlorate and three phenylpyridine molecules, respectively. The oxygen out of the Mn_3 plane is 0.28 Å and the Mn...Mn distance is 3.25 Å.

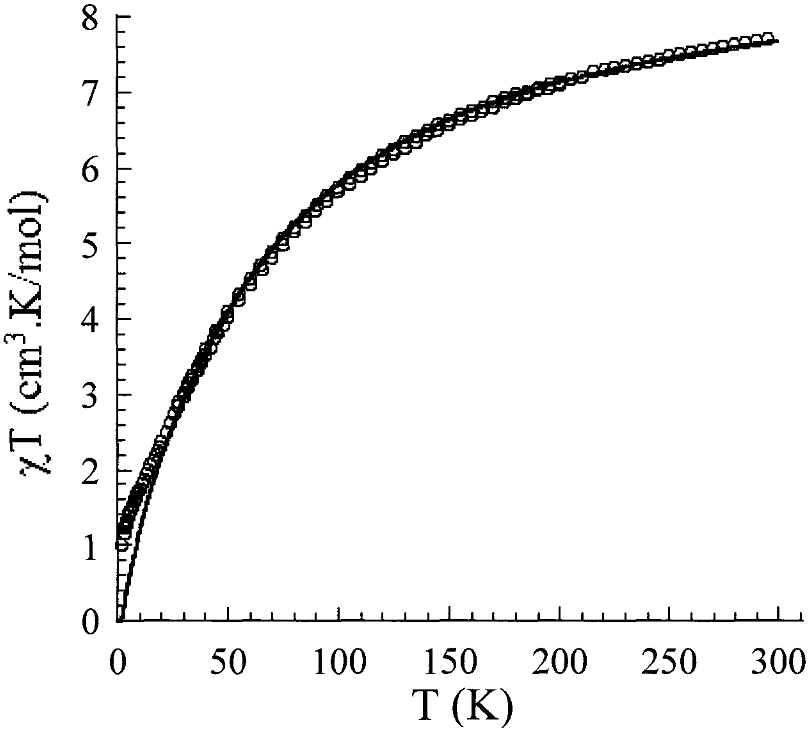

Figure 36. Plot of χT *vs.* T for complex **10** at 1000 Oe. The solid line is the best fit obtained with the Heisenberg trinuclear model.

At room temperature, the χT product is 7.7 cm^3K/mol. When the temperature is lowered, the χT product decreases reaching 1.0 cm^3K/mol at 1.8 K indicating strong antiferromagnetic interactions between $S = 2$ Mn(III) spins (Figure 36). Down to 28 K, the experimental data have been fitted using a isotropic Heisenberg $S = 2$ regular triangle model. The best set of parameters found is J/k_B = -5.6(1) K and g = 1.99(1) as expected for Mn(III) sites (red line shows the fit down to 28 K). The ground state of the Mn_3 unit is not completely clear. In a pure Heisenberg model the ground state would be S = 0 but due to the significant anisotropy of the Mn(III) it is here difficult to conclude as the χT product below 25 K seems to clearly extrapolate below 3 cm^3K/mol suggesting a ground state lower than 2.

3.9 Structure and Magnetism of $[Mn^{III}_3(\mu_3\text{-}O)(salox\text{-}Me)_3(ClO_4)(Phpy)_3]{\bullet}0.5MeCN$, 11

Complex **11**, $[Mn^{III}_3(\mu_3\text{-}O)(salox\text{-}Me)_3(ClO_4)(Phpy)_3]{\bullet}0.5MeCN$, consists of three Mn(III) ions arranged in an equilateral triangular configuration (Figure 37). Structurally, complex **11** is similar to **10**, however the only difference is the substituent on the C1 atom, which is a methyl group instead of a hydrogen atom. All three Mn ions possess a distorted octahedral geometry with C_3 symmetry linked *via* the central μ_3-oxide atom (O1). The Mn...Mn distance for **4** is 3.26 Å as shown in Table 5. The inorganic core $[Mn^{III}_3(\mu_3\text{-}O)]$ is surrounded by three equatorial ligand ($Leq.^{-2}$ = $salox\text{-}Me^{-2}$) which is arranged in a near-planar fashion coordinating to the three Mn(III) ions through the oxime bridges [Mn-N-O-Mn]. The $salox\text{-}Me^{-2}$ ligand generates six-membered coordination rings which are highly flexible. The methyl group on the C1 atom of the $salox\text{-}Me^{-2}$ ligand, generates a large torsion angle of 44.3° along the Mn-N-O-Mn moiety. The top and bottom face of the core is similar to **6** and **10**, therefore these compounds can be used in the structural and magnetic comparative studies. All three Mn ions are in the 3+ oxidation state and this is evident with the Jahn-Teller elongation along the axial positions of the distorted octahedral Mn ions. The central μ_3-oxygen is 0.28 Å below the Mn_3 plane resulting in a near parallel arrangement of the Jahn-Teller axis.

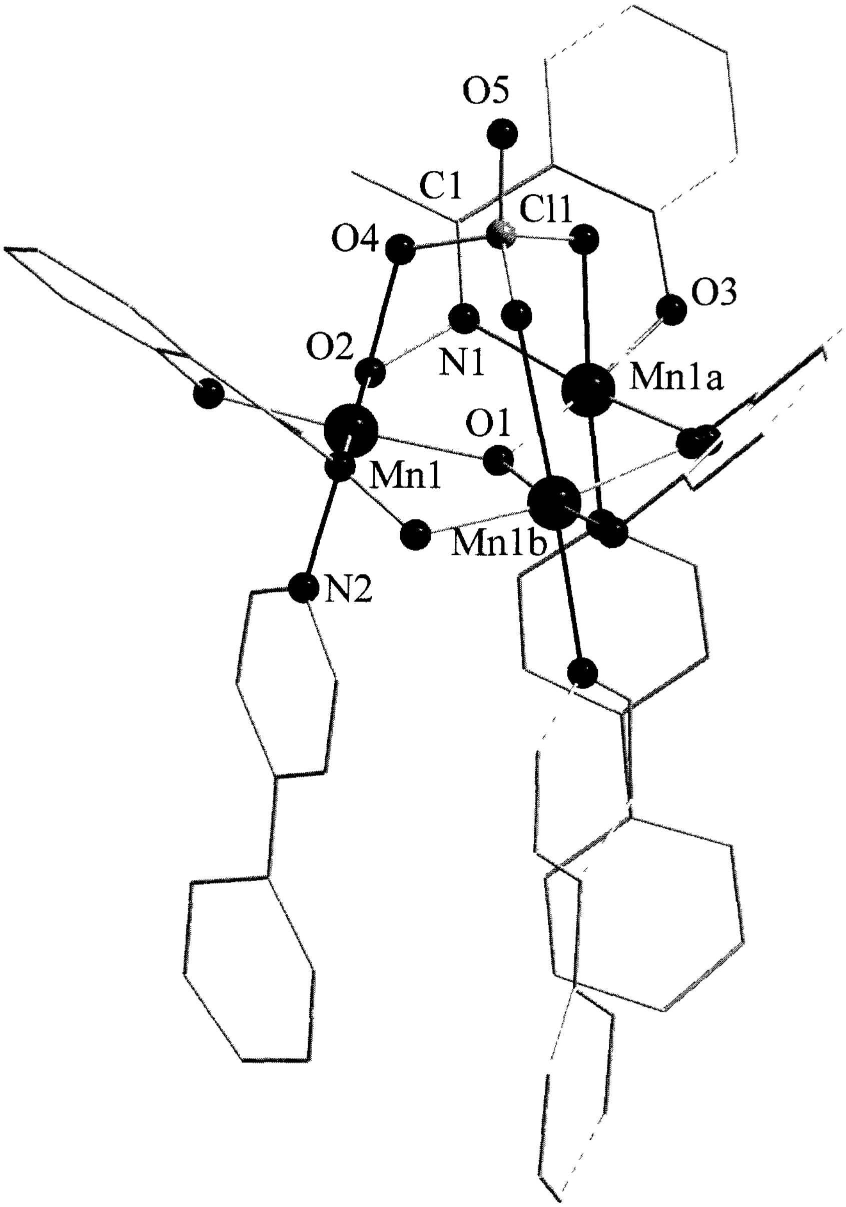

Figure 37. Molecular structure of $[Mn^{III}_3(\mu_3\text{-}O)(salox\text{-}Me)_3(ClO_4)(Phpy)_3]\cdot 0.5MeCN$, **11**.

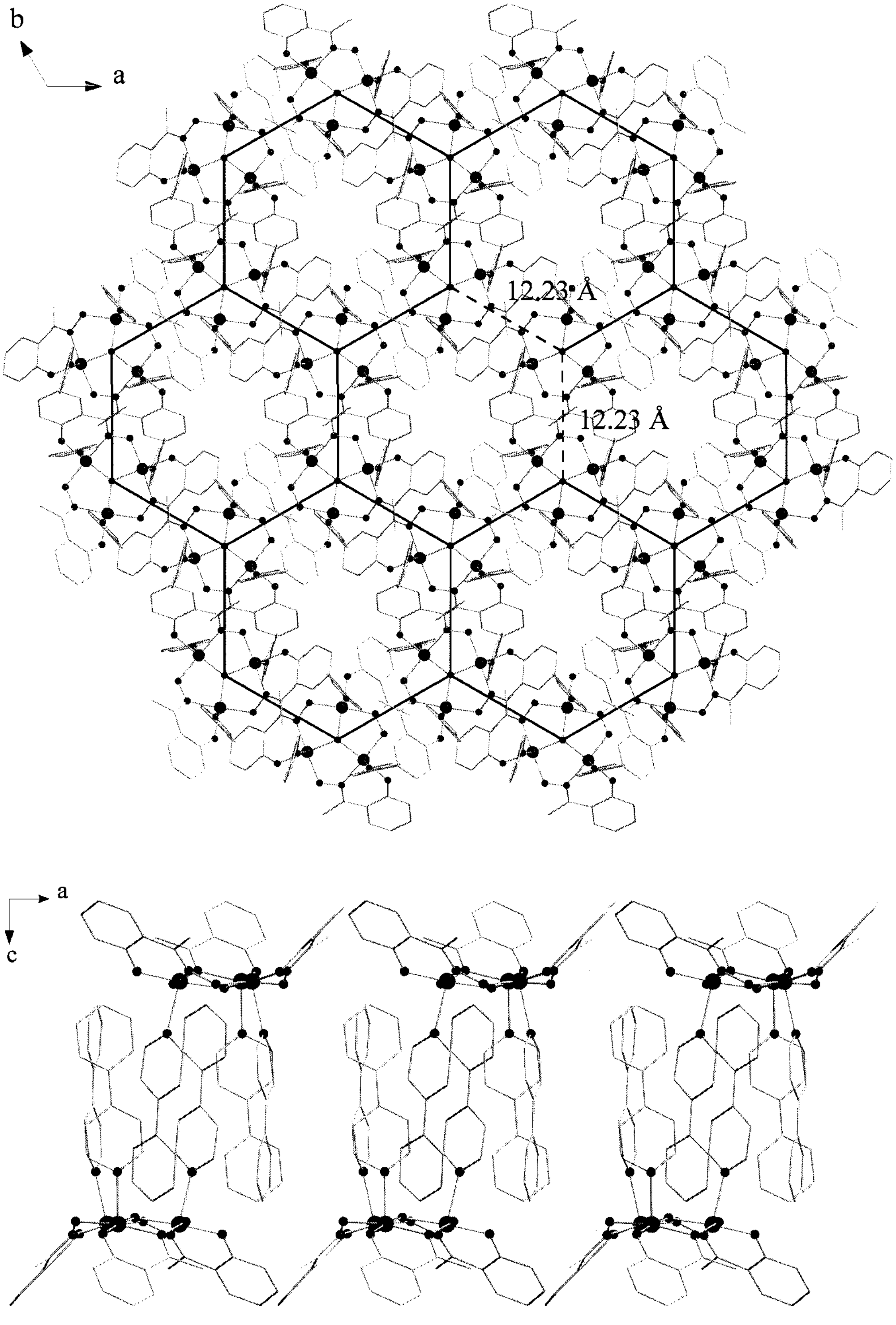

Figure 38. Crystal packing arrangements of **11** along the *c*- axis (top) and the *b*- axis (bottom). Mn(III) ions are presented in purple, O in red and N in blue. Hydrogen atoms and the perchlorate anions are omitted for clarity.

The crystal packing arrangements of **11** resemble a biological lipid bilayer along the *a*- and *b*-axes and a honey comb shape along the *c*- axis. The molecules in the crystal lattice are oriented towards each other with the perchlorate anions facing outward and the axial ligands facing inward as shown in Figure 38. They are closely stacked while minimizing steric hindrance.

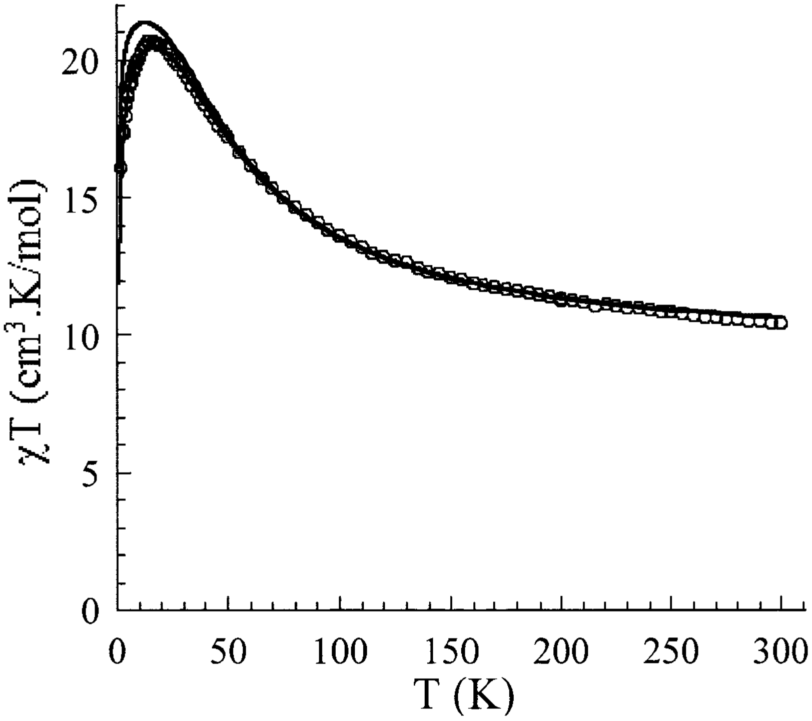

Figure 39. Plot of χT *vs.* T for complex **11** at 1000 Oe. The solid line is the best fit obtained with the Heisenberg trinuclear model.

The χT product for **11** at room temperature is 10.5 cm^{3}K/mol. When the temperature is lowered, the χT product at 1000 Oe increases reaching 20.8 cm^{3}K/mol at 21 K indicating significant ferromagnetic interactions between $S = 2$ Mn(III) spins (Figure 39). The χT product below 21 K decreases to 16.1 cm^{3}K/mol at 1.8 K. Using the Hamiltonian (eq. 3), the application of the Van Vleck equation[23] to the Kambe's vector coupling scheme[24], allows the determination of an analytical expression of the magnetic susceptibility and the fitting of experimental data. Considering the data above 25 K, the best set of parameters found is $J/k_B = 5.7(1)$ K and g =

2.00(2). This result suggests an $S_T = 6$ spin ground state for **11**. In order to fit the χT product below 21 K, intermolecular interactions were introduced in the frame of the mean field theory. The following definition of the susceptibility was used:

$$\chi = \frac{\chi_0}{1 - \frac{2zJ'}{Ng^2\mu_B^2}\chi_0} \qquad \text{Eq. 4}$$

where χ_0 is the susceptibility of an isolated Mn(III) triangle obtained from the equation 4 , z is the number of nearest neighbors and J' is the intermolecular magnetic interaction between Mn_3 units.[30] As shown in Figure 39 (red line), an excellent fit has been achieved with $J/k_B = +5.20(5)$ K, $zJ'/k_B = -0.029(2)$ K and $g = 2.03(2)$. Nevertheless the inter-triangle interactions are certainly overestimated by this modeling approach as their estimation also contains the effects of the magnetic anisotropy brought by the Mn(III) metal ions (vide infra).

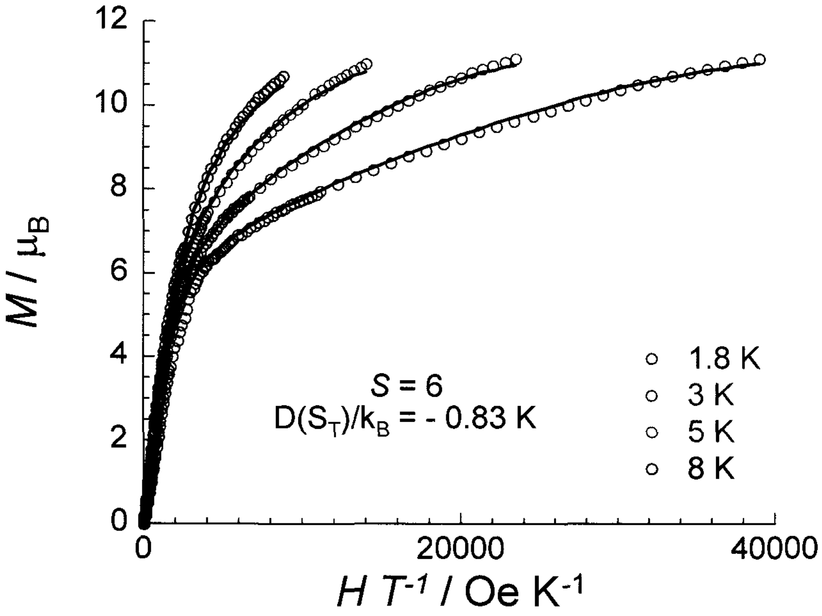

Figure 40. Reduced magnetization plot from 1.8 K to 8 K with fit line.

The field dependence of the magnetization in the 1.8 – 8 K range was also measured and showed that the magnetization is not saturated at 7 T reaching 11.2 μ_B while 12 μ_B is expected for an S_T = 6 spin ground state. The absence of saturation suggests the presence of a significant magnetic anisotropy. The excited states cannot contribute to this behavior as the S = 5 excited state is around 62.4 K (12 J/k_B) above the ground state in energy. The *M vs. H/T* plot confirms the presence of an anisotropy intrinsic to Mn(III) metal ions as the data are not superposed on a single master-curve as expected for isotropic systems with a well defined spin ground state. In order to model the *M vs. H* data below 8 K, a macro-spin approach was used considering that only the S_T = 6 spin ground state is thermally populated below 8 K. This is a relatively good approximation, taking into account that the S = 5 excited state is far above the ground state in energy. Therefore, the following macro-spin Hamiltonian was considered:

$$H = D_{S_I} S_T^2 \qquad \text{Eq. 5}$$

As shown in Figure 40 by the lines superposed to the experimental data at 1.8, 3, 5 and 8 K, an excellent fit was achieved with $D(S_T)/k_B$ = -0.83(5) K and g = 2.00(2). Using this result, the local D_{Mn} parameter of each Mn(III) metal ions was estimated at -3.06 K[31] and the χT vs T data were calculated using a general procedure developed by J. M. Clemente-Juan and co-workers (MAGPACK program[32]), with the following anisotropic Heisenberg Hamiltonian:

$$H = -2J\left(S_1 \bullet S_2 + S_2 \bullet S_3 + S_1 \bullet S_3\right) + 3D_{Mn}S_{z,Mn}^2 \qquad \text{Eq. 6}$$

Fixing the parameters to the following values: J/k_B = +5.20 K, D_{Mn}/k_B = -3.06 K and g = 2.03, the magnetic susceptibility was obtained (blue line, Figure 39) and was superposed to the experimental data. As shown, this model does not reproduce the data well below 30 K and therefore inter-triangle magnetic interactions had to be considered and were estimated at zJ'/k_B = -0.02 K. With this value, the experimental data could be perfectly simulated as shown by the red line in Figure 39.

The energy diagram was calculated for the two lowest spin states (S_T = 6 and S = 5) as shown in Figure 41. As expected, even with the introduction of magnetic anisotropy, the two levels are well separated in energy with a minimum value of 41.9 K. The energy barrier on the ground state is 29.7 K which is in excellent agreement with the energy gap calculated from $D(S_T)$ and estimated at $D(S_T)\ S_T^2/k_B$ = 29.7 K. This result shows the self consistency of our models. However, no hysteresis loops were observed on the *M vs. H* data above 1.8 K with sweep-rate used in a traditional SQUID magnetometer (100 – 200 Oe/min).

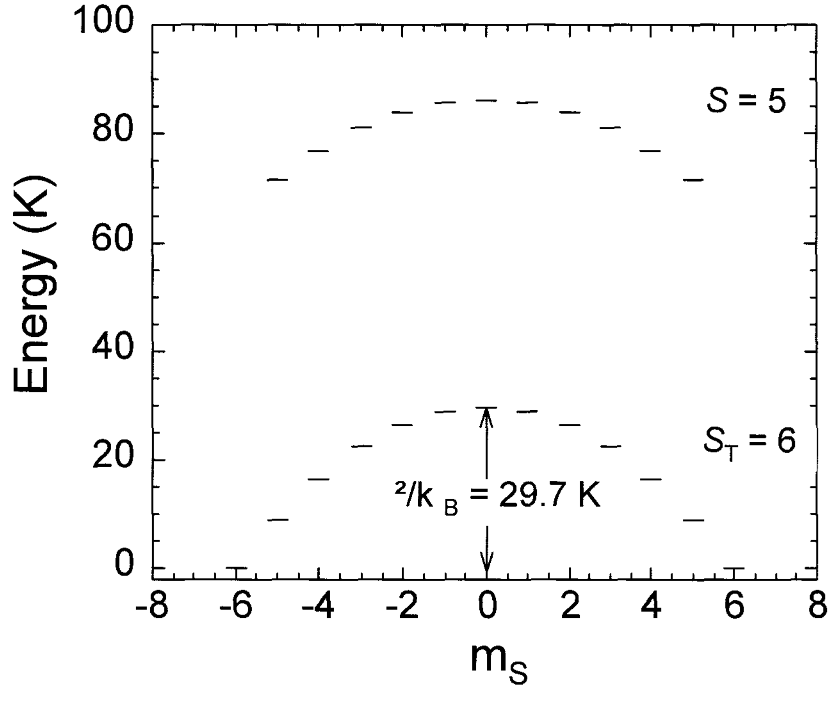

Figure 41. Energy diagram for **11** calculated for the two lowest spin states (S_T = 6 and S = 5) shows the two levels are well separated in energy.

Nevertheless, the ac susceptibility of this compound was measured in zero dc field. At low temperatures below 8 K (for frequency around 1500 Hz), slow relaxation of the magnetization was observed based on the appearance of a frequency dependent out-of-phase signal. The ac susceptibility as a function of the frequency at different temperatures was also measured in order to follow the relaxation time in a clean manner. This feature (shape and frequency dependence) is indicative of SMM behaviour.

The relaxation time could be deduced between 2.4 and 5.8 K (Figure 42). In this temperature domain and in the ac frequency experimental range, the relaxation time was thermally activated with an estimated energy gap of 39 K and a pre-exponential factor of the Arrhenius law (τ_0) of approximately 7.3 10^{-8} s. The energy gap deduced from the dynamic data (39 K) is without doubt higher than the expected thermal barrier estimated around 30 K by the static measurements and their models. In most cases, the presence of thermally activated quantum tunnelling of the magnetization decreases the energy gap. Here, the difference between the theoretical and experimental energy gap is not clear but could be a signature of the inter-triangle magnetic interactions that could enhance the energy gap in a similar way as is observed in SCM system.

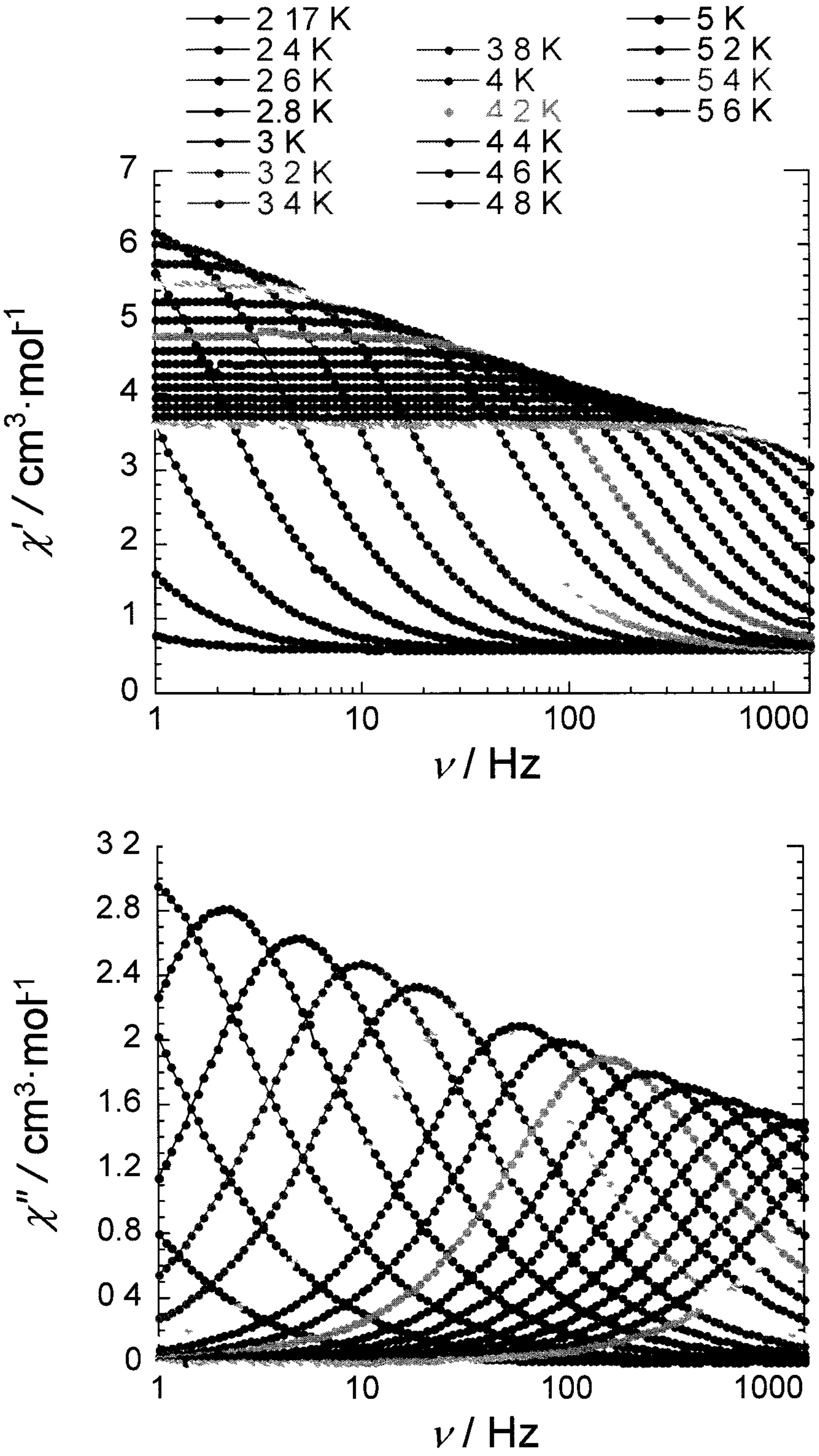

Figure 42. *Top* ac magnetic susceptibility χ' as a function of frequency at temperature ranging from 2.17 to 5.8 K. *Bottom* χ'' out-of-phase component.

3.10 Discussion

Eight triangular Mn_3 complexes have been characterized structurally and magnetically. Complex **4 - 9** was synthesized using class A ligands (H_2dmo and H_2cpo) and **10 - 11** was synthesized using class B ligand (H_2salox-H and H_2salox-Me). The general procedure for the synthesis of triangular complexes is the addition of 1 equiv. of $Mn(ClO_4)_2 \bullet 6H_2O$, 1 equiv. of equatorial ligand (L_{eq} = cpo^{-2}, dmo^{-2}, salox-Me^{-2} and salox-H^{-2}) and 1 equiv. of axial ligand (L_{ax} = MeOH, EtOH, imidazole and 4-phenylpyridine) to a solution of Et_3N and solvent (MeOH, EtOH, MeCN, Et_2O) as shown in equation 7.

$$1Mn(ClO_4)_2 \bullet 6H_2O + 1H_2L_{eq.} + 1L_{ax.} \xrightarrow[\text{Solvent}]{Et_3N} [Mn^{III}(\mu_3\text{-}O)(L_{eq.})_3(ClO_4)(L_{ax.})_3] \bullet x\text{Solvent} \quad \text{Eq. 7}$$

The equatorial ligands allow for the incorporation of one ligand on each edge of the $Mn(III)_3$ triangular core. The $Mn(ClO_4)_2 \bullet 6H_2O$ was chosen as the metal source due to the ClO_4^- anion which acts as a tripodal chelating agent capping the three Mn(III) ions from the top face. The Mn(II) salt slowly oxidizes to Mn(III) under basic conditions and such coordination environment. Triethylamine is essential in facilitating the deprotonation of the ligand which then readily coordinates to the free metal ions in solution. Furthermore, in the presence of Et_3N, the hydrated metal provides a source of oxygen for the formation of the μ_3-oxide. By varying the base to NaOH or Et_4NOH, the formation of powder was observed and X-Ray quality crystals could not be isolated. Various other solvents, such as iPrOH, CH_2Cl_2 and DMF, were used in an attempt to alter the packing arrangement of the molecules; however, crystallization was not observed. Sodium azide was added to the reaction mixture in order to replace the axial ligands and dimerize or polymerize the $Mn(III)_3$ units *via* end-to-end or end-on coordination as demonstrated by S. Gao[33] and co-workers. Similarly, a known Mn_8 complex, reported by Brechin *et. Al.,* was isolated in which the $Mn(III)_3$ units dimerized with Mn(II) ions capping both ends *via* end-on azide molecules.[34]

Complexes **4** – **9**, consists of five-membered coordination rings, display relatively low torsion angle ranging from 4.5° to 21.0° as shown in Table 5. This structural feature is clearly observed for all six complexes. Complex **10** consists of a six-membered coordination ring, also exhibits low torsion angle of 14.3° due to the substituent on the C1 atom. The hydrogen atom on the C1 carbon interacts with the O2 atom of the –NO group of the oxime *via* hydrogen bonding with a distance of 2.33 Å, thus producing a near planar molecule. By deliberately switching the substituent on the C1 atom to a larger group, methyl, a larger torsion angle of 44.3° was observed for complex **11**. This structural feature was also observed with the ethyl group on the C1 atom as shown by E. Brechin[27b], H-L. Tsai[27c] and co-workers giving rise to large torsion angles averaging 42°. The selected bond distances and bond valence sum calculations for **4** - **11** are shown in Table 7 and Table 8, respectively.

Table 6. Selected interatomic distances (Å), μ_3- oxide out-of-plane distances (Å) and dihedral angles (°) for complexes **4** - **11**.

Complex	Mn(1)… Mn(1a)	O(1) out-of-plane	Mn-N-O-Mn
$[Mn^{III}_3(\mu_3\text{-}O)(cpo)_3(ClO_4)(MeOH)_3]$ **4**	3.26	0.30	18.6
$[Mn^{III}_3(\mu_3\text{-}O)(cpo)_3(ClO_4)(Imz)_3]$ **5**	3.23	0.32	12.2
$[Mn^{III}_3(\mu_3\text{-}O)(cpo)_3(ClO_4)(Phpy)_3]$•4.5MeCN **6**	3.24	0.22	5.0
$[Mn^{III}_3(\mu_3\text{-}O)(dmo)_3(ClO_4)(MeOH)_3]$ **7**	3.24	0.21	6.4
$[Mn^{III}_3(\mu_3\text{-}O)(dmo)_3(ClO_4)(EtOH)_3]$ **8**	3.25	0.20	4.5
$[Mn^{III}_3(\mu_3\text{-}O)(dmo)_3(ClO_4)(Imz)_3]$ **9***	3.23-3.25	0.28	21.0/19.7/12.8
$[Mn^{III}_3(\mu_3\text{-}O)(salox\text{-}H)_3(ClO_4)(Phpy)_3]$ **10**	3.25	0.28	14.3
$[Mn^{III}_3(\mu_3\text{-}O)(salox\text{-}Me)_3(ClO_4)(Phpy)_3]$ •0.5MeCN **11**	3.26	0.28	44.3
$[Mn^{III}_3(\mu_3\text{-}O)(salox\text{-}Me)_3(ClO_4)(2,4'\text{-}bpy)_3]$•0.5MeCN[α]	3.26	0.27	44.2
$[Mn^{III}_3(\mu_3\text{-}O)(salox\text{-}Et)_3(ClO_4)(MeOH)_3]$[β]	3.24	0.18	42.1

*Has no C_3 symmetry axis. [α]H-L Tsai and co-workers. [β]E. Brechin and co-workers.

Table 7. Selected bond distances (Å) for complexes **4** - **11**.

Complex	Mn(1)-O(1)	Mn(1)-O(2)	Mn(1)-N(1)	Mn(1)-O(3)	Mn(1)-O(4)	Mn(1)-O(6)	Mn(1)-N(2)
4	1.906(2)	1.914(3)	1.984(4)	1.876(3)	2.60	2.208(3)	-
5	1.893(2)	1.931(4)	1.981(5)	1.856(5)	2.68	-	2.214(6)
6	1.886(8)	1.934(3)	1.983(3)	1.841(3)	2.62	-	2.300(4)
7	1.885(6)	1.912(2)	1.995(3)	1.860(2)	2.66	2.217(3)	-
8	1.886(2)	1.913(3)	1.995(3)	1.858(3)	2.68	2.237(3)	-
9*	1.89- 1.894(3)	1.91- 1.947(3)	1.98- 1.995(3)	1.85- 1.873(3)	2.63- 2.70	-	2.20- 2.206(3)
10	1.897(2)	1.903(4)	1.996(4)	1.875(4)	2.51	-	2.229(8)
11	1.905(8)	1.913(3)	1.987(3)	1.866(2)	2.56	-	2.277(3)

* Has no C_3 symmetry axis.

Table 8. Bond valence sum calculation with the suggested oxidation state for **4** - **11**.

Complex	Mn(II)	Mn(III)	Mn(IV)	Ox. state
4	3.19	2.96	3.06	3
5	3.29	3.06	3.12	3
6	3.26	3.03	3.10	3
7	3.23	2.99	3.08	3
8	3.21	2.97	3.06	3
9	3.20	2.98	3.04	3
10	3.29	3.07	3.13	3
11	3.24	3.02	3.08	3

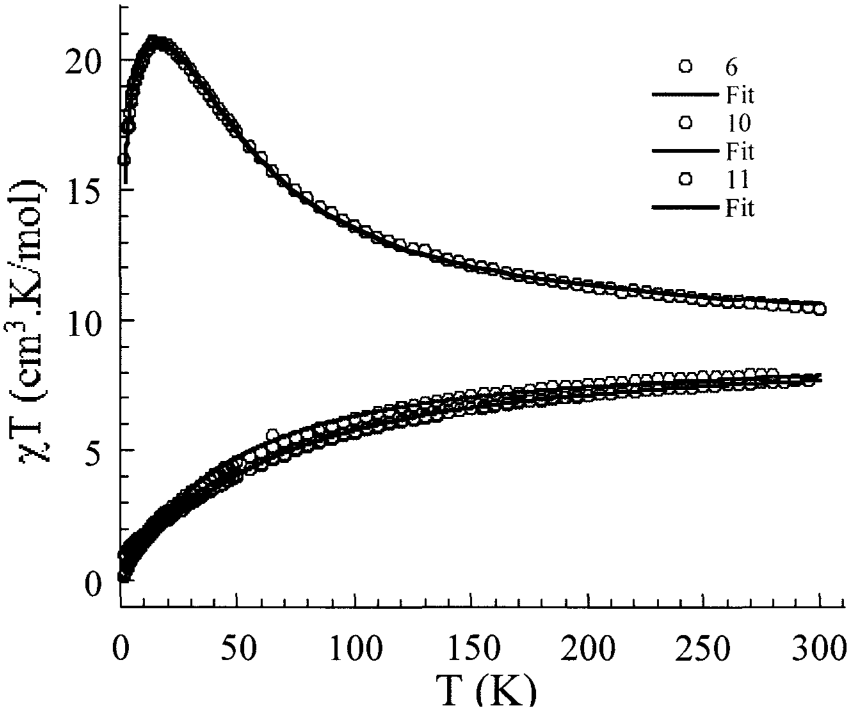

Figure 43. Comparative analysis of **6**, **10** and **11**.

Comparative analysis of complexes **6**, **10** and **11** showed a clear magneto-structural correlation (Figure 43). In order to obtain an accurate comparison, variables such as the axial ligand 4-phenylpyridine, the capping anion ClO_4^{-1} and the μ_3-oxide were deliberately kept consistent. This allowed us to study the role of the equatorial ligands with respect to the planarity of the core and the torsion angles imposed by the substituent on the C1 atom. This approach helped answer some of the fundamental questions regarding the structural aspects and the responsive magnetic behaviour of the $Mn(III)_3$ triangle units. Complex **6** consisted of three five-membered rings formed by the coordination of the cpo^{-2} ligands encompassing the $Mn(III)_3$ magnetic core. The latter displayed a relatively low torsion angle of 5.0° as a result of its inability to bend due to the physical constraints of the five-membered coordination ring. The overall consequence was a near planar molecule with the μ_3-Oxide out of the $Mn(III)_3$ plane by 0.22 Å. This structural feature was also observed with the substitution of the axial ligands from 4-phenylpyridine to MeOH, **7** and imidazole, **8** resulting in torsion angles of 18.6° and 12.2°, as well as exchange constants of J = -3.1K and J = -6.3K, respectively. Initially, we suspected that by introducing a large axial ligand, such as 4-phenylpyridine, a distortion in the triangle would be induced which was in fact observed in the structural analysis of **9**. The five-membered coordination rings formed by the cpo^{-2} ligand had no significant effect on the nature of the interactions leading to J = -4.2K. Furthermore, complexes **7**, **8** and **9** were synthesized with a similar equatorial ligand, H_2dmo, to study whether the cyclopentyl group on C2 had any effect on the planarity of the $Mn(III)_3$ core. These complexes consisted of MeOH, EtOH and imidazole as the axial ligand, respectively. Compound **10** was synthesized with the equatorial ligand H_2salox-H which formed a six-membered coordination ring with two adjacent Mn(III) ions in the $Mn(III)_3$ triangle. This ligand was specifically chosen to study the effects of a six-membered ring with H on the C1 atom, which provided greater flexibility to the –NO bridging moiety as shown in Figure 44.

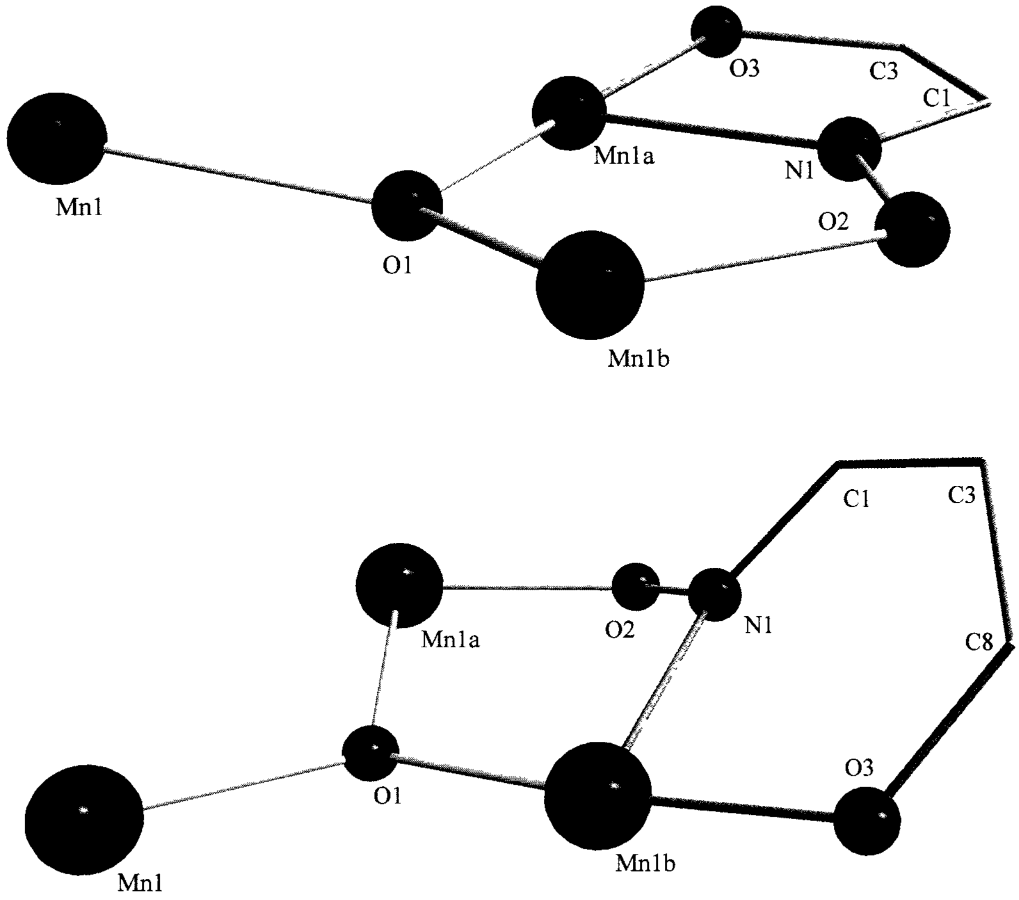

Figure 44. *Top:* five-membered coordination ring formed by the ligand and two Mn(III) ions. *Bottom:* six-membered coordination ring formed by the ligand and two Mn(III) ions.

The torsion angle observed for complex **10** was 14.3° which is larger than the angle in **6** by 9.3°. Nonetheless, magnetically, both complexes were similar; they both exhibited anti-ferromagnetic interactions. By switching the equatorial ligand to H_2salox-Me, complex **11** was isolated in which the methyl group on the C1 atom replaced the H. Comparative studies were performed where all other variables were kept constant while varying the substituent on the C1 atom. As per our expectations, the resulting structure had a high torsion angle of 44.3°, a difference of 30.0° relative to **10**, inducing ferromagnetic coupling interactions with J = +5.7 K (Table 9). A structural distortion was observed in the crystal structure in which the three salox-Me^{-2} ligands bend towards the $\mathrm{ClO_4}^{-1}$ anion (Figure 37). Analogous ferromagnetic complexes were reported by H-L. Tsai and co-workers and E.K. Brechin and co-workers demonstrating similar structural features with torsion angles of 44.2° and 42.1°, respectively. D.N. Hendrickson[27c] and co-workers have also isolated a ferromagnetic $\mathrm{Mn(III)_3Zn(II)_2}$ heterometallic complex using the salox-H^{-2} ligand exhibiting a large torsion angle of 32.1°. In this situation, the high torsion angle was induced by the axial Zn(II) ions linked *via* azide bridging molecules, hence introducing ferromagnetism to the system. Evidently, there are two determinants of ferromagnetism in $\mathrm{Mn(III)_3}$ triangles; a six-membered coordination ring is essential in giving flexibility which in turn gives rise to the second determinant, a large dihedral angle along the oxime bridge, Mn-NO-Mn (Figure 45).

Table 9. Magnetic fit parameters for complexes **4** - **11**.

Complex	J (K)	*g*	χT*	S_T
$[\mathrm{Mn^{III}}_3(\mu_3\text{-O})(\mathrm{cpo})_3(\mathrm{ClO_4})(\mathrm{MeOH})_3]$ **4**	-3.1(1)	1.99(1)	8.4	0-2
$[\mathrm{Mn^{III}}_3(\mu_3\text{-O})(\mathrm{cpo})_3\ (\mathrm{ClO_4})(\mathrm{Imz})_3]$ **5**	-6.3(1)	2.00(2)	7.2	0-2
$[\mathrm{Mn^{III}}_3(\mu_3\text{-O})(\mathrm{cpo})_3(\mathrm{ClO_4})(\mathrm{Phpy})_3]$•4.5MeCN **6**	-4.2(1)	1.98(2)	8.1	0-2
$[\mathrm{Mn^{III}}_3(\mu_3\text{-O})(\mathrm{dmo})_3(\mathrm{ClO_4})(\mathrm{MeOH})_3]$ **7**	-5.1(1)	1.99(1)	7.8	0-2
$[\mathrm{Mn^{III}}_3(\mu_3\text{-O})(\mathrm{dmo})_3(\mathrm{ClO_4})(\mathrm{EtOH})_3]$ **8**	-5.2(1)	1.99(1)	7.8	0-2
$[\mathrm{Mn^{III}}_3(\mu_3\text{-O})(\mathrm{dmo})_3(\mathrm{ClO_4})(\mathrm{Imz})_3]$ **9**	-7.7(1)	2.00(1)	7.4	0-2
$[\mathrm{Mn^{III}}_3(\mu_3\text{-O})(\text{salox-H})_3(\mathrm{ClO_4})(\mathrm{Phpy})_3]$ **10**	-5.6(1)	2.00(1)	7.7	0-2
$[\mathrm{Mn^{III}}_3(\mu_3\text{-O})(\text{salox-Me})_3(\mathrm{ClO_4})(\mathrm{Phpy})_3]$ •0.5MeCN **11**	+5.7(1)	2.00(2)	10.5	6
$[\mathrm{Mn^{III}}_3(\mu_3\text{-O})(\text{salox-Me})_3(\mathrm{ClO_4})(2,4'\text{-bpy})_3]$•0.5MeCN$^{\alpha}$	+3.6	1.95	9.8	6
$[\mathrm{Mn^{III}}_3(\mu_3\text{-O})(\text{salox-Et})_3(\mathrm{ClO_4})(\mathrm{MeOH})_3]^{\beta}$	+2.8	2.00	10.0	6

$^{\alpha}$H-L Tsai and co-workers. $^{\beta}$E. Brechin and co-workers. * $\mathrm{cm^3}$ K/ mol at 300 K

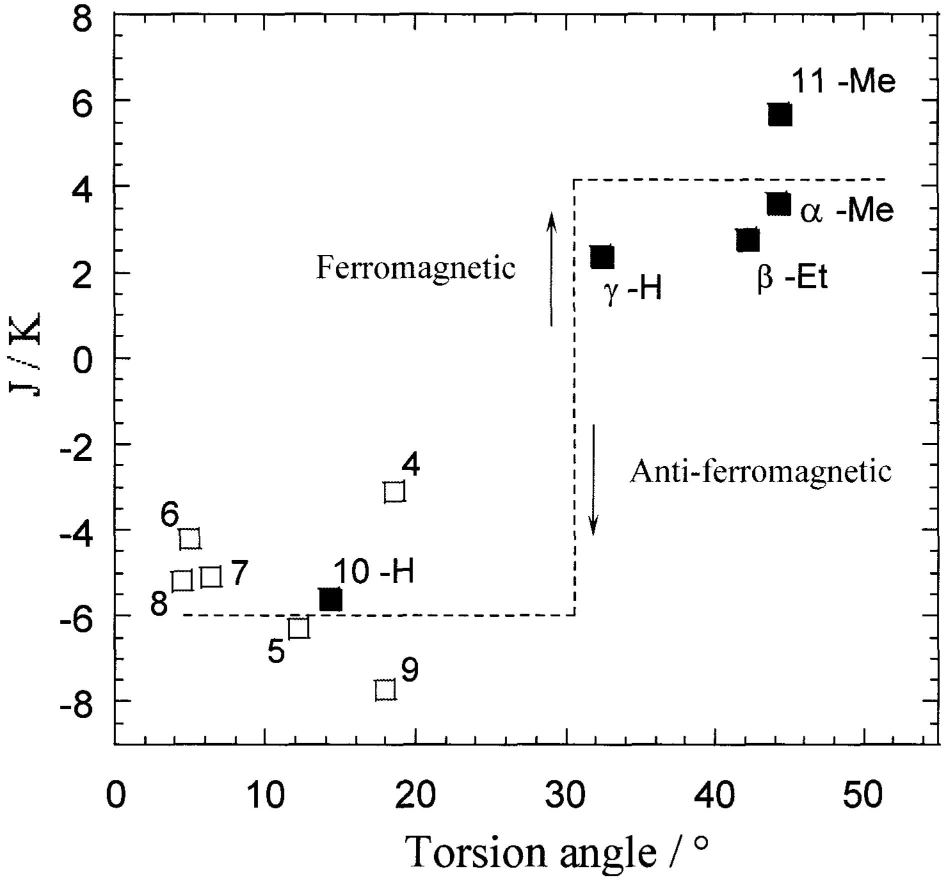

Figure 45. The magnetic interaction switch as a function of the torsion angles for **4 - 11** is depicted. Non-filled Squares and filled squares correspond to the five- and six-membered coordination rings, respectively. The symbols α, βand γ represent H-L Tsai, E. Brechin and D.N. Hendrickson and co-workers complex, respectively.

A systematic approach to the synthesis of manganese triangles has been explored in which the magnetic interaction between the metal centers of the triangle can be switched from antiferromagnetic to ferromagnetic by means of ligand exchange. Eight manganese complexes, sharing the triangular motif and the general formula $[Mn^{III}_3(\mu_3\text{-}O)(L_{eq.})_3(ClO_4)(L_{ax.})_3]$, have been synthesized and characterized structurally and magnetically. Complexes **4-10** show antiferromagnetic interactions due to relatively low torsion angles whereas complex **11** shows ferromagnetic interaction between the Mn(III) ions due to significantly larger torsion angles. In summary, a magneto-structural correlation was obtained where a tridentate ligand can form a six-membered coordination ring with the metal ions is essential in obtaining large torsion angles which in turn result in ferromagnetic interactions. In taking this work to the next level, axial positions of the compound can be controlled to incorporate bridging ligands (i.e. 4,4` bipyridine, N_3, CN and etc.) thereby forming dimeric complexes or even 1-D chains of repeating $Mn(III)_3$ units. This approach can ultimately increase the energy barrier of the molecule by essentially aligning the Mn_3 unit in a unidirectional fashion.

Chapter 4

4.1 Two Mn_3 Triangles Linked Side-on by Methoxides

Ferromagnetic manganese triangles are known to be excellent building blocks towards achieving larger energy barrier SMMs. This was demonstrated by E. Brechin and co-workers' Mn_6 cluster[13] which currently holds the record energy barrier for manganese SMMs with $S_T = 12$ and $U_{eff} = 86.4$ K. This Mn_6 cluster consists of two stacked $Mn(III)_3$ triangles bridged by oxime groups on the salox-Et^{2-} ligand. The stacked arrangement generates large amounts of anisotropy for this system, $D = -0.43$ cm^{-1} due to the Jahn-Teller axes aligned in a near-parallel fashion. Class B ligand, H_2salox-Et, was employed in the quest to break the record energy barrier. A larger substituent on the C1 atom of the oxime ligand (i.e. methyl group) is believed to generate larger torsion angles as shown in chapter 3. The ferromagnetic interaction between the Mn(III) ions gives rise to a large net spin ground state. The logic behind using a bulkier substituent on the C1 atom is to generate larger torsion angles between the Mn-N-O-Mn moieties which, in turn, possibly result in ferromagnetism. This is an essential ingredient in observing SMM behaviour in small molecules. This chapter focuses on linking Mn_3 triangles side on by methoxide molecules (Figure 46).

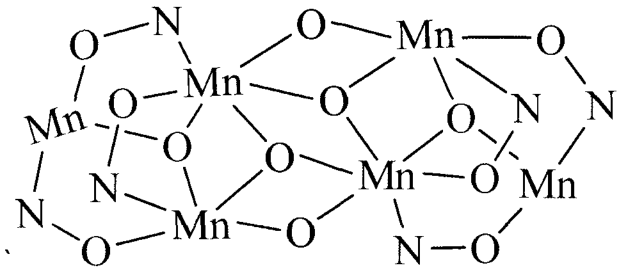

Figure 46. Two Mn_3 triangles linked side-on *via* four methoxide bridges.

4.2 Structure and Magnetism of [$Mn^{III}_4Mn^{IV}_2$(salox-Et)$_6$(μ_3-O)$_2$(μ_3-MeO)$_2$(μ-MeO)$_2$(MeOH)$_2$], 12

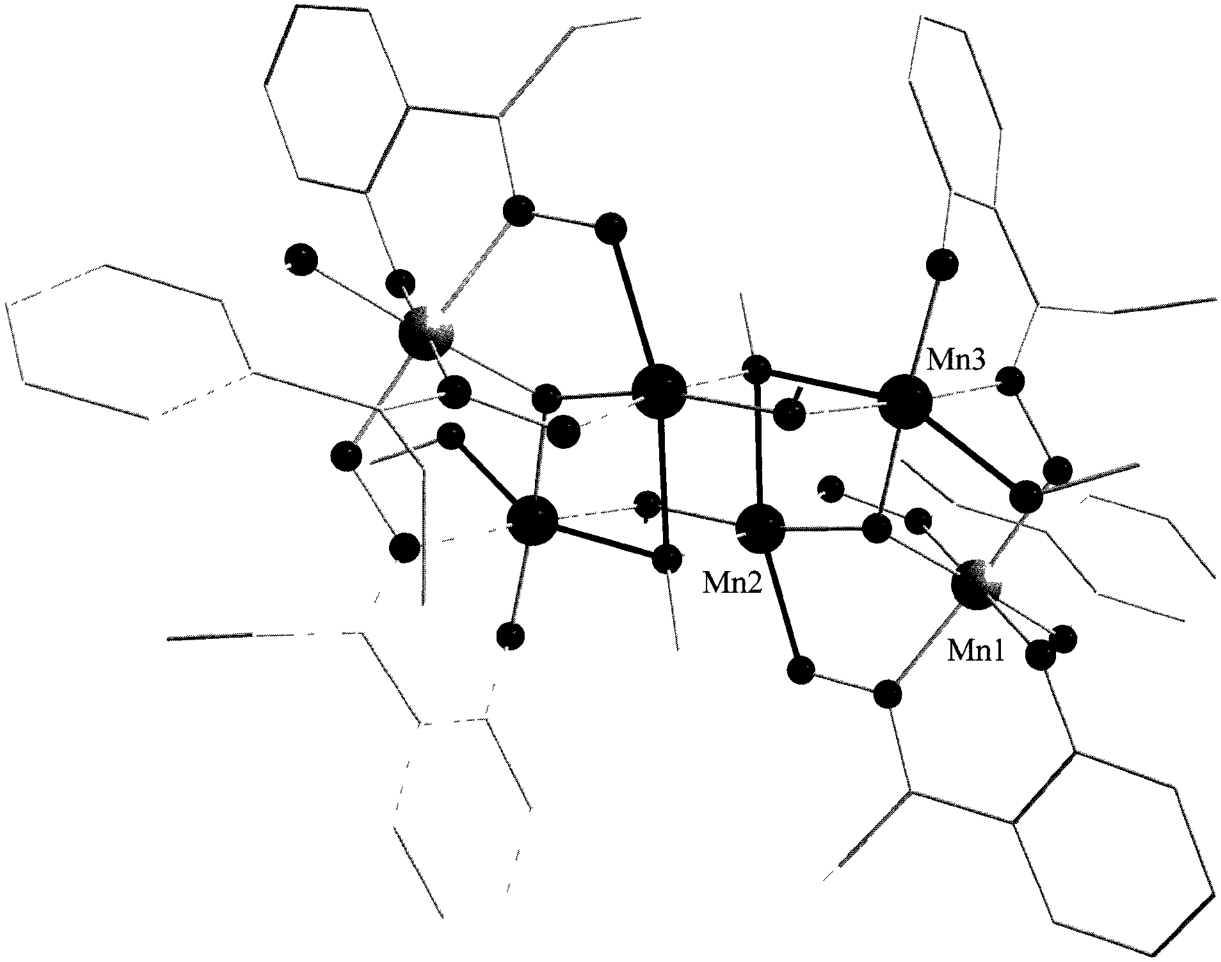

Figure 47. Molecular structure of [$Mn^{III}_4Mn^{IV}_2$(salox-Et)$_6$(μ_3-O)$_2$(μ_3-MeO)$_2$(μ-MeO)$_2$(MeOH)$_2$], **12**.

A unique mixed-valent complex **12**, [$Mn^{III}_4Mn^{IV}_2$(salox-Et)$_6$(μ_3-O)$_2$(μ_3-MeO)$_2$(μ-MeO)$_2$(MeOH)$_2$], was synthesized using a class B ligand, H_2salox-Et. It consists of two Mn_3 triangles linked side-on by two μ_3- and two μ-methoxides (Figure 47). The asymmetric Mn_3 triangle unit is interconnected by a central μ_3- oxide anion. The two Mn_3 inorganic cores are encapsulated by six salox-Et^{-2} ligands and two methanol molecules completing the distorted octahedral geometry of the Mn ions. The unit cell contains two unique crystallographic Mn_6 molecules oriented in slightly different directions. As mentioned in section 1.5, Class B ligands generate six-membered coordination rings which are highly flexible, hence producing larger torsion angles ranging from 9.3° to 46.2°. The oxidation states of the two terminal Mn ions are 4+ and the four internal Mn ions are 3+. These results were confirmed by charge consideration as well as bond valence sum calculations shown in Table 10. The four Mn(III) ions naturally possess the Jahn-Teller axes as shown in bold (Figure 47). The anisotropic axes of Mn(2) and Mn(3) are essentially perpendicular and hence cancel each other out. The four Mn(III) ions form a stable defective dicubane as shown in Figure 48 in turquoise bonds. This feature is exclusively formed by methoxides and oxides bridging moieties. The crystal packing arrangements along the b and a axes are depicted in Figure 49 and 50, respectively.

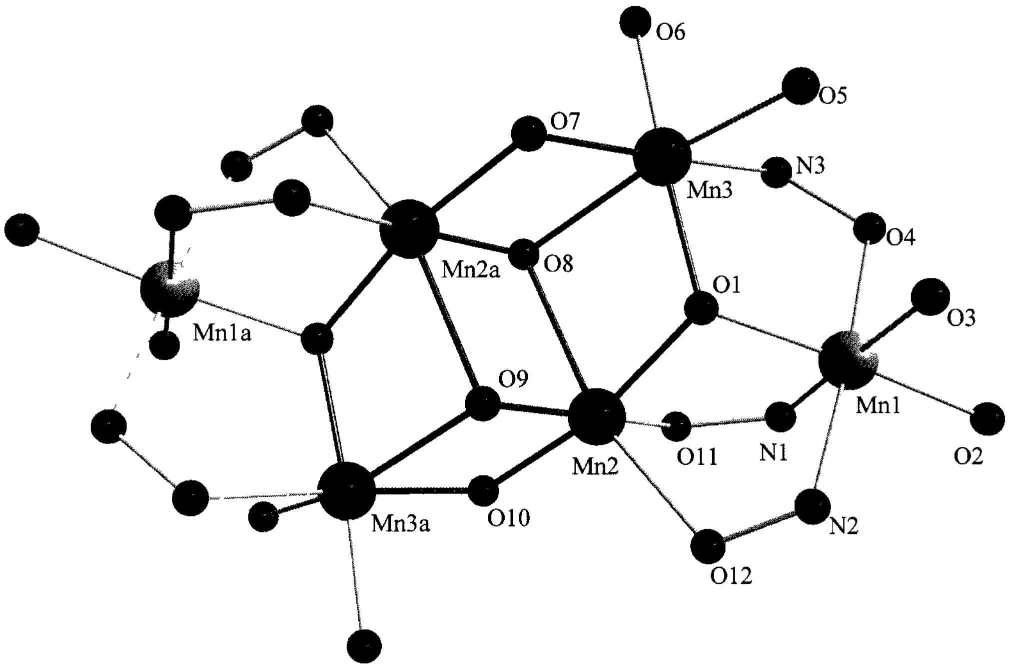

Figure 48. Core structure of **12** with atom labels and bold bonds depicting the defective dicubane.

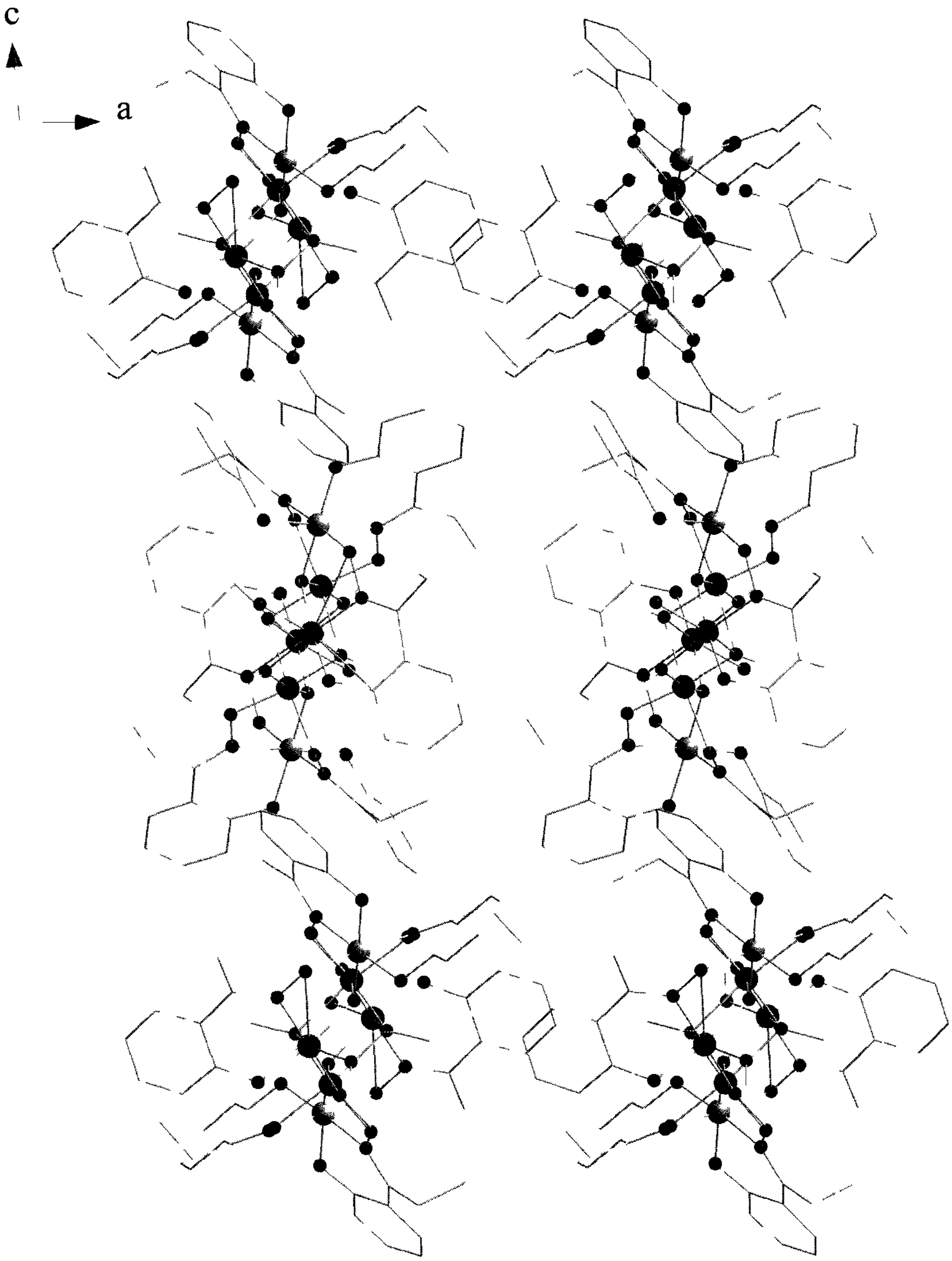

Figure 49. Packing arrangement of **12** along the *b* axis.

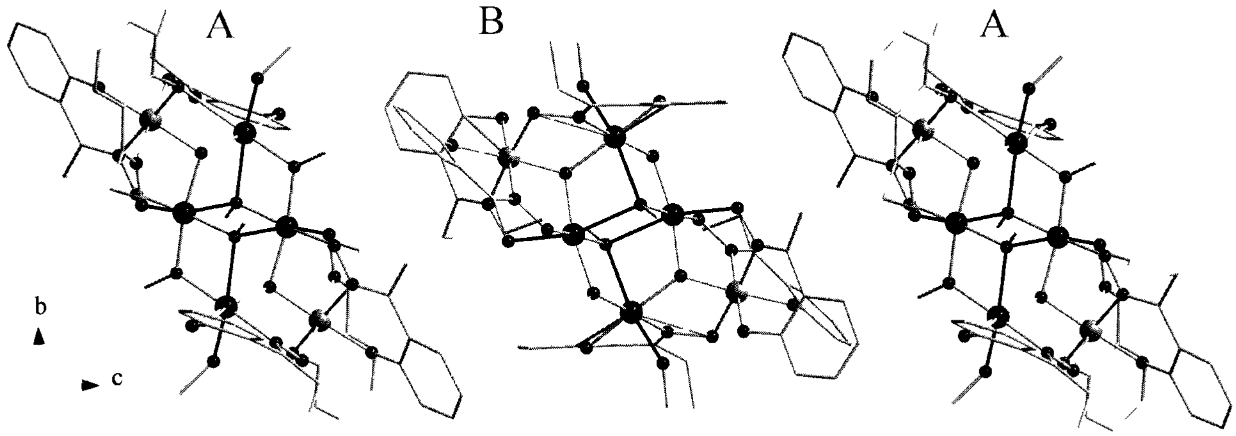

Figure 50. Packing arrangement of **12** along the *a* axis.

The χT product at 300 K is 18.9 cm^3K/mol which is close to the theoretical value for a mixed valent $Mn(III)_4$/ $Mn(IV)_2$ species (15.8 cm^3K/mol). The χT product gradually increases as the temperature is lowered from 300 K to 3 K to reach a maximum of 47.2 cm^3K/mol (Figure 51). The increase in χT product is indicative of dominant ferromagnetic interaction within the Mn_6 unit. Two Mn(IV) ions each contribute a spin S = 3/2 and four Mn(III) ion contribute a spin, S = 2. The overall net spin ground state of the molecule is $S_T = 11$. The field dependence (up to 7 T) of the magnetization at different temperatures (1.8 to 8 K) has also been measured for **12**. The magnetization at 1.8 K saturates above 6.0 T at 20.7 μ_B (Figure 52) in good agreement with the $S_T = 11$ ground state. The clear saturation of the magnetization suggests the absence of a significant magnetic anisotropy and also the presence of a well defined spin ground state. In order to confirm the magnitude of spin ground state and the magnetic anisotropy, the magnetization, M vs. H/T data have been fitted to an $S_T = 11$ Brillouin function that leads to an excellent theory/ experiment agreement with a g factor of 2.12 and a D value of -0.116 cm^{-1} (Figure 53). Ac magnetic susceptibility measurements were conducted in order to determine whether **12** exhibits SMM property, however, no out-of-phase component χ'' was observed.

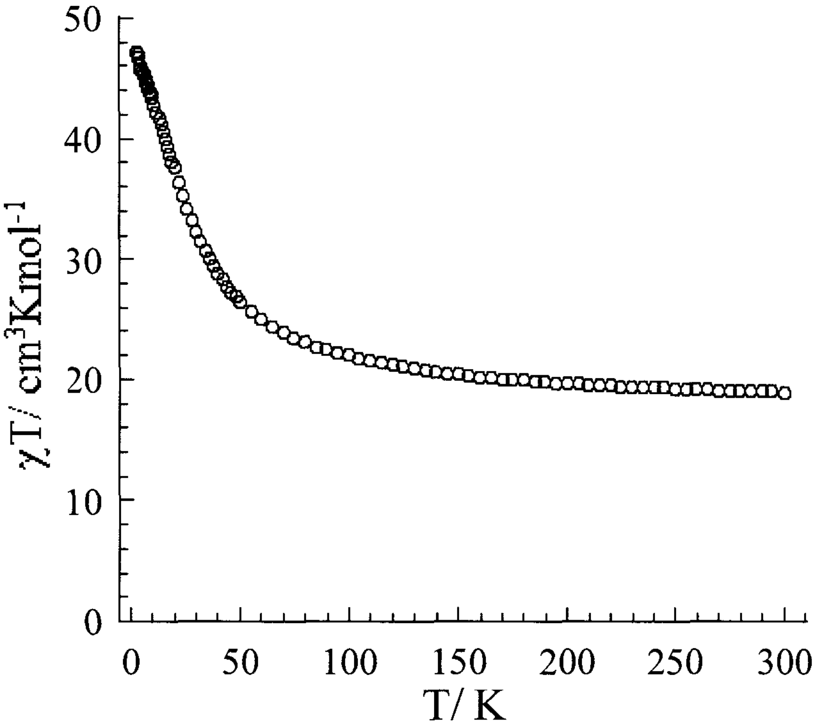

Figure 51. Plot of χT *vs.* T for complex **12** at 1000 Oe.

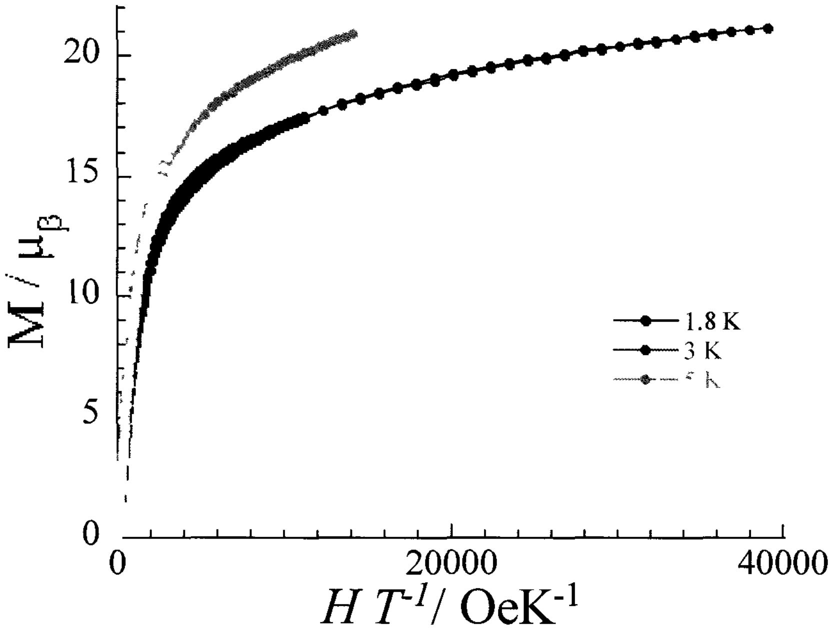

Figure 52. Reduced magnetization *vs.* field/ temperature for **12**.

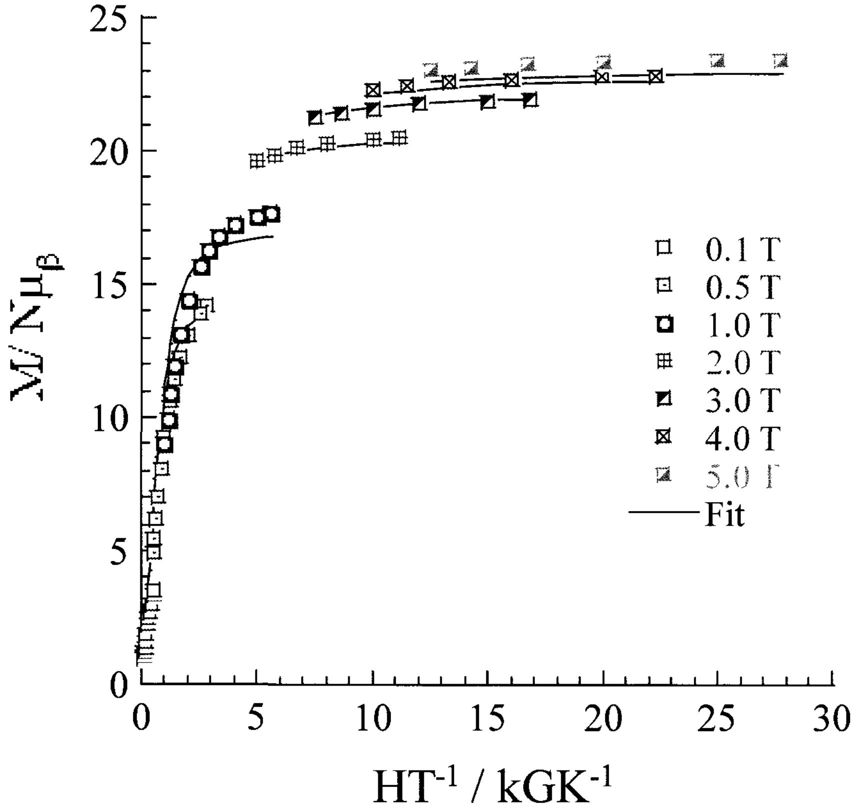

Figure 53. Plot of magnetization *vs.* field/ temperature along with the fit using the Brillouin function for an $S_T = 11$ (solid line).

4.3 Structure and Magnetism of [$Mn^{III}_4Mn^{IV}_2$(salox-Et)$_6$(μ_3-O)$_2$(μ_3-MeO)$_2$(μ-MeO)$_2$(DMF)$_2$]•MeOH, 13

The analogous complex **13**, [$Mn^{III}_4Mn^{IV}_2$(salox-Et)$_6$(μ_3-O)$_2$(μ_3-MeO)$_2$(μ-MeO)$_2$(DMF)$_2$]•MeOH, was characterized structurally and magnetically. This complex is similar to **12**, however, the two methanol molecules on Mn_6 are replaced by dimethyl formamide molecules (Figure 54). The unit cell contains only one repeating Mn_6 unit as opposed to two repeating Mn_6 units. The torsion angles along the Mn-O-N-Mn range from 7.7- 47.9° as shown in Table 11.

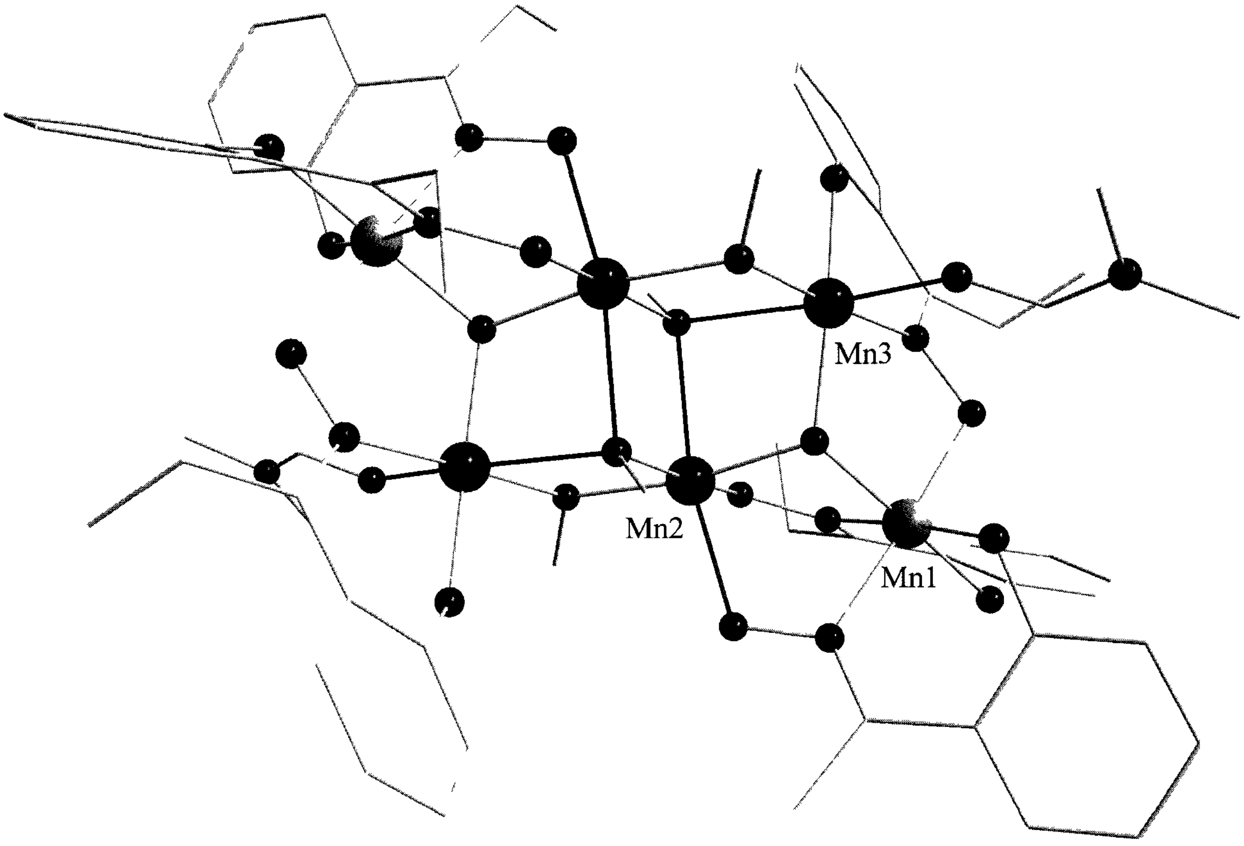

Figure 54. Molecular structure of $Mn^{III}_4Mn^{IV}_2$(salox-Et)$_6$(μ_3-O)$_2$(μ_3-MeO)$_2$(μ-MeO)$_2$(DMF)$_2$]•MeOH, **13**.

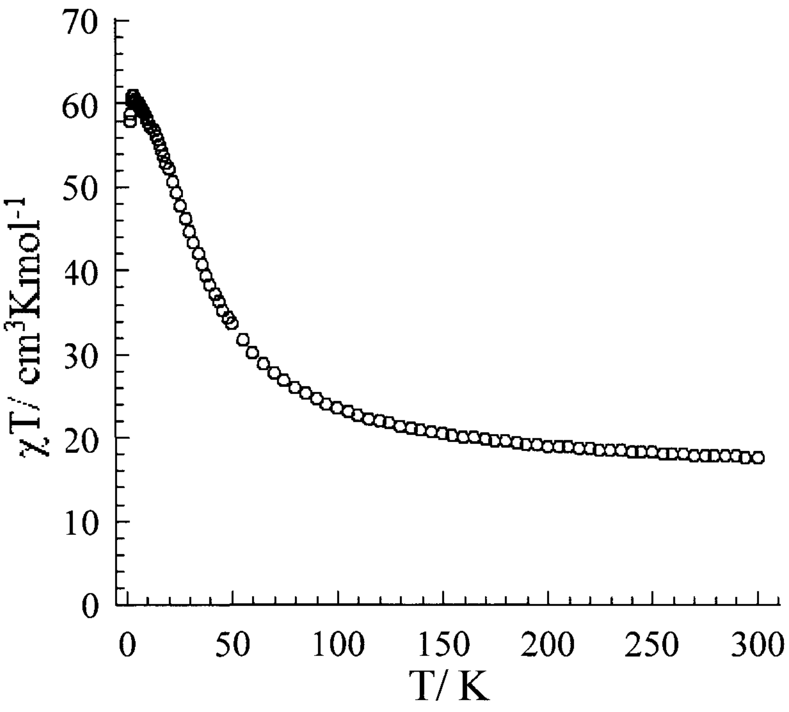

Figure 55. Plot of χT *vs.* T for complex **13** at 1000 Oe.

The χT product at 300 K is 17.6 cm^{3}K/mol which is closer to the theoretical value for a mixed valent Mn(III)$_4$/ Mn(IV)$_2$ species (15.8 cm^{3}K/mol). The χT product gradually increases as the temperature is lowered from 300 K to 3.5 K to reach a maximum of 61.1 cm^{3}K/mol (Figure 55). The increase in χT product is indicative of dominant ferromagnetic interaction within the Mn$_6$ unit. Two Mn(IV) ions each contribute a spin S = 3/2 and four Mn(III) ion contribute a spin, S = 2. The overall net spin ground state of the molecule is $S_T = 11$. Using the spin only formula for $S_T = 11$, χT product of 66.0 cm^{3}K/mol was obtained. Ac magnetic susceptibility measurements were conducted in order to determine whether **13** exhibits SMM property, however, no out-of-phase component χ'' was observed.

4.4 Discussion

Two ferromagnetic complexes have been characterized structurally and magnetically. Both share the defective dicubane motif exclusively linked through methoxides. The Mn-O-Mn angles forming the dicubane are similar as shown in Table 11. According to the bond valence sum calculations, the terminal Mn(1) ion is in the 4+ and 3+ oxidation state for **12** and **13**, respectively. However, taking into account the overall charge of the molecule, Mn(1) should be in 4+ oxidation state similar to **12**.

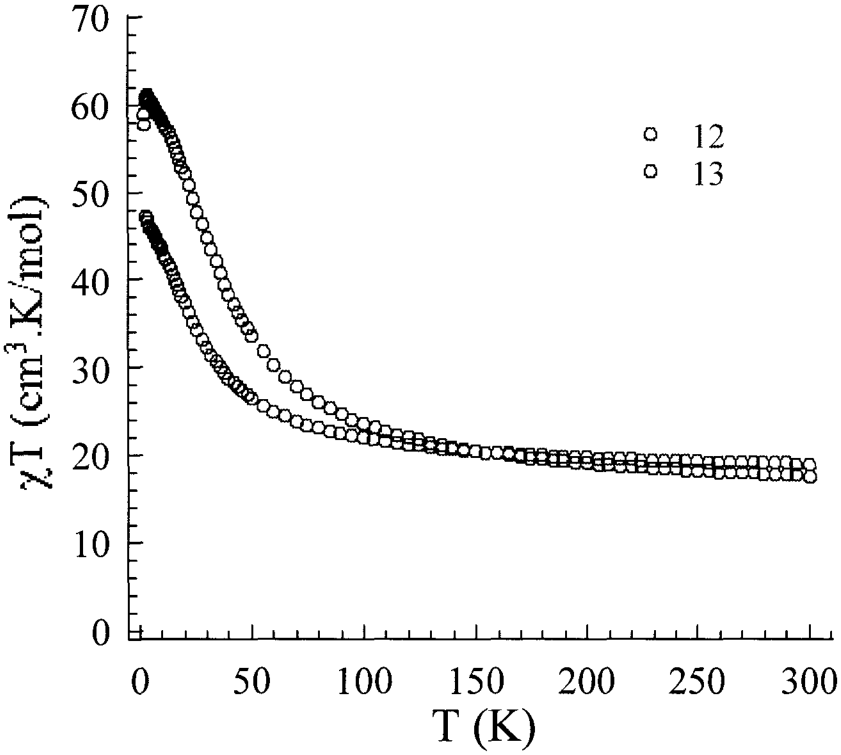

Figure 56. Comparison plot of χT *vs.* T for complex **12** and **13** at 1000 Oe.

Table 10. Bond valence sum calculation with the suggested oxidation states for **12** and **13**.

Complex	**12**				**13**			
	Mn(II)	Mn(III)	Mn(IV)	Ox. state	Mn(II)	Mn(III)	Mn(IV)	Ox. state
Mn(1)	4.13	3.89	4.02	4	3.34	3.12	3.17	3
Mn(2)	3.25	2.97	3.12	3	3.26	2.98	3.13	3
Mn(3)	2.90	2.69	2.76	3	3.22	2.98	3.07	3

The magnetic susceptibility χT product for **13** at low temperature is 61.1 cm^3K/mol. The theoretical value using the spin only formula is 66.0 cm^3K/mol for $S_T = 11$ ($Mn^{III}_4Mn^{IV}_2$)and 78.0 cm^3K/mol for $S_T = 12$ (Mn^{III}_6). This is a clear indication that the terminal Mn(1) ions are indeed in the 4+ oxidation state. In addition, there are no obvious Jahn-Teller elongation axes for Mn(1) as there is for Mn(2) and Mn(3) ions as shown in Table 11. The elongated axis (or the anistropic axis) for Mn(2) and Mn(3) is almost perdendicular resulting in a negligible anistropy to the system. Hence, **12** and **13** do not exhibit the SMM properties due to the absence of mangetic anistropy, which is one of the essential requirements. Comparison plot of χT *vs.* T shows both curves reaching a maxima, which is indicative of ferromagnetic interaction (Figure 56).

Table 11. Selected angles (°) and bond distances (Å) for **12** and **13**.

Parameters	**12**	**13**
Mn(1)-O(4)-N(3)-Mn(3) /°	40.47	46.93
Mn(1)-N(1)-O(11)-Mn(2) /°	12.15	7.71
Mn(1)-N(2)-O(12)-Mn(2) /°	24.48	21.60
Mn(2)-O(1)-Mn(3) /°	115.72	111.35
Mn(2)-O(8)-Mn(3) /°	89.07	87.90
Mn(2)-O(8)-Mn(2a) /°	97.31	97.94
Mn(2)-O(10)-Mn(3a) /°	107.37	107.18
Mn(2)-O(09)-Mn(3a) /°	96.40	97.00
Mn(1)-O(1) /Å	1.867	1.872
Mn(1)-O(2) /Å	1.865	1.868
Mn(1)-O(3) /Å	1.892	1.874
Mn(1)-O(4) /Å	1.906	1.939
Mn(1)-N(1) /Å	2.012	2.041
Mn(1)-N(2) /Å	1.956	2.017
Mn(2)-O(1) /Å	1.902	1.916
Mn(2)-O(08) /Å	2.329	2.274
Mn(2)-O(09) /Å	1.913	1.926
Mn(2)-O(10) /Å	1.921	1.938
Mn(2)-O(11) /Å	1.914	1.899
Mn(2)-O(12) /Å	2.120	2.122
Mn(3)-O(01) /Å	1.904	1.912
Mn(3)-O(05) /Å	2.242	2.174
Mn(3)-O(06) /Å	1.851	1.867
Mn(3)-O(07) /Å	1.956	1.987
Mn(3)-O(08) /Å	2.266	2.281
Mn(3)-N(3) /Å	2.004	2.174

Chapter 5

5.1 Mn_3 Triangles Linked by 1,2 Diols

One of the focal points of this research was to use the Mn_3 triangles, **4** - **11**, as precursors to generate larger nuclearity complexes. Is it possible to synthesize a molecule consisting of stacked Mn_3 triangles to produce Mn_6, Mn_9, or possibly one-dimensional polymers? This allows the Jahn-Teller axes to be aligned in one direction giving rise to large anisotropy. Each Mn(III) ion contains four unpaired electrons that contribute to the net spin ground state of the overall molecule. The most difficult aspect in engineering SMMs is to be able to synthetically control anisotropy and net spin ground state. In the quest to link the Mn_3 triangles through the axial positions, various linker molecules have been employed such as 4,4'-bipyridine, pyrazine, imidazole, 4,4'-dicarboxylic acids, 1,2- diol, and 1,3- diol (Figure 57). The reaction conditions were tuned to allow the incorporation of various linker molecules.

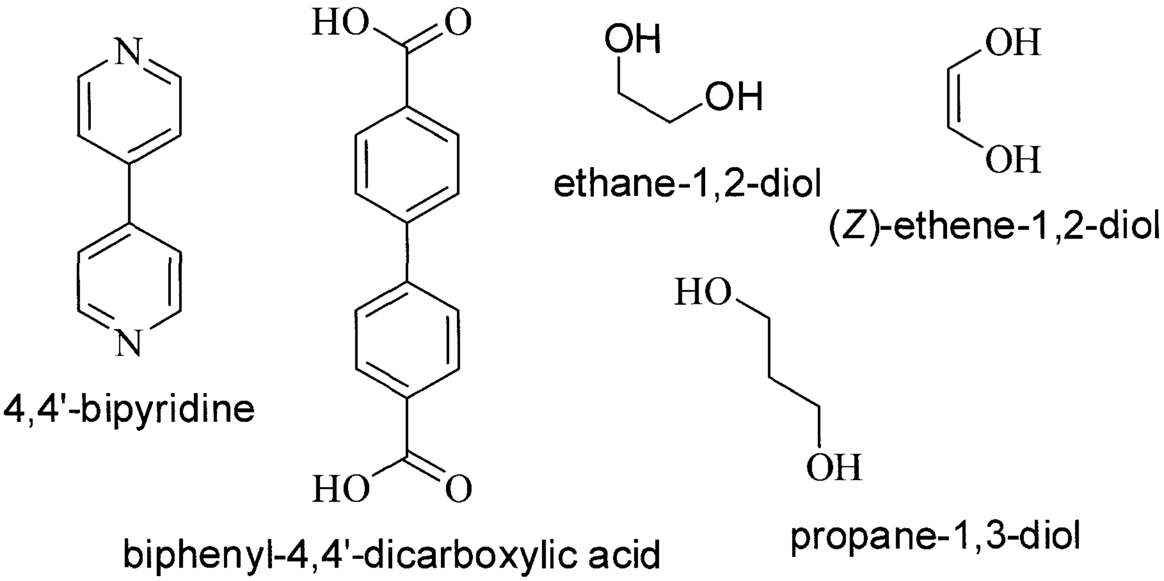

Figure 57. Bidentate organic linker molecules.

Eight Mn_3 triangles (**3 - 11**) were screened with the aforementioned linkers in an attempt to link the two triangles. However, only 1,2- diol was successfully employed to bridge two [Mn_3] core, more specifically **4** *via* the three axial positions (Figure 58). It is an ideal candidate to replace the three axial methanol molecules of **4**, allowing the two triangles to face each other in a near parallel fashion. In addition, the three diol molecules create an excellent pocket for a metal ion to occupy. This metal center essentially acts as a means of communication between the two triangles *via* the unpaired electrons. This structural motif resembles a dumb-bell with weights on either side. The terminal axial positions are available for further coordination. This is an ideal synthetic strategy to control the growth of metal aggregates which can potentially break the record energy barrier for manganese SMMs. The ultimate goal was to link two ferromagnetic triangles (i.e. complex **11**) *via* $[Mn^{IV}(diol)_3]^{2-}$ to produce an overall ferromangetic complex with an $S_T = 27/2$.

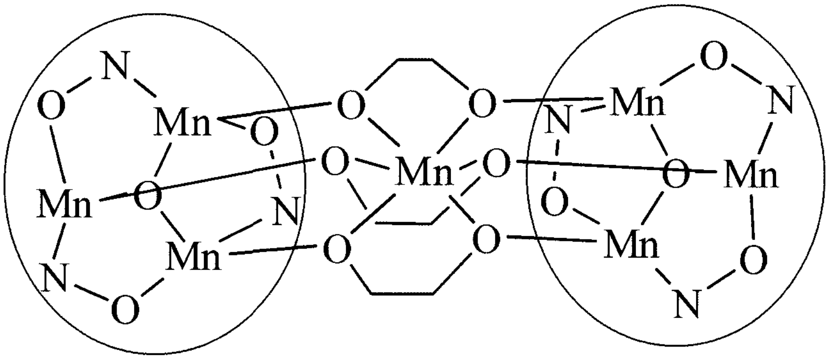

Figure 58. 1,2 diol acting as a bidentate ligand linking the two Mn_3 units.

Four Mn_7 complexes have been characterized structurally and magnetically. Complex **14**, $[Mn^{III}_6Mn^{IV}(\mu_3\text{-}O)_2(cpo)_6(diol)_3]$, is antiferromagnetically coupled to give an $S_T = 5/2$. In an attempt to alter the magnetic interaction, complexes **15** and **16** were synthesized with methanol and benzimidazole on the terminal axial positions, respectively. However, both compounds are magnetically similar. Complex **17**, $[Mn^{III}{}_6Mn^{IV}(\mu_3\text{-}O)_2(dpo)_6(diol)_3(MeOH)_2(H_2O)_2]\cdot4MeOH$, was synthesized using the more sterically hindered ligand (V), H_2dpo, as the equatorial ligand. In an attempt to form extended systems, the reaction conditions were tuned and complex **18**, $[Mn^{II}{}_2Mn^{III}{}_{18}(\mu_3\text{-}O)_6(cpo)_{18}Mn^{IV}{}_3(C_2H_4O_2)_{13}(MeCN)_4(H_2O)_6]^{2+}\cdot[(MeOH)(MeCN)(C_2H_6O_2)]$, was synthesized and characterized magnetically.

5.2 Structure and Magnetism of $[Mn^{III}{}_6Mn^{IV}(\mu_3\text{-}O)_2(cpo)_6(diol)_3]$, 14

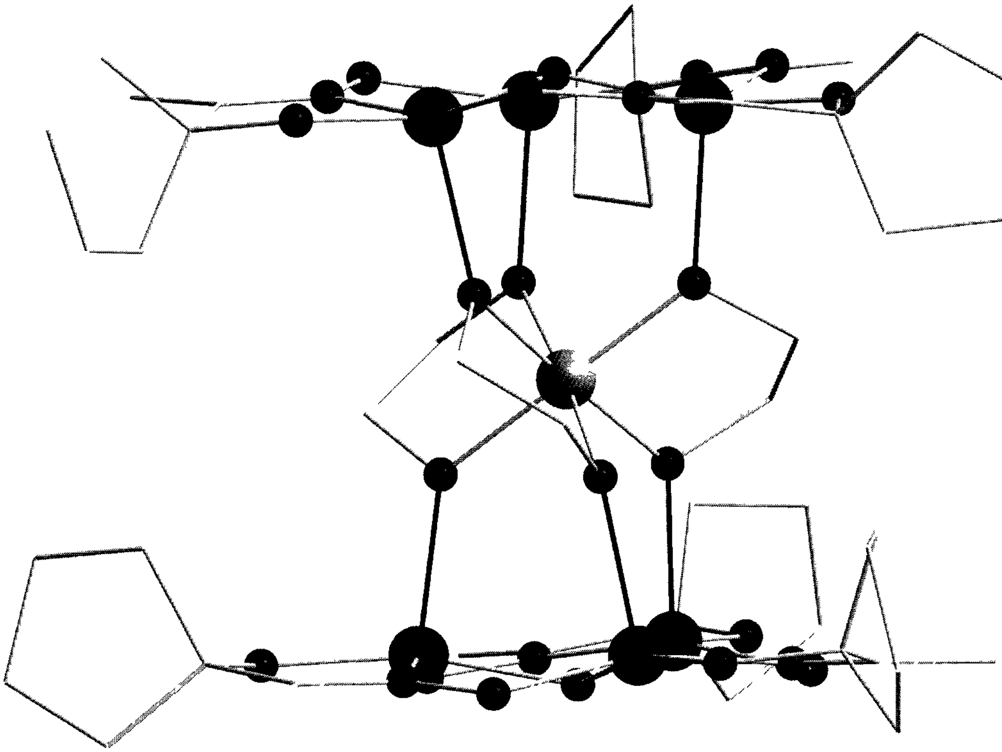

Figure 59. Molecular structure of $[Mn^{III}{}_6Mn^{IV}(\mu_3\text{-}O)_2(cpo)_6(diol)_3]$, **14**.

Complex **14**, $[Mn^{III}{}_6Mn^{IV}(\mu_3\text{-}O)_2(cpo)_6(diol)_3]$, was synthesized using **4** as a building block in solution with 1,2 diol as a linking agent (Figure 59). The two equilateral $Mn(III)_3$ triangles are coupled together by a Mn(IV) unit. The $Mn(III)_3$ triangle unit is encapsulated by three cpo^{2-} ligands and connected by a central μ_3- oxygen. The three bidentate 1,2 diol ligands coordinate to the axial positions of the two triangles forming the sandwich-like complex. In addition, it forms an ideal octahedral pocket for the Mn(IV) ion to occupy (Figure 60). The two Mn_3 planes are parallel with a separation distance of 6.338 Å. All six Mn(III) ions are penta-coordinate with the axial bonds elongated as a result of Jahn-Teller effect. The torsion angle formed along the Mn(2)-N(1)-O(1)-Mn(2) atoms is 10.9°.

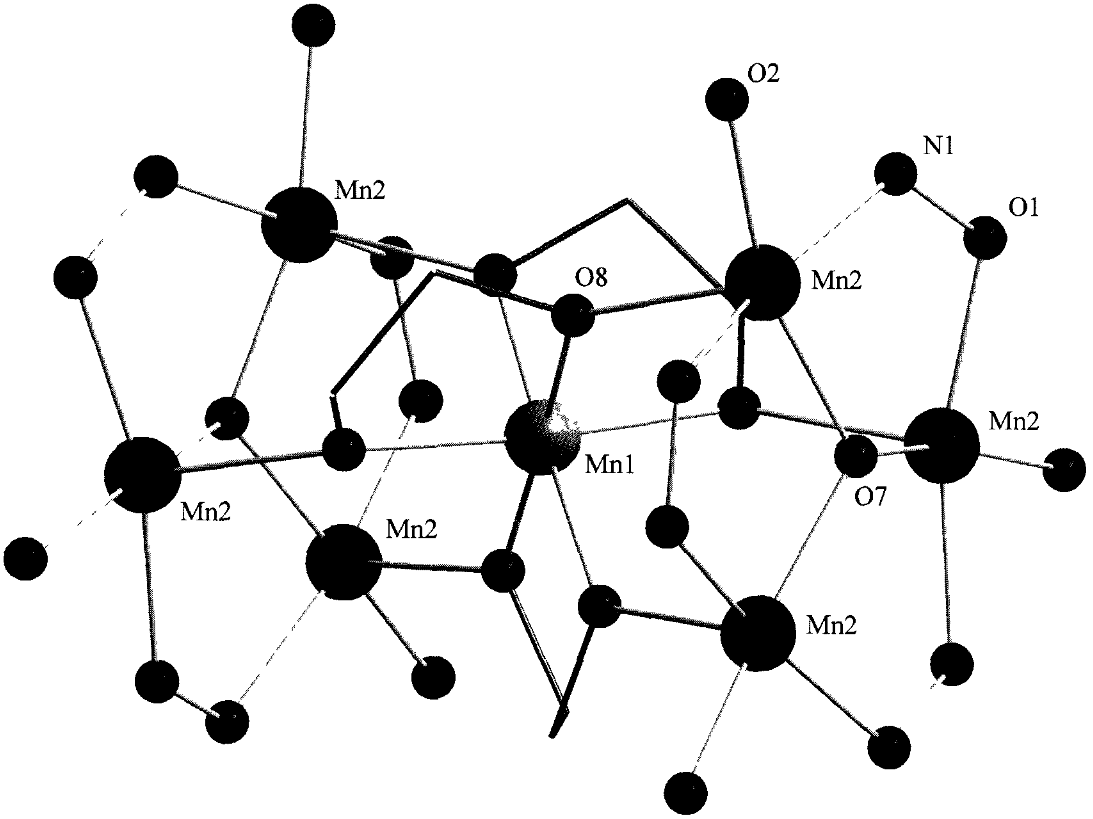

Figure 60. Core structure of **14** with 1,2 diol ligand shown in turquoise bonds connecting the two triangles.

At room temperature, the χT product is 16.5 cm^3K/mol (Figure 61) which is slightly lower in comparison to the expected value of 19.88 cm^3K/mol for six non-interacting Mn(III) ions (g = 2.00; C = 3.00 cm^3K/mol) and one Mn(IV) ions (g = 2.00; C = 1.875 cm^3K/mol). This is the result of the intra-molecular antiferromagnetic interaction in the [Mn_7] core as shown by the decrease of the χT product when lowering the temperature down to 1.81 K where it reaches a value of 0.77 cm^3K/mol at 1000 Oe. The obtained value of the χT product at 1.8 K is significantly lower than the expected value of an S = 5/2 state resulting from the complete antiferromagnetic arrangement of the spins in the [Mn_7] core. This result suggests that significant magnetic interactions are present between Mn(III) and even between Mn(III) and Mn(IV) (if the Mn(III)-Mn(IV) were negligible a χT product of 7.875 cm^3K/mol would be expected). There is also a relatively strong antiferromagnetic interaction between the [Mn_7] units. Based on the molecular structure of the [Mn_7] core, numerical models have been used to reproduce the magnetic data. Unfortunately neither isotropic (considering only one Mn(III)-Mn(III) and one Mn(III)-Mn(IV) interactions) nor anisotropic (considering only one Mn(III)-Mn(III), one Mn(III)-Mn(IV) interactions and a zero-field splitting parameters on the Mn(III) ions) Heisenberg models were able to reproduce in a satisfactory manner to the experimental data. Therefore, the complex was simplified to a simple sum of susceptibility from two Mn(III) S = 2 regular triangles (using an isotropic Heisenberg model considering the following Hamiltonian: $H = -2J(S_1 \bullet S_2 + S_1 \bullet S_3 + S_2 \bullet S_3)$ and a Curie Mn(IV) S = 3/2 contribution. In this approximation, the data have been fitted only above 50 K in order to avoid the effects of the smaller Mn(III)-Mn(IV) interactions, inter-complex magnetic interactions and magnetic anisotropy. As shown below, the experimental data have been fitted well and the best set of parameters found is J/k_B = -8.3(1) K and g = 2.01(5) as expected for Mn(III) sites (red line in the Figure below). The obtained Mn(III)-Mn(III) interaction value is quite similar to the one found for the isolated [Mn_3] units and related [Mn_7] complexes previously measured.

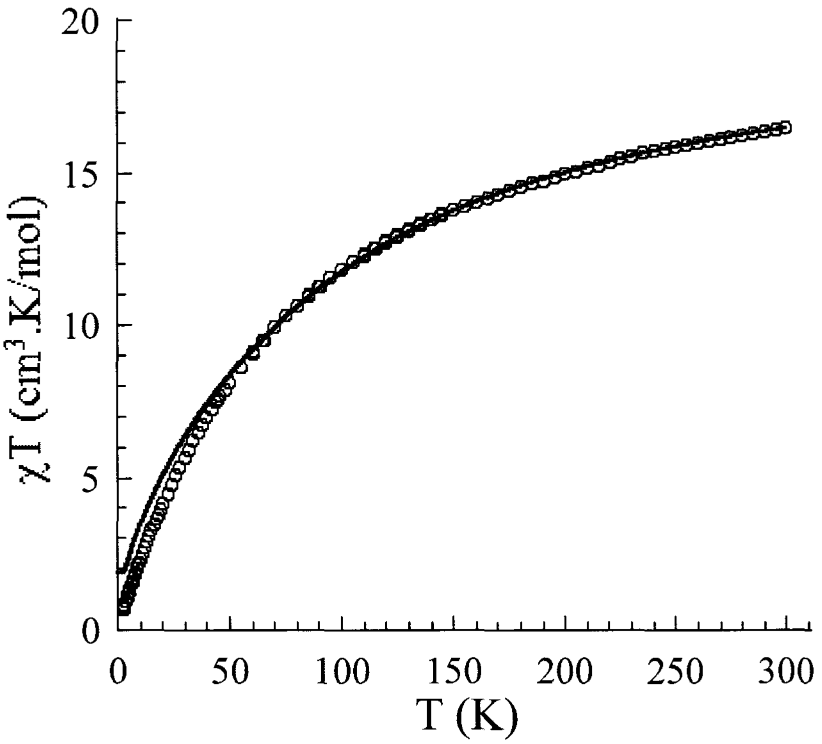

Figure 61. Plot of χT *vs.* T for complex **14** at 1000 Oe. The solid line is the best fit obtained with the Heisenberg trinuclear model.

Field dependence of the magnetization measurement was done under dc applied fields ranging from 0 T to 7 T and at temperatures of 1.8, 3, 5 and 8 K (Figure 62). The magnetization increases continuously and almost linearly up to the maximum value of 3.2 μ_β at 1.8 K and 7 T. The data shows no clear sign of saturation which is indicative of (i) a strong magnetic anisotropy and/or (ii) most likely the presence of low lying excited states probably present due the weak Mn(IV)-Mn(III) magnetic interactions and/or (iii) even more likely due to the presence of intermolecular antiferromagnetic interactions.

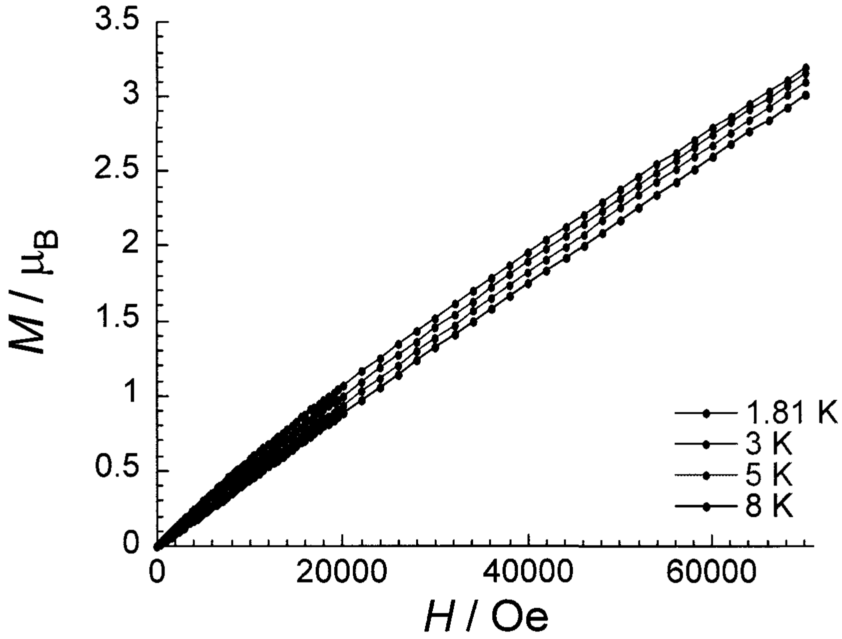

Figure 62. Reduced magnetization *vs.* field for complex **14.**

5.3 Structure and Magnetism of $[Mn^{III}_6Mn^{IV}(\mu_3\text{-}O)_2(cpo)_6(diol)_3(MeOH)_2(H_2O)_2]$, 15

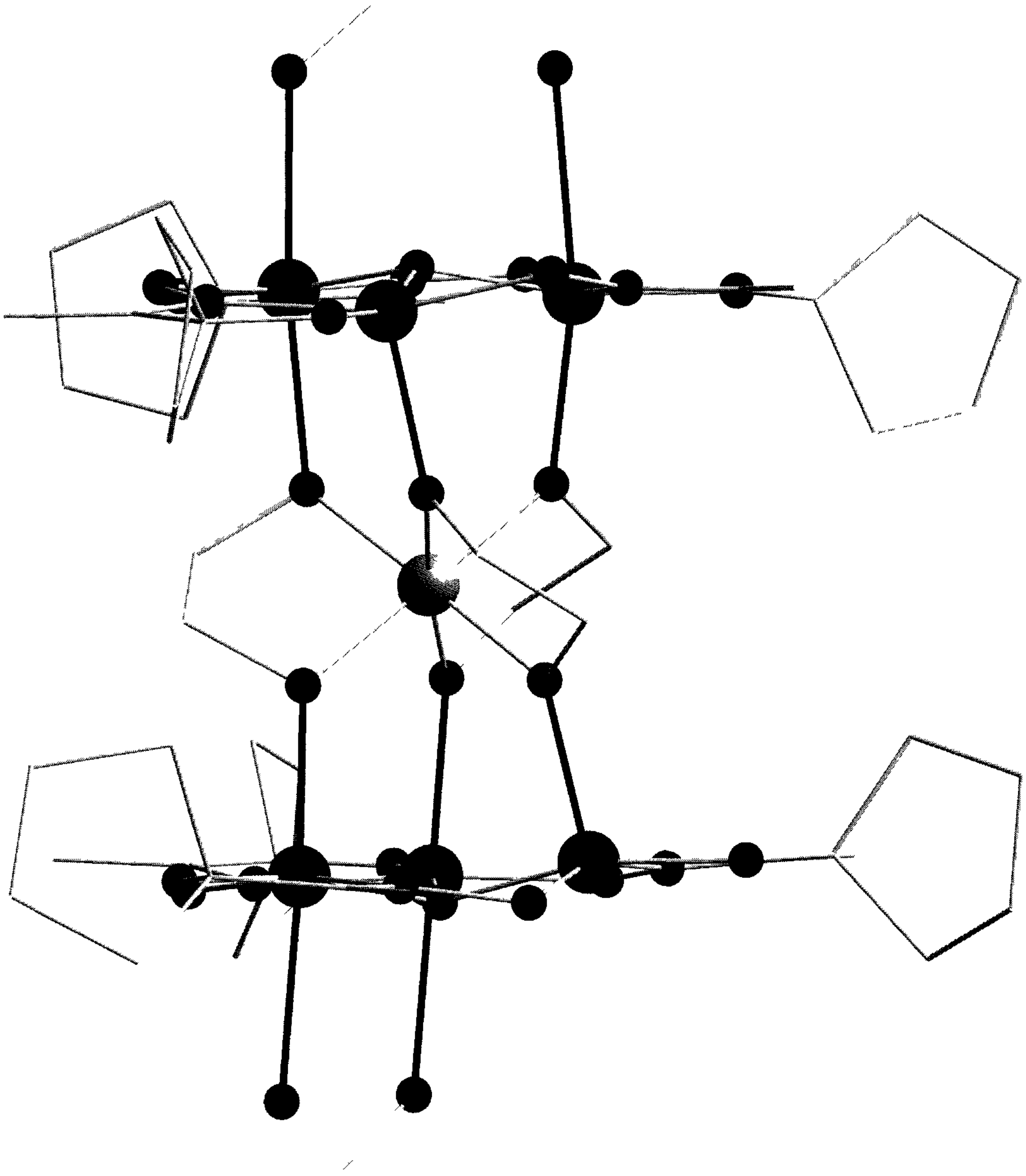

Figure 63. Molecular structure of $[Mn^{III}_6Mn^{IV}(\mu_3\text{-}O)_2(cpo)_6(diol)_3(MeOH)_2(H_2O)_2]$, **15**.

Complex **15**, $[Mn^{III}_6Mn^{IV}(\mu_3\text{-}O)_2(cpo)_6(diol)_3(MeOH)_2(H_2O)_2]$, consists of two non-equilateral $Mn(III)_3$ triangles stacked in-near planar fashion (Figure 63). These two triangles are bridged by three 1,2 diol molecules in which one Mn(IV) ion is trapped in an octahedral coordination environment with Mn-O distances 1.86 - 1.91 Å. On either end of the terminal Mn ions (Mn8 and Mn7) two MeOH and two H_2O molecules are coordinated to complete the octahedral geometry (Figure 64).

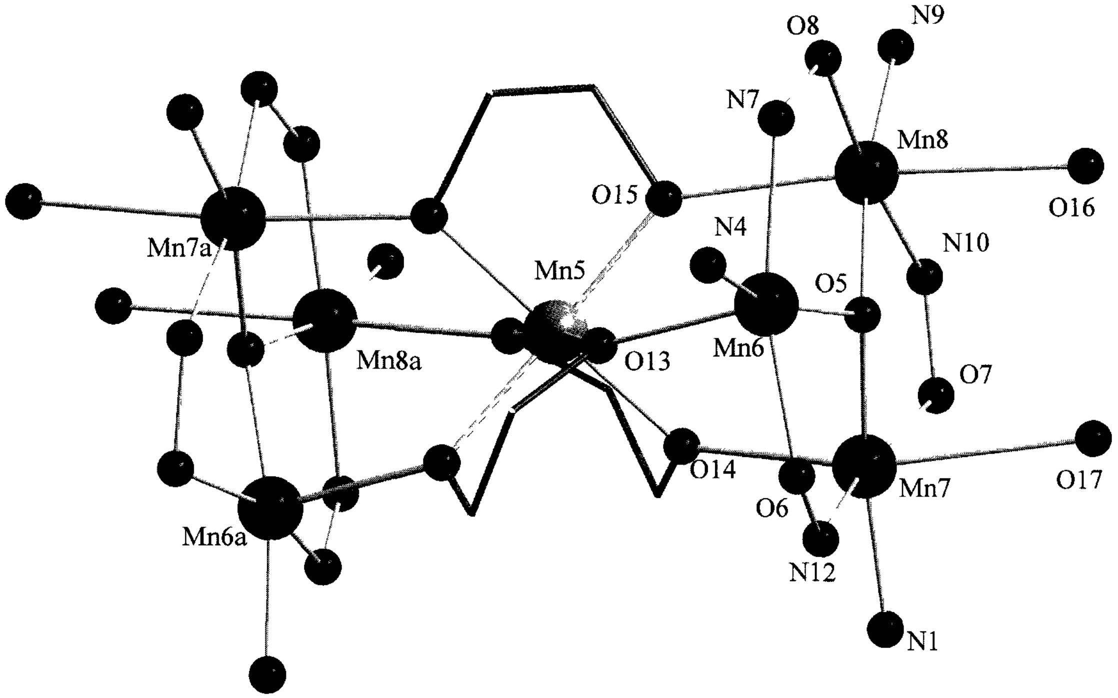

Figure 64. Core structure of **15** with 1,2 diol ligand shown in cyan bonds connecting the two triangles.

At room temperature, the χT product is 17.35 cm^3K/mol (Figure 65) which is slightly lower in comparison to the expected value of 19.87 cm^3K/mol for six non-interacting Mn(III) ions (g = 2.00; C = 3.00 cm^3K/mol) and one Mn(IV) ions (g = 2.00; C = 1.875 cm^3K/mol). This slightly low value is the result of the intra-molecular antiferromagnetic interaction in the [Mn_7] core as shown by the decrease of the χT product when lowering the temperature down to 1.81 K where it reaches a value of 1.5 cm^3K/mol at 1000 Oe. The obtained value of the χT product at 1.8 K is significantly lower than the expected value of an S = 5/2 state resulting from the complete antiferromagnetic arrangement of the spins in the [Mn_7] core. As shown below, the experimental data have been fitted well and the best set of parameters found is J/k_B = -6.3(1) K and g = 2.01(5) as expected for Mn(III) sites (red line in the Figure below). The obtained Mn(III)-Mn(III) interaction value is quite similar to the one found for the isolated [Mn_3] units previously measured.

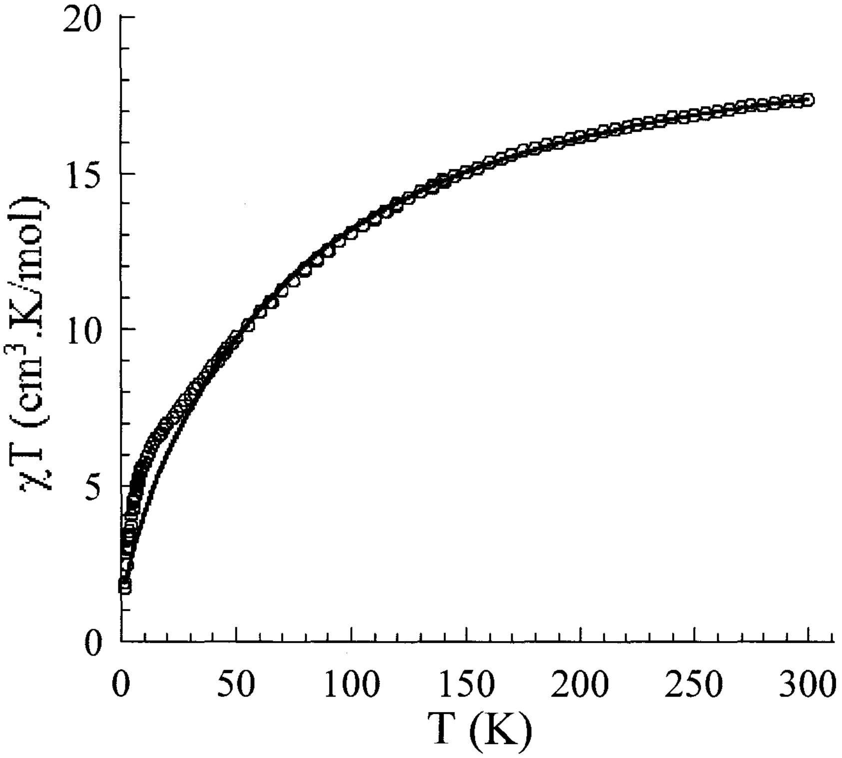

Figure 65. Plot of χT *vs.* T for complex **15** at 1000 Oe. The solid line is the best fit obtained with the Heisenberg trinuclear model.

5.4 Structure and Magnetism of $[Mn^{III}_6Mn^{IV}(\mu_3\text{-}O)_2(cpo)_6(diol)_3(benzIm)_2]\cdot4MeCN$, 16

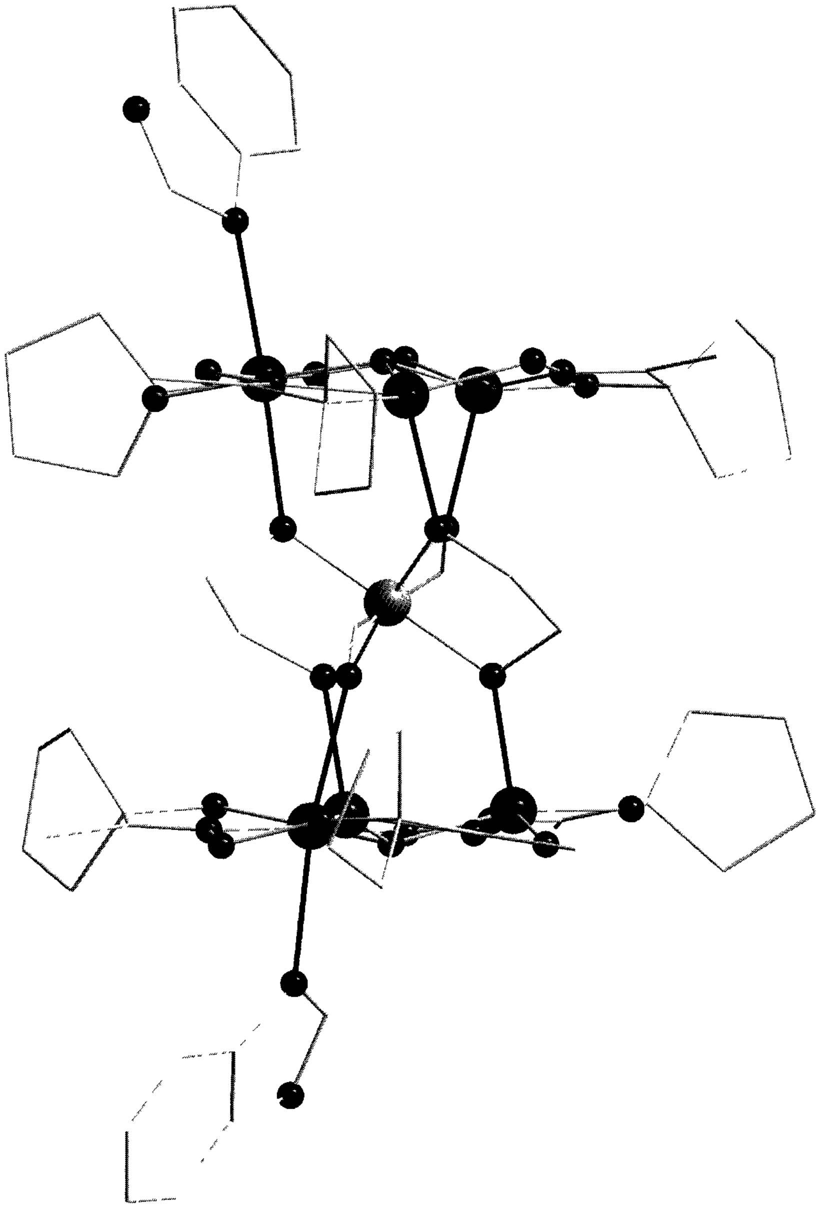

Figure 66. Molecular structure of $[Mn^{III}_6Mn^{IV}(\mu_3\text{-}O)_2(cpo)_6(diol)_3(benzIm)_2]\cdot4MeCN$, **16**.

Complex **16**, $[Mn^{III}_6Mn^{IV}(\mu_3\text{-}O)_2(cpo)_6(diol)_3(benzIm)_2]$•4MeCN, consists of two non-equilateral triangles linked by three 1,2 diol molecules, analogous to **15**. However, on the terminal ends of the $[Mn_7]$ core, two benzimidazole molecules are coordinated on the Mn(III) ions (Figure 66).

At room temperature, the χT product is 18.2 cm^3K/mol (Figure 67) which is slightly lower in comparison to the expected value of 19.87 cm^3K/mol for six non-interacting Mn(III) ions (g = 2.00; C = 3.00 cm^3K/mol) and one Mn(IV) ions (g = 2.00; C = 1.875 cm^3K/mol). This slightly low value is the result of the intra-molecular antiferromagnetic interaction in the $[Mn_7]$ core as shown by the decrease of the χT product when lowering the temperature down to 1.81 K where it reaches a value of 5.2 $cm^3K/$ mol at 1000 Oe. The pseudo-saturation of the χT product below 4 K seems to indicate a ground state that is solely populated at 1.8 K. The obtained value of the χT product at 1.8 K might be compatible with an expected $S = 5/2$ state resulting from the complete antiferromagnetic arrangement of the spins in the $[Mn_7]$ core. This result suggests that significant magnetic interactions are present between Mn(III) and even between Mn(III) and Mn(IV) (if the Mn(III)-Mn(IV) were negligible a χT product of 7.875 cm^3K/mol would be expected). As shown below, the experimental data have been fitted remarkably well and the best set of parameters found is J/k_B = -4.9(1) K and g = 2.00(5) as expected for Mn(III) sites (red line in the Figure below). The obtained Mn(III)-Mn(III) interaction value is quite similar to the one found for the isolated $[Mn_3]$ units previously measured.

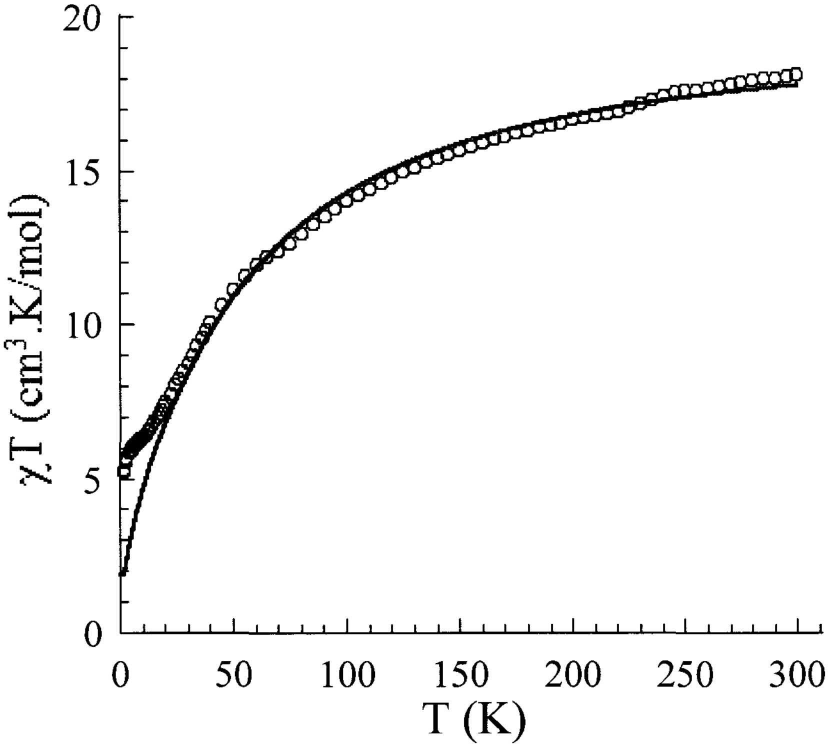

Figure 67. Plot of χT *vs.* T for complex **16** at 1000 Oe. The solid line is the best fit obtained with the Heisenberg trinuclear model.

5.5 Structure and Magnetism of $[Mn^{III}_6Mn^{IV}(\mu_3\text{-}O)_2(dpo)_6(diol)_3(MeOH)_2]\bullet 4MeOH$, 17

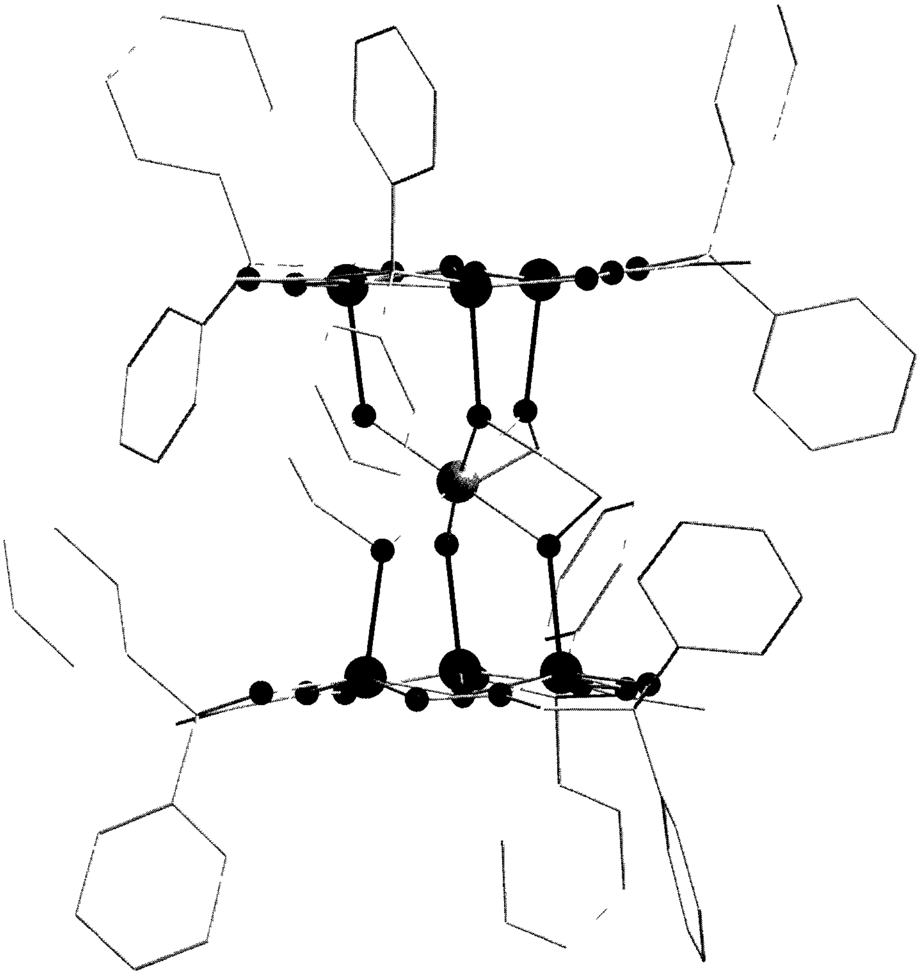

Figure 68. Molecular structure of $[Mn^{III}_6Mn^{IV}(\mu_3\text{-}O)_2(dpo)_6(diol)_3(MeOH)_2]\bullet 4MeOH$, **17**.

Complex **17**, $[Mn^{III}_6Mn^{IV}(\mu_3\text{-}O)_2(dpo)_6(diol)_3(MeOH)_2]\bullet 4MeOH$, was synthesized using H_2dpo as the equatorial ligand (Figure 68). The two sets of $[Mn_3]$ triangles are linked by three 1,2 diols which contain a Mn(IV) ion in the center. These two sets of $[Mn_3]$ are parallel to each other. The torsion angles along the Mn-N-O-Mn bond is between 2.8 - 4.0°. All six Mn(III) ions are penta-coordinate with the axial bonds elongated due to the Jahn-Teller effect.

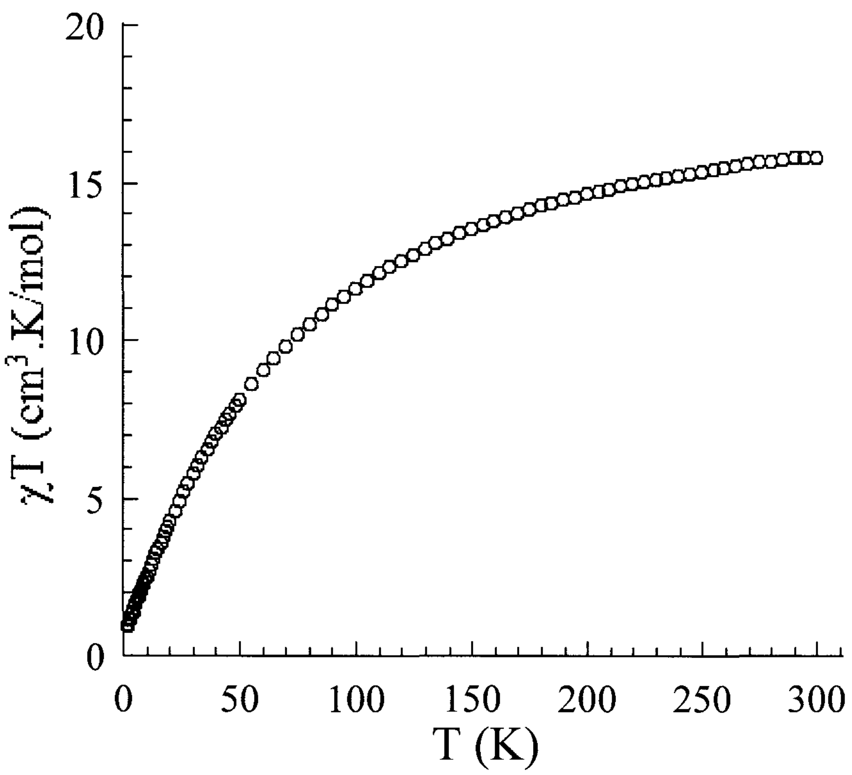

Figure 69. Plot of χT *vs.* T for complex **17** at 1000 Oe.

At room temperature, the χT product is 15.8 cm^3K/mol (Figure 69) which is low in comparison to the expected value of 19.87 cm^3K/mol for six non-interacting Mn(III) ions ($g = 2.00$; $C = 3.00$ $cm^3K/$ mol) and one Mn(IV) ions ($g = 2.00$; $C = 1.875$ cm^3K/mol). This is due to the strong intra-molecular antiferromagnetic interaction within the [Mn_7] core. This is evident as the temperature is decreased to 1.8 K, the χT product reaches a value of 0.95 cm^3K/mol at 1000 Oe.

5.6 Structure and Magnetism of $[Mn^{II}_2Mn^{III}_{18}(\mu_3\text{-}O)_6(cpo)_{18}Mn^{IV}_3(C_2H_4O_2)_{13}(MeCN)_4(H_2O)_6]^{2+}$ •$[(MeOH)(MeCN)(C_2H_6O_2)]$, 18

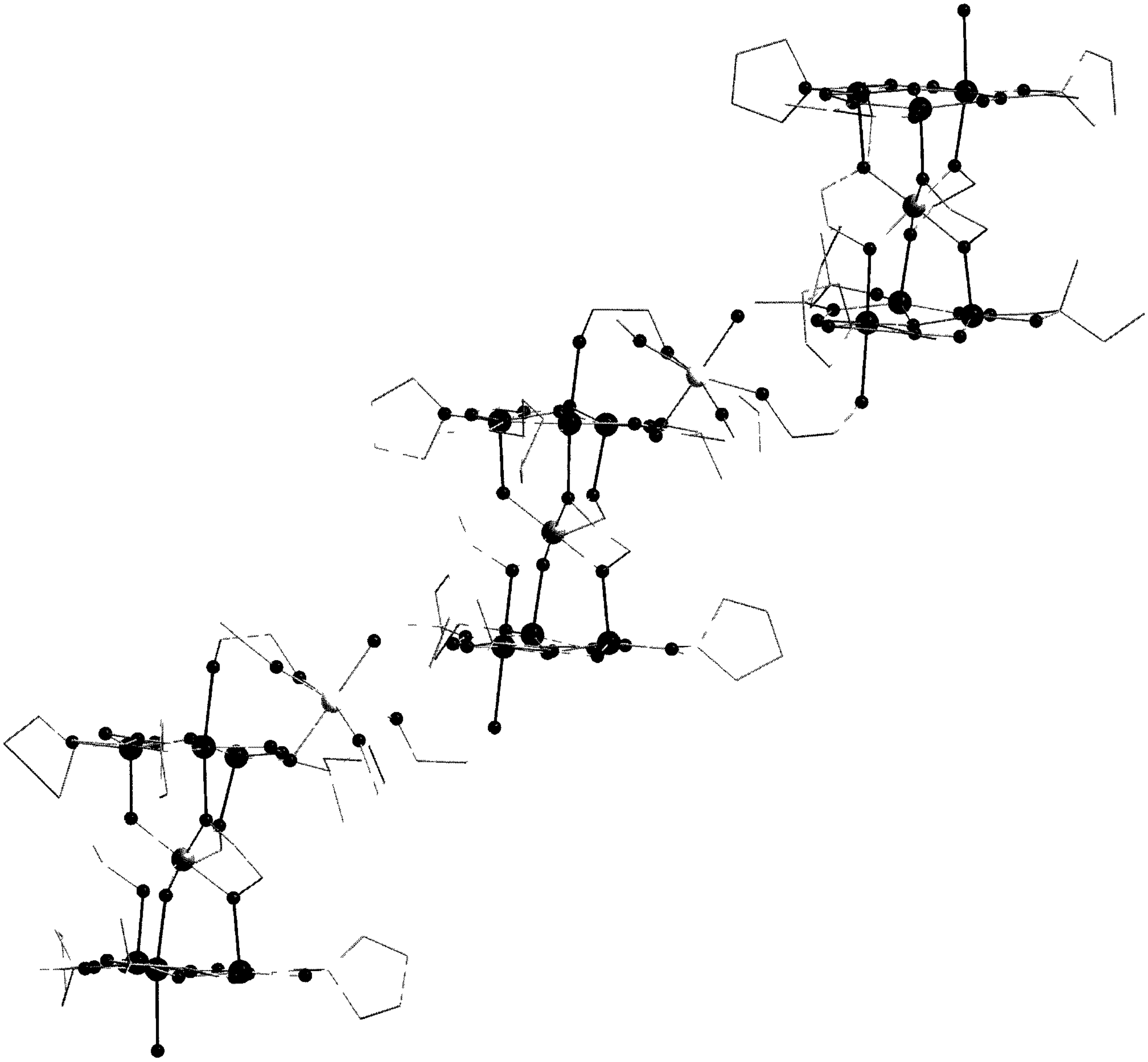

Figure 70. Molecular structure of $[Mn^{II}_2Mn^{III}_{18}(\mu_3\text{-}O)_6(cpo)_{18}Mn^{IV}_3(C_2H_4O_2)_{13}(MeCN)_4(H_2O)_6]^{2+}$•$[(MeOH)(MeCN)(C_2H_6O_2)]$, **18**.

Complex **18** is a large metal cluster containing 23 Mn ions with oxidation states ranging from 2+ to 4+. It consists of three repeating [Mn_7] units linked by two monomeric Mn(II) ions and capped by two water molecules (Figure 70). All three [Mn_7] units are oriented in parallel fashion with the Jahn-Teller axes aligned in one direction. The Mn(II) ion is coordinated to two MeCN, two H_2O and two 1,2 diol molecules. The latter acts a bridging unit to link the [Mn_7] units. All of the oxidation states are confirmed by charge balance and bond valence sum calculations. This Mn_{23} cluster crystallizes out with two perchlorate anions, one MeOH, one MeCN and one 1,2 diol molecule.

At room temperature, the χT value is 53.1 cm^3K/mol (figure 71) that is low in comparison with the expected value (68.375 cm^3K/mol) for three $S = 3/2$ Mn(IV) metal ions ($C = 1.875$ cm^3K/mol), 18 $S = 2$ Mn(III) metal ions ($C = 3$ cm^3K/mol) and two $S = 5/2$ Mn(II) metal ions ($C = 4.375$ cm^3K/mol). This result is explained by the presence of strong intramolecular antiferromagnetic interactions that are seen on the temperature dependence of the χT product. Indeed, the χT product decreases all the way down to 1.8 K to reach 17.6 cm^3K/mol. This decrease is not monotonous as expected in presence of a variety of magnetic interactions. Fit of the experimental data to a Curie-Weiss law above 50 K leads to a Curie constant of 61.6 cm^3K/mol that is closer to the expected value given above. The Weiss constant is on the other hand equal to -46.7 K in agreement with strong antiferromagnetic interactions. It is difficult to further analyze the data as this complex with 23 magnetic centers is too large. The only possibility is that the [Mn_7] units have an $S = 5/2$ ground state at this temperature resulting from four $S = 2$ spins down in opposition to two $S = 2$ and one $S = 3/2$ spins down (each Mn(III) triangle are antiferromagnetically coupled). Then at about 10 K, we should have five $S = 5/2$

spins taking into account the two Mn(II) spins that are in very weak interactions and thus a χT product close to 5 times 4.375 cm^3K/mol equal to 21.875 cm^3K/mol as seen experimentally.

The field dependence of the magnetization below 8 K reveals a relative slow increase of the magnetization at low fields that is not saturating even at 7 T and 1.8 K reaching 27.6 μ_B. The field dependence of the magnetization suggests the presence of a significant magnetic anisotropy and/or low lying exited states in agreement with the weak intramolecular magnetic interactions mentioned above. This is confirmed by plotting the *M vs. H/T* at different fields, the curves are not superposed on a single master-curve further indicating that these effects (magnetic anisotropy and/or low lying exited states) are significant. In addition, it is worth noting that no hysteresis on the *M vs. H* data has been observed above 1.8 K with sweep-rate used in a traditional SQUID magnetometer (100 – 200 Oe/min) and that no out-of-phase ac susceptibility has been detected above 1.8 K.

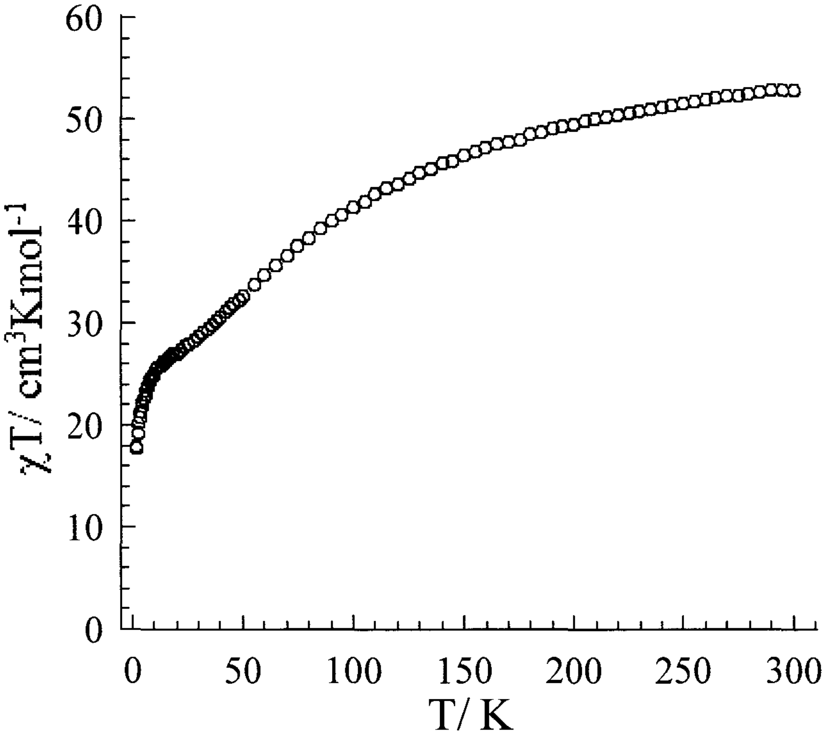

Figure 71. Plot of χT *vs.* T for complex **18** at 1000 Oe.

5.7 Discussion

Five complexes containing the $[Mn_7]$ have been characterized structurally and magnetically. All five complexes, **14-18**, possess the basic fundamental repeating $[Mn_3]$ units which are antifferromangetically coupled. Efforts to synthesize the Mn_7 unit containing the ferromagnetic Mn_3 units have been unsuccessful. Theoretically, this approach would lead to a molecule with large spin ground state, given the Mn_3 is ferromagnetically coupled to the other Mn_3 *via* Mn(IV) ion. The anisotropic axis is deliberately aligned in one direction to maximize the magnitude and hence possibly break the record barrier with an $S_T = 27/2$ (Figure 72).

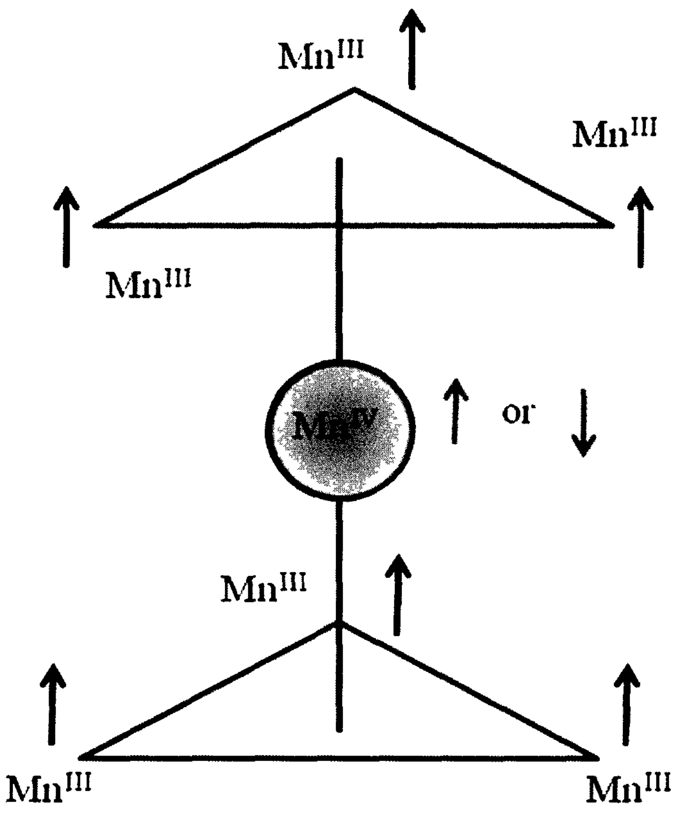

Figure 72. Hypothetical case with ferromagnetic triangles linked through a Mn(IV) ion to yield $S_T = 27/2$ or $S_T = 21/2$.

In order to confirm the oxidation states of each Mn ion in the complex, bond valence sum calculations were performed and tabulated in Table 11. According to the magnetic measurements, all five complexes exhibit dominant antiferromagnetic interactions within the [Mn_7] core shown in Figure 73. The magnetic parameters obtained using the fit is shown in Table 12 using the isotropic Heisenberg model. All five compounds clearly demonstrate a dominant antiferromagnetic interaction between the metal centers.

Table 11. Bond valence sum calculations with the suggested oxidation states for **14** - **18**.

		Central Mn ion	1st set of Mn_3 Triangle			Monomer
Complex		Mn(1)	Mn(2)	Mn(3)	Mn(4)	Mn(5)
14	Mn(II)	4.19	3.25			
	Mn(III)	3.83	3.01			
	Mn(IV)	4.02	3.10			
Ox. State		4	3			
15	Mn(II)	4.30	3.27	3.19	2.58	
	Mn(III)	3.93	3.03	2.95	2.36	
	Mn(IV)	4.13	3.12	3.04	2.48	
Ox. State		4	3	3	3	
16	Mn(II)	4.17	3.25	3.21	3.43	
	Mn(III)	3.81	3.00	2.97	3.24	
	Mn(IV)	4.00	3.10	3.06	3.24	
Ox. State		4	3	3	3	
17	Mn(II)	3.96	3.31			
	Mn(III)	3.62	3.06			
	Mn(IV)	3.80	3.15			
Ox. State		4	3			
18	Mn(II)	4.19	3.42	3.39	3.65	1.95
	Mn(III)	3.83	3.22	3.18	3.44	1.84
	Mn(IV)	4.03	3.23	3.20	3.44	1.84
Ox. State		4	3	3	3	2

Table 12. Magnetic fit parameters for complexes **14** - **18**.

Complex	J (K)	g	χT*	S_T
14	-8.3(1)	2.01(5)	16.5	0-5/2
15	-6.3(1)	2.01(5)	17.4	0-5/2
16	-4.9(1)	2.00(5)	18.2	0-5/2
17	N/A	N/A	15.8	0-5/2
18	N/A	N/A	53.1	N/A

* cm^3K/ mol at 300 K

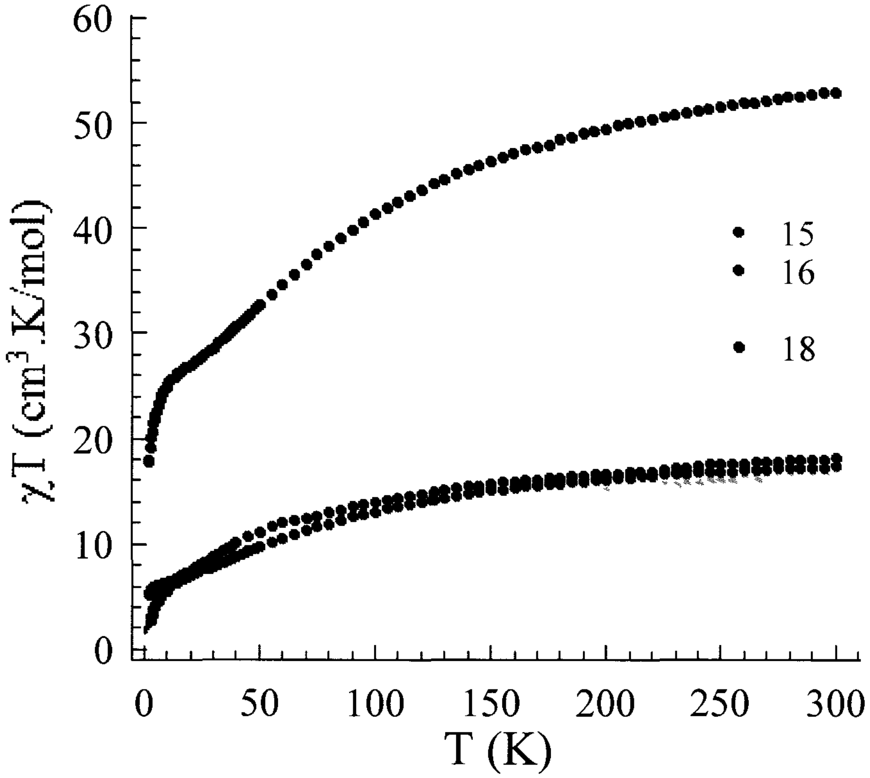

Figure 73. Comparison plot of χT *vs.* T for complexes **14** - **18** at 1000 Oe.

Chapter 6

6.1 Stacked Mn_3 Triangles Leading to Larger Clusters

A novel synthetic strategy was developed to target high nuclearity manganese clusters based on trinuclear ferromagnetic units. In order to promote the ferromagnetic interaction in the Mn_3 units, class B ligand VIII, H_2salox-Me, was employed. The latter ligand is known to yield perchlorate capped ferromagnetic triangle **11** with SMM behaviour as shown in chapter 3. Therefore, in order to prevent the capping of ClO_4 and promote larger cluster formation, $Mn(CH_3COO)_2$ was used as a starting material in the reaction conditions. Acetate anions act as excellent bridging ligands and promote the formation of larger cluster molecules as observed in the Mn_{12} complex. This chapter focuses on using Mn_3 triangles which are stacked to produce larger clusters (figure 74).

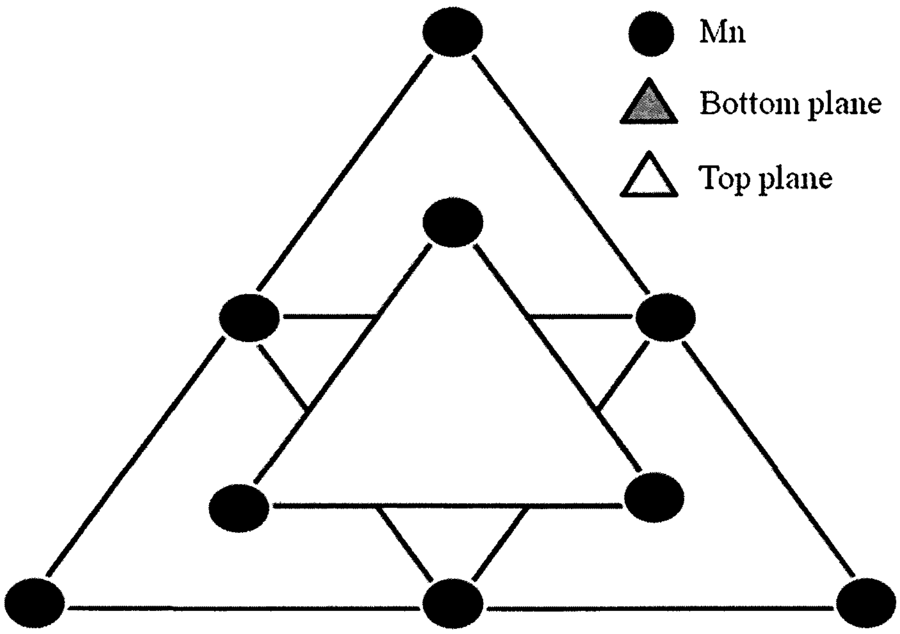

Figure 74. Mn triangles stacked in two planes to form Mn_9 aggregates.

Two enneanuclear [Mn_9] clusters containing the ferromagnetic trinuclear SMM unit have been characterized based on the structure and magnetic properties. Both complexes contain salox-Me^{2-} ligands on the equatorial positions with the triangles oriented as shown in Figure 74. Even larger Mn aggregates were isolated by tuning the reaction conditions and switching the equatorial ligand to salox-Et^{2-}.

6.2 Structure and Magnetism of [$Mn^{III}_9(\mu_3$-O)(μ_4-O)$_3$(salox-Me)$_6$(MeO)$_3$(CH$_3$COO)$_3$(H$_2$O)$_3$]$^+$, 19

The structure of the enneanuclear complex, **19**, is composed of eight Mn(III) ions and one Mn(II) ion. These Mn ions are placed in two planes which are oriented in parallel fashion as shown in Figure 75 with pink and blue shades. The upper plane contains three Mn(III) ions in an equilateral triangle configuration linked *via* μ_3-oxide (O7). The lower plane contains five Mn(III) ions and one Mn(II) ion forming three non-equilateral triangles linked *via* μ_3-oxides. In addition, there are six salox-Me^{2-} ligands in the equatorial position and three acetate ligands as well as three water molecules in the axial positions. The C_3 axis is perpendicular to the upper and lower Mn planes and passes through the central μ_3- oxide (O7). The latter atom lies 0.204 Å slightly above the upper Mn3 plane. All the edges of the upper triangle are bridged by N-O groups from the salox-Me^{2-} ligands with Mn-O-N-Mn torsion angles of 43.9°. In the lower Mn6 plane, edges of the triangles are linked *via* a combination of methoxide bridges with 96.3° and N-O bridges with torsion angles of 24.3°.

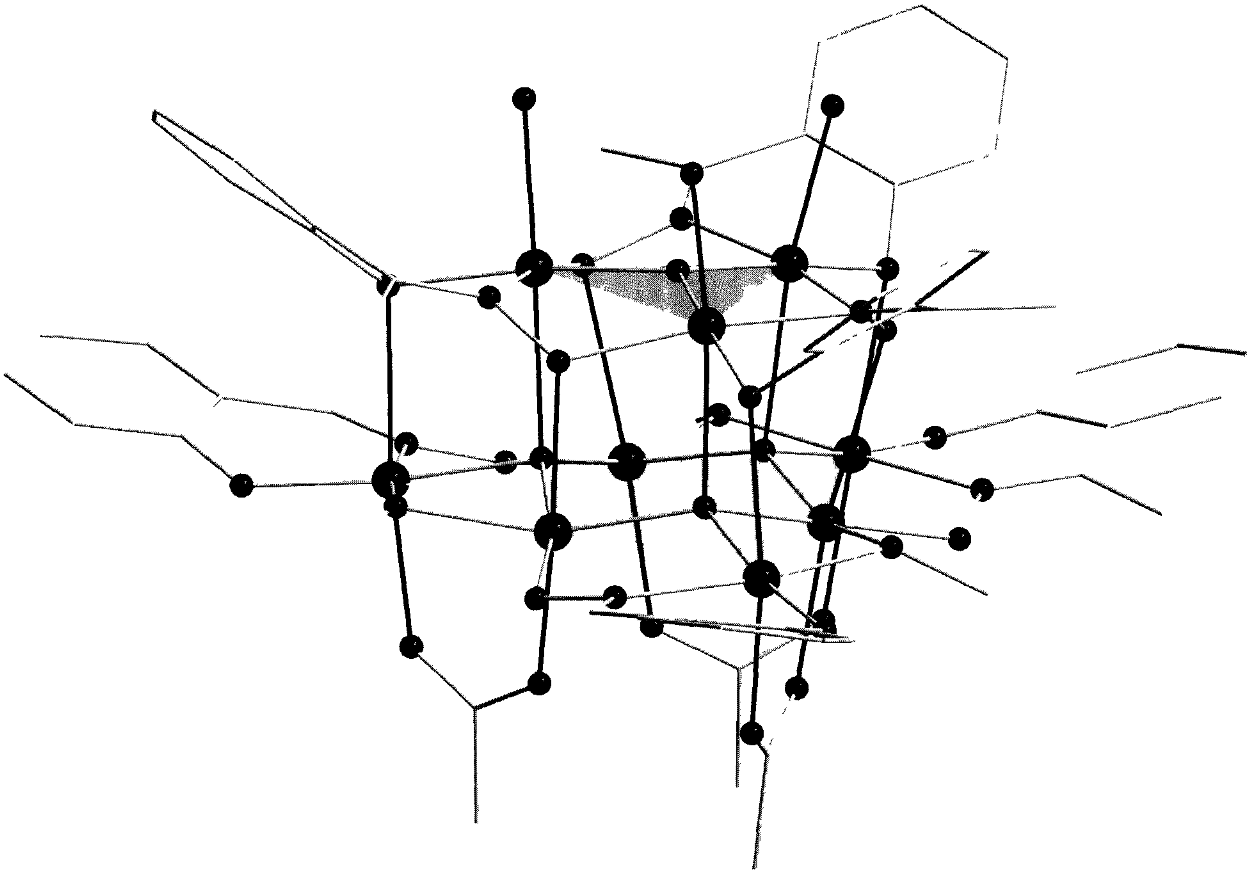

Figure 75. Molecular structure of $Mn^{III}_9(\mu_3\text{-O})(\mu_4\text{-O})_3(\text{salox-Me})_6(\text{MeO})_3(CH_3COO)_3(H_2O)_3]^+$, **19**.

The upper trianglar unit is very similar to **11**, containing the $[Mn^{III}(\mu_3\text{-O})]^{7+}$ core. The oxidation states of the Mn ions were established to be 3+ by charge considerations and the bond valence sum (BVS) calculations. In addition, the Jahn-Teller axes are aligned in near parallel fashion as shown in Figure 76. The packing arrangment within the crystal lactice along the *b* axis shows the Mn_9 units are well separated (Figure 77).

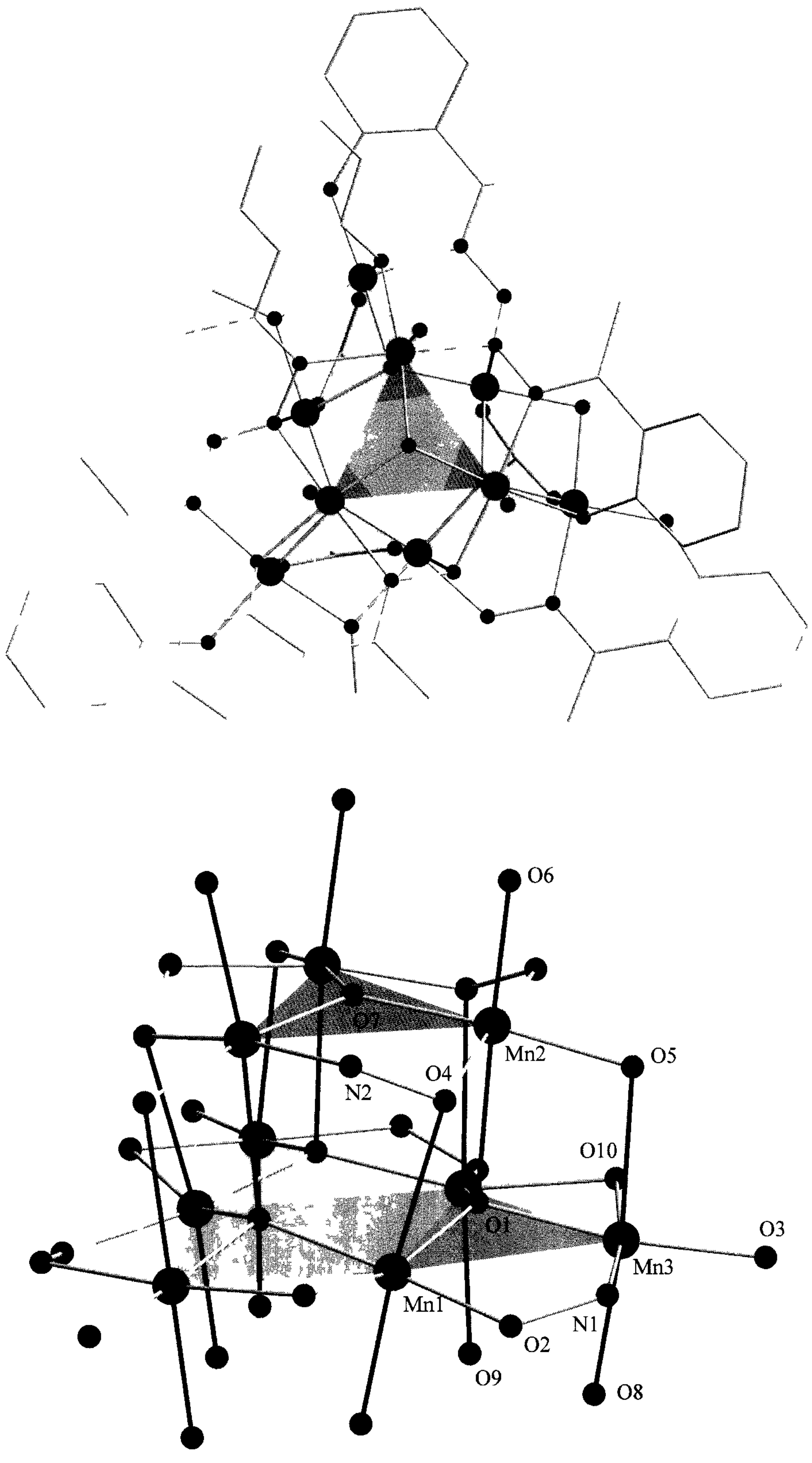

Figure 76. *Top* Top perspective along the C_3 axis of **19**. *Bottom* Core structure of **19.**

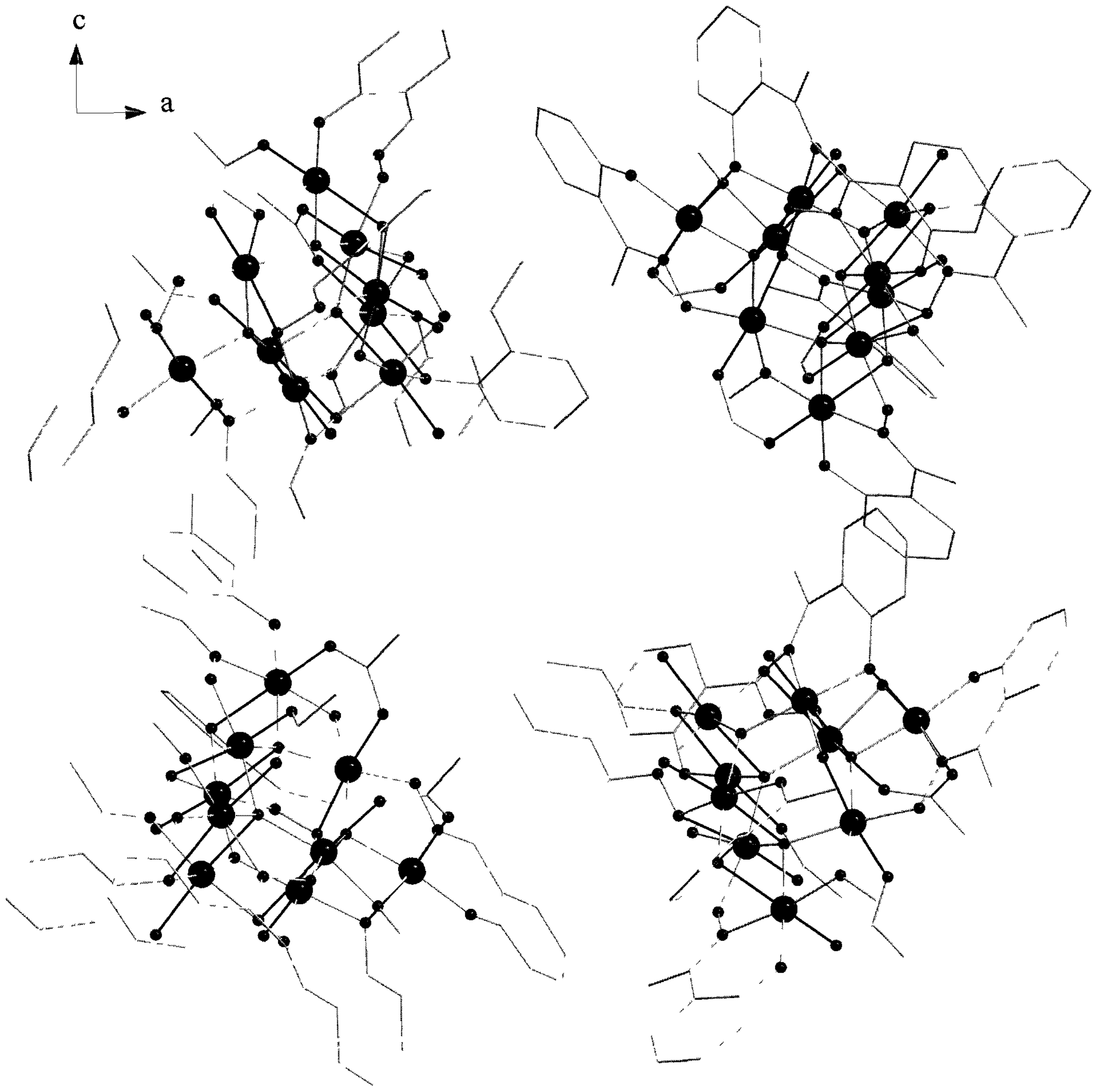

Figure 77. Packing arrangement of **19** along the *b* axis.

At room temperature, the χT product is 28.74 cm^3K/mol which is slightly high in comparison to the expected value of 27.0 cm^3K/mol for non-interacting Mn^{III} ions (g = 2.00; C = 3.00 cm^3K/mol) The χT product gradually decreases from 300 - 36 K reaching a minimum value of 20.8 cm^3K/mol at 1000 Oe (Figure 79). From 36 - 4.0 K, the product increases to a maximum of

22.6 cm^3K/mol and this is due to intramolecular ferromagetic interactions. The obtained value of the χT product at 4.0 K is close to the expected value of 24.38 cm^3K/mol for an S = 13/2 spin state. The top plane containing the Mn_3 triangle is ferromagnetically coupled to give an $S_T = 6$ and the Mn ions in the bottom plane are antiferromagnetically coupled to give an $S_T = 1/2$. Both sets of planes are ferromagnetically coupled giving rise to an $S_T = 13/2$. The oxidation states of the three Mn1 ion are delocalized with two 3+ and one 2+.

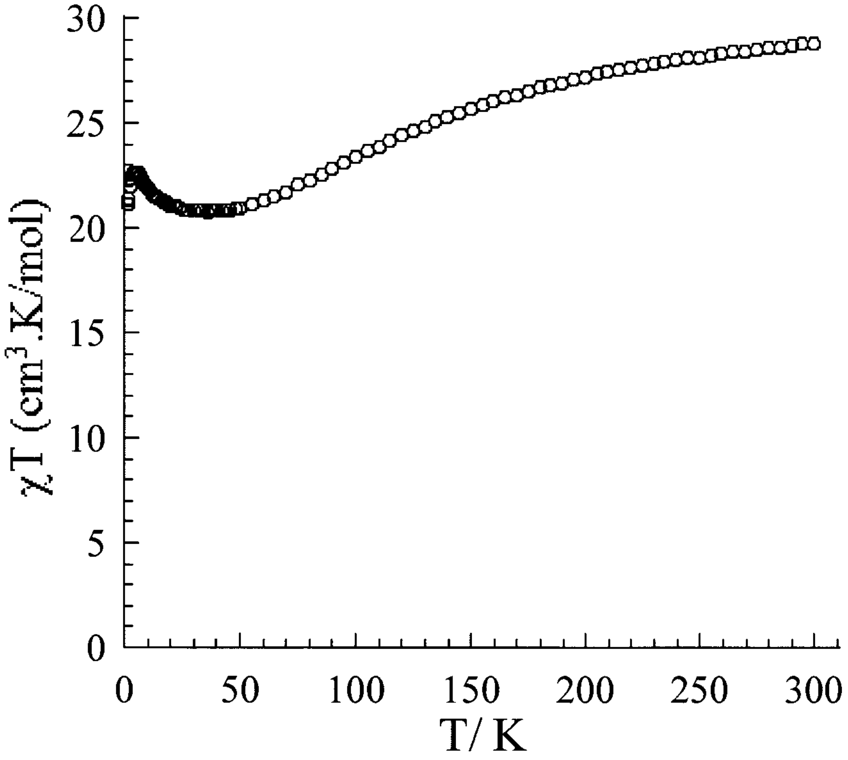

Figure 78. Plot of χT *vs.* T for complex **19** at 1000 Oe.

In order to confirm the magnitude of the spin ground state and the magnetic anisotropy, the magnetization, M *vs.* H/T data have been fitted to an S_T = 13/2 Brillouin function that leads to an excellent theory/ experiment agreement with a g factor of 2.05 and a D value of -0.423 cm^{-1} (Figure 79).

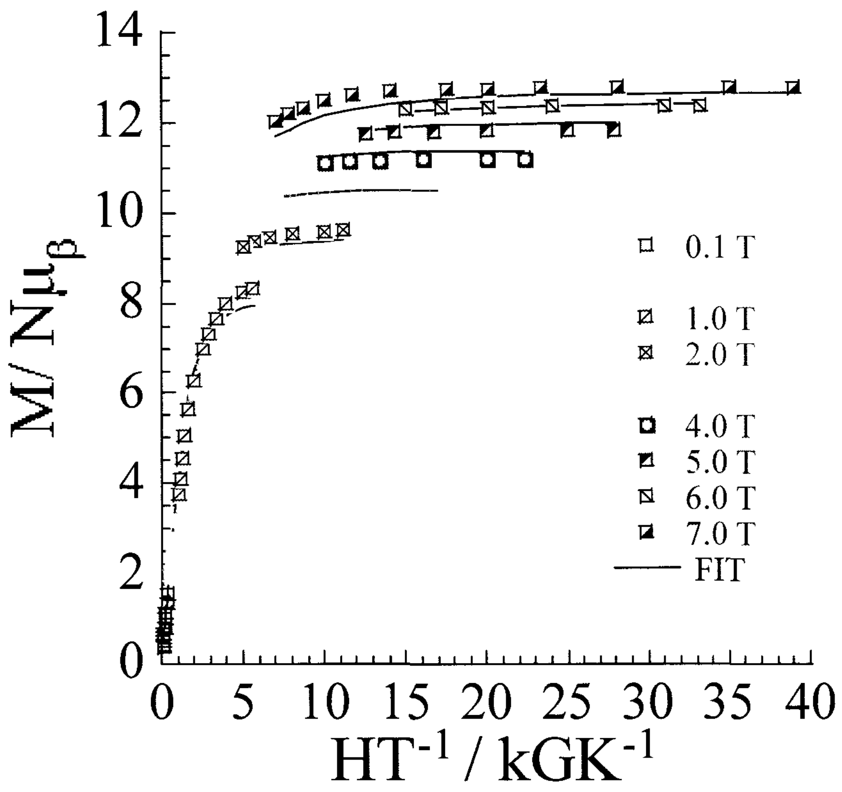

Figure 79. Plot of magnetization *vs.* Field/ Temperature along with the fit using the Brillouin function for an $S_T = 13/2$ (solid line).

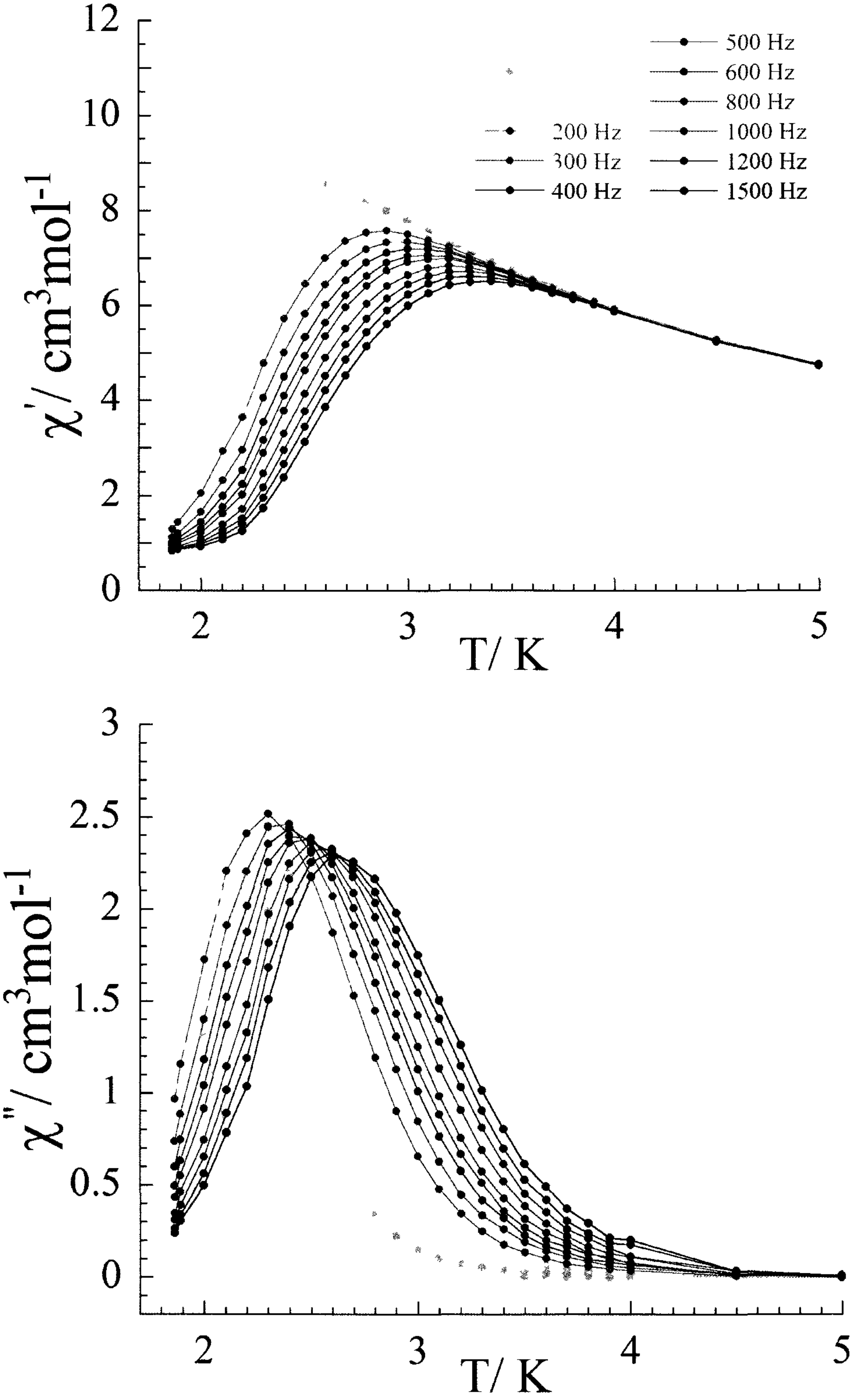

Figure 80. *Top:* ac magnetic susceptibility χ' as a function of temperature at frequency ranging from 1 to 1500 Hz. *Bottom:* χ'' out-of-phase component for **19**.

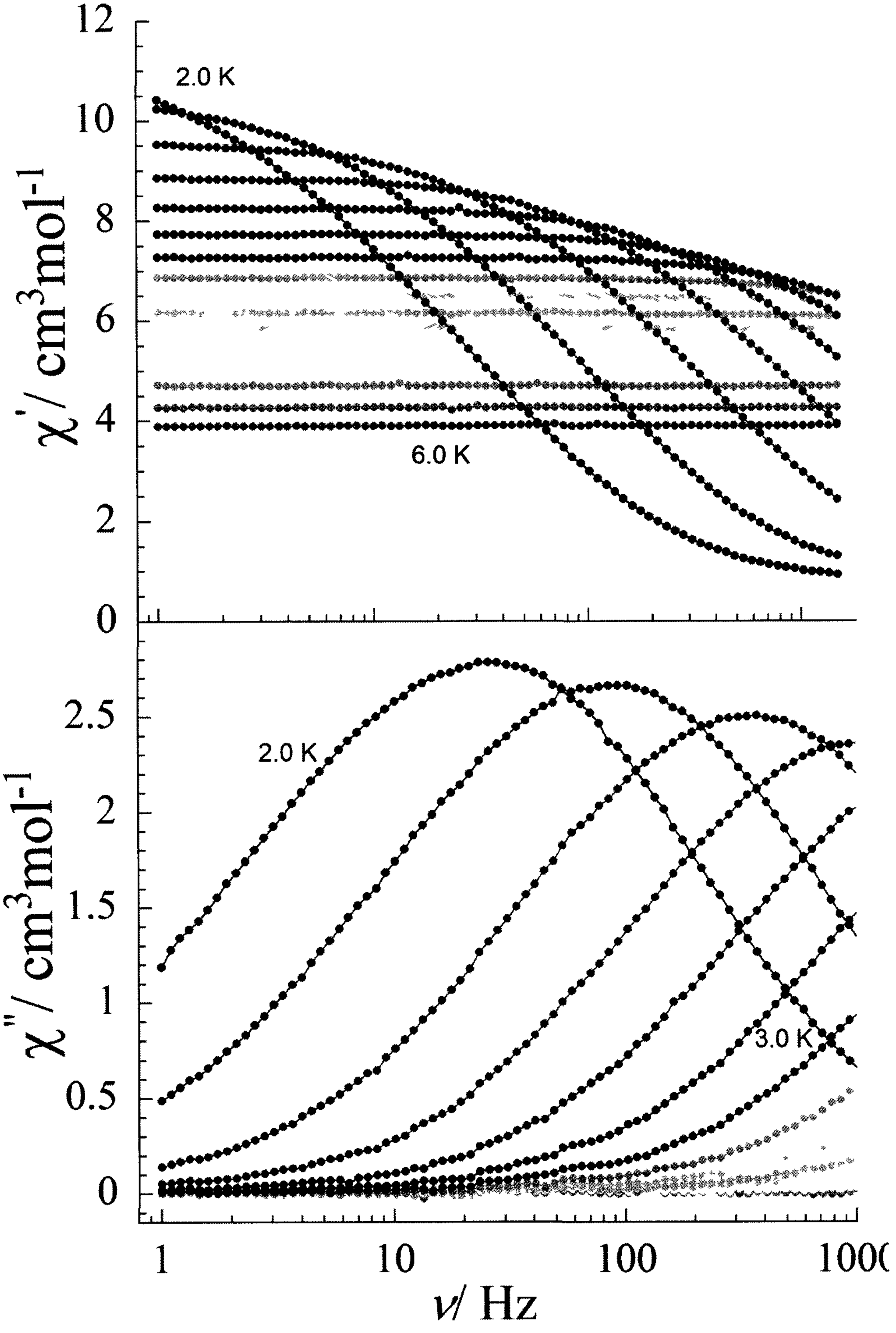

Figure 81. *Top:* ac magnetic susceptibility χ' as a function of frequency at temperature ranging from 2.0 to 6.0 K. *Bottom:* χ'' out-of-phase component for **19**.

ac magnetic susceptibility measurements were conducted between 1.8 - 10 K in function of frequency ranging from 10-1500 Hz (Figure 80), clear in-phase and out-of-phase component is seen which is a good indication that this molecule exhibits SMM behaviour. Measurements in function of temperature were also conducted and a similar trend was observed (Figure 81). The effective energy barrier was determined by extrapolating the maximum values of the out-of-phase component using the Arrhenius plot with $U_{eff} \sim 32.8$ K (Figure 82).

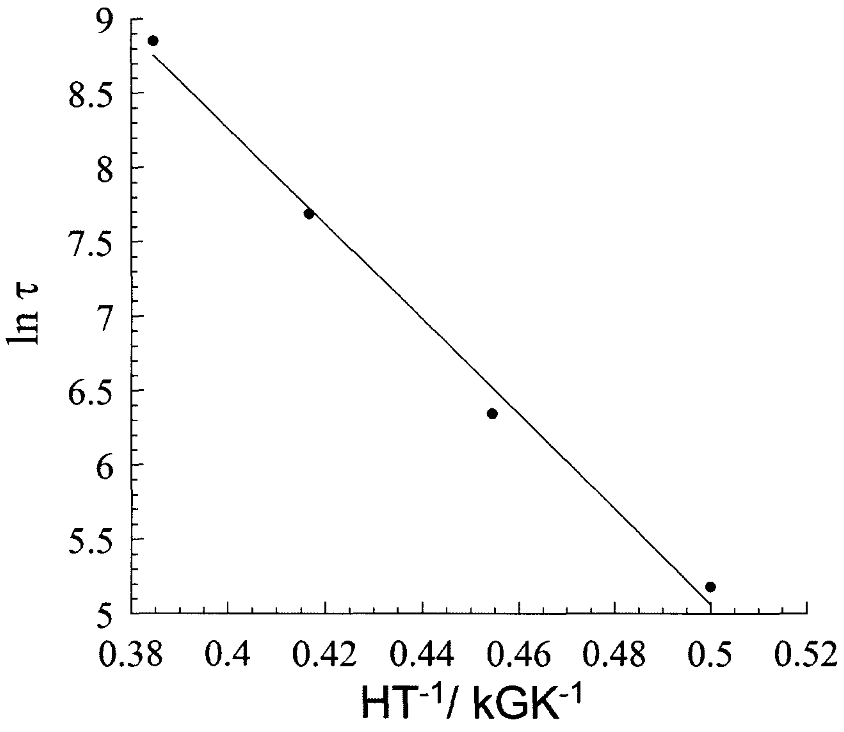

Figure 82. Arrhenius plot with a fit line for **19**.

6.3 Structure and Magnetism of $[Mn^{III}_9(\mu_3\text{-}O)(\mu_4\text{-}O)_3(\text{salox-Me})_6(MeO)_3(CH_3COO)_4(MeOH)_2(Phpy)]^+ \cdot MeCN$, 20

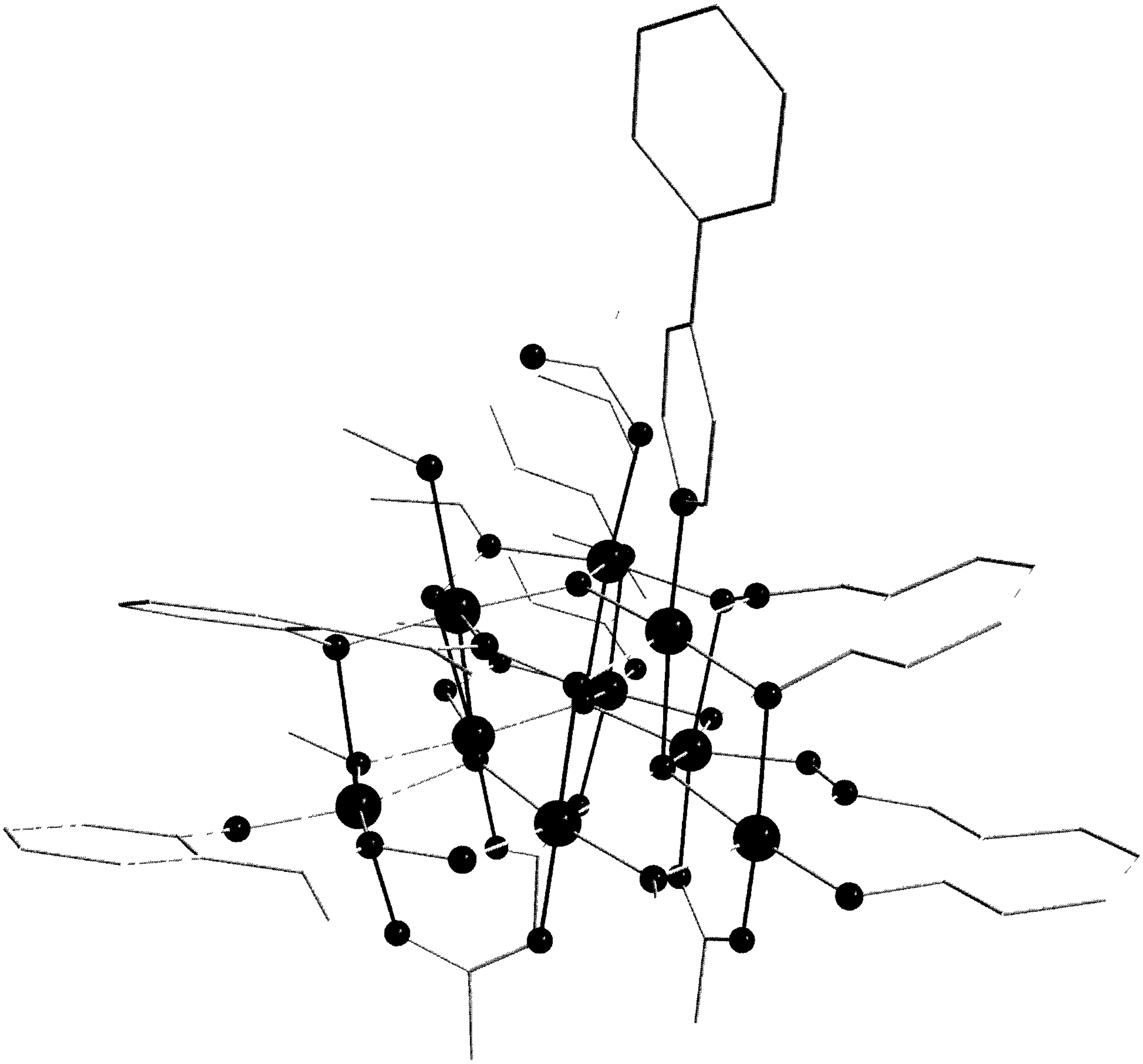

Figure 83. Molecular structure of $[Mn^{III}_9(\mu_3\text{-}O)(\mu_4\text{-}O)_3(\text{salox-Me})_6(MeO)_3(CH_3COO)_4(MeOH)_2(Phpy)]^+ \cdot MeCN$, **20.**

Complex **20**, $[\mathrm{Mn^{III}}_9(\mu_3\text{-O})(\mu_4\text{-O})_3(\text{salox-Me})_6(\mathrm{MeO})_3(\mathrm{CH_3COO})_4(\mathrm{MeOH})_2(\mathrm{Phpy})]^+\bullet\mathrm{MeCN}$, consists of one non-equilateral Mn(III)$_3$ triangle stacked on top of three non- equilateral triangles in-near planar fashion, analogous to **19** (Figure 83). The top triangle contains one phenylpyridine, one acetate and one methanol molecule which is coordinated to the Mn ions to complete the octahedral geometry. The central μ_3- oxygen (O7) lies 0.264 Å above the upper Mn$_3$ plane. The torsion angles along the Mn-O-N-Mn moiety on the top plane are relatively high ranging from 37° to 42°. The bottom plane contains three acetate molecules on the axial positions. The torsion angles are relatively low ranging from 8.9° to 12.4°. The methoxide bridges between the Mn ions in the bottom plane are 99.6°.

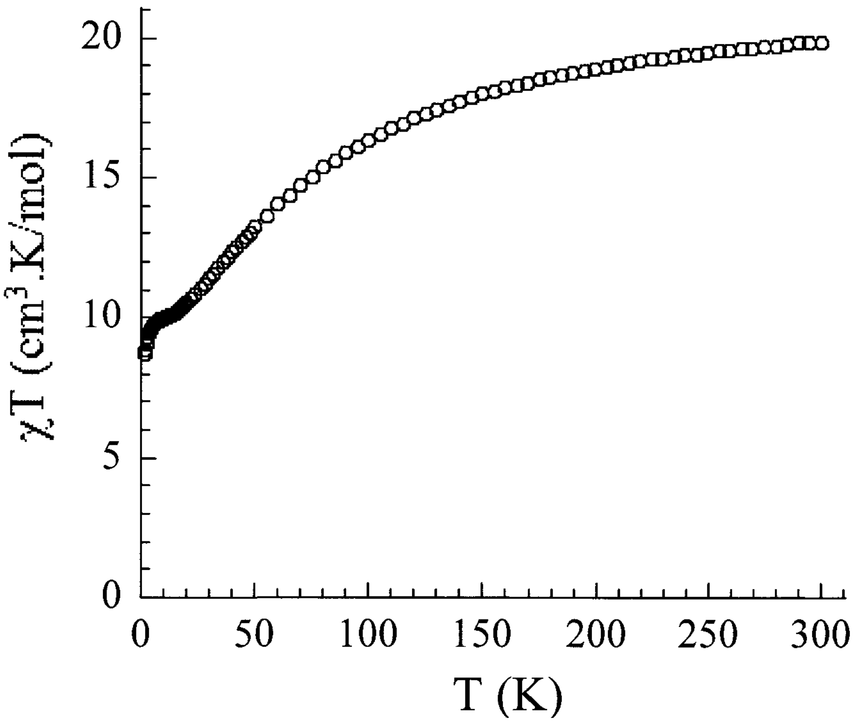

Figure 84. Plot of χT *vs.* T for complex **20** at 1000 Oe.

At room temperature, the χT product is 19.82 cm^{3}K/mol (Figure 84) which is low in comparison to the expected value of 27.0 cm^{3}K/mol for six non-interacting Mn(III) ions (g = 2.00; C = 3.00

cm^{3}K/mol). The χT product gradually decreases from 300 - 15 K reaching a minimum value of 10.8 cm^{3}K/mol and levels off and eventually decreases to 8.73 cm^{3}K/mol at 1.8 K. The decrease in χT product is indicative of dominant antiferromagnetic interaction in the [Mn$_9$] unit.

6.4 Structure and Magnetism of $[Mn^{III}_{18}(\mu_3\text{-}O)_2(\mu_4\text{-}O)_6(\text{salox-Et})_{12}(CH_3COO)_9(MeO)_6Cl]$, 21

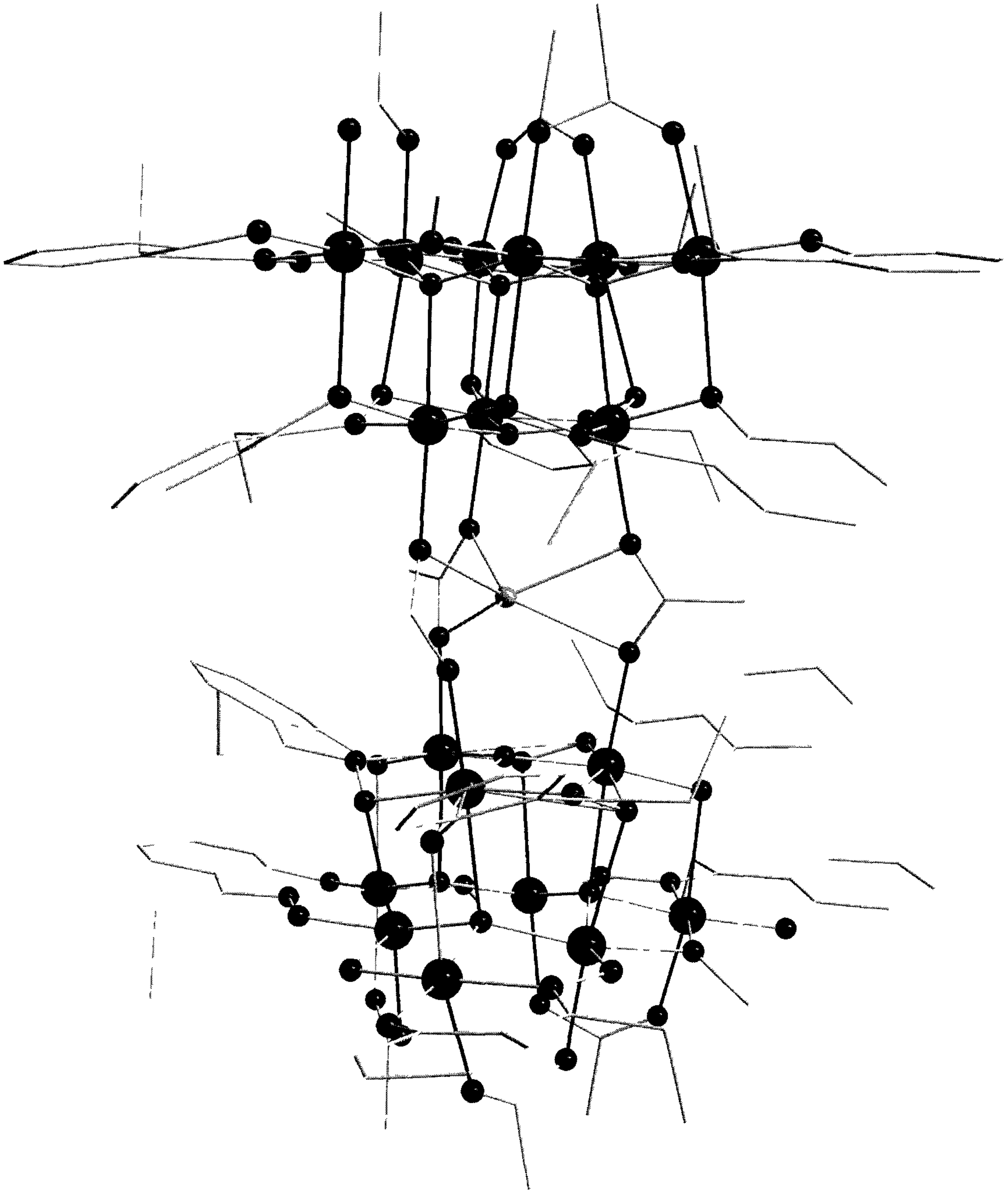

Figure 85. Molecular structure of $[Mn^{III}_{18}(\mu_3\text{-}O)_2(\mu_4\text{-}O)_6(\text{salox-Et})_{12}(CH_3COO)_9(MeO)_6Cl]$, **21**.

A larger manganese aggregate was isolated by tuning the reaction conditions and switching the equatorial ligand to salox-Et^{2-}. Complex **21**, $[Mn^{III}_{18}(\mu_3\text{-}O)_2(\mu_4\text{-}O)_6(\text{salox-Et})_{12}(CH_3COO)_9(MeO)_6Cl]$, is composed of two [$Mn_9$] units linked *via* acetates to form Mn_{18} (Figure 85). The three acetate molecules create an octahedral pocket for a chloride ion to be placed in. There is a total of 12 salox-Et ligand and six methoxides on the equatorial positions and six acetate molecules on the top and bottom of the [Mn_{18}] core. The inner two symmetrical [Mn_3] units are connected by three acetates. In addition, the torsion angles along the Mn-O-N-Mn group are 37.3°. The central O(7) atom lies 0.225 Å above the upper Mn_3 plane.

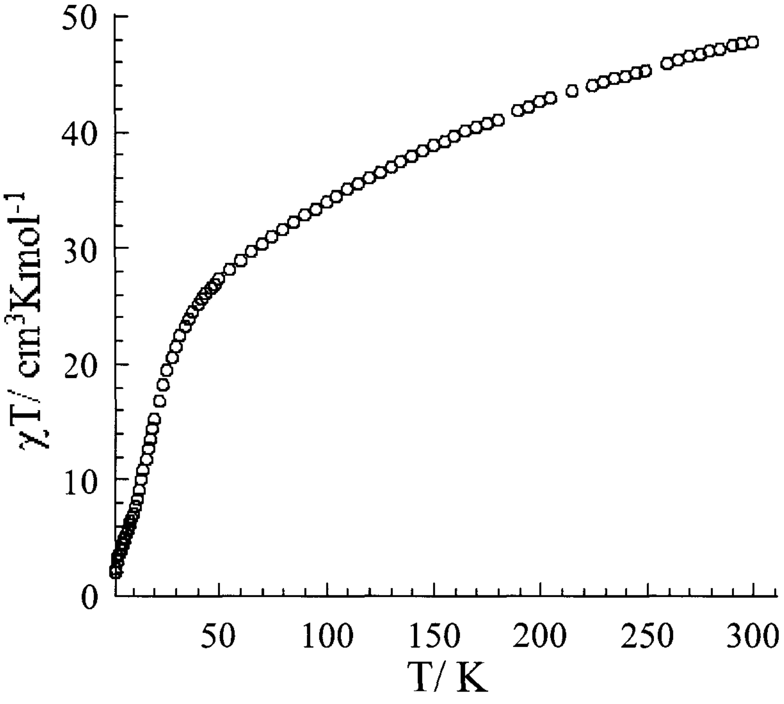

Figure 86. Plot of χT *vs.* T for complex **21** at 1000 Oe.

At room temperature, the χT product is 47.8 cm^{3}K/mol (Figure 86) which is low in comparison to the expected value of 54.0 cm^{3}K/mol for 18 non-interacting Mn(III) ions ($g = 2.00$; $C = 3.00$ cm^{3}K/mol). The χT product gradually decreases from 300 - 1.8 K reaching a minimum value of 1.97 cm^{3}K/mol which is indicative of dominant antiferromagnetic interactions in the [Mn_{18}] unit.

Chapter 7

7 Conclusion

A systematic approach to the development and synthesis of multinuclear complexes has been demonstrated in this thesis. The chapters are sequentially arranged in increasing nuclearity and atomic configuration (i.e. linear Mn_3, triangular Mn_3, Mn_6, Mn_7, Mn_9, Mn_{18} and Mn_{23}). Each compound was characterized exclusively by X-ray crystallography and magnetic measurements. The former allows us to establish the spin ground state and magnetic anisotropy to ultimately determine whether the molecule exhibits SMM behaviour. In addition, a magneto-structural correlation was conducted for each molecule allowing us to study the nature and strength of interaction between metal centers. Two basic repeating units, linear Mn_3 and triangular Mn_3, have been utilized in the synthesis of larger metal aggregates as shown in Figure 87.

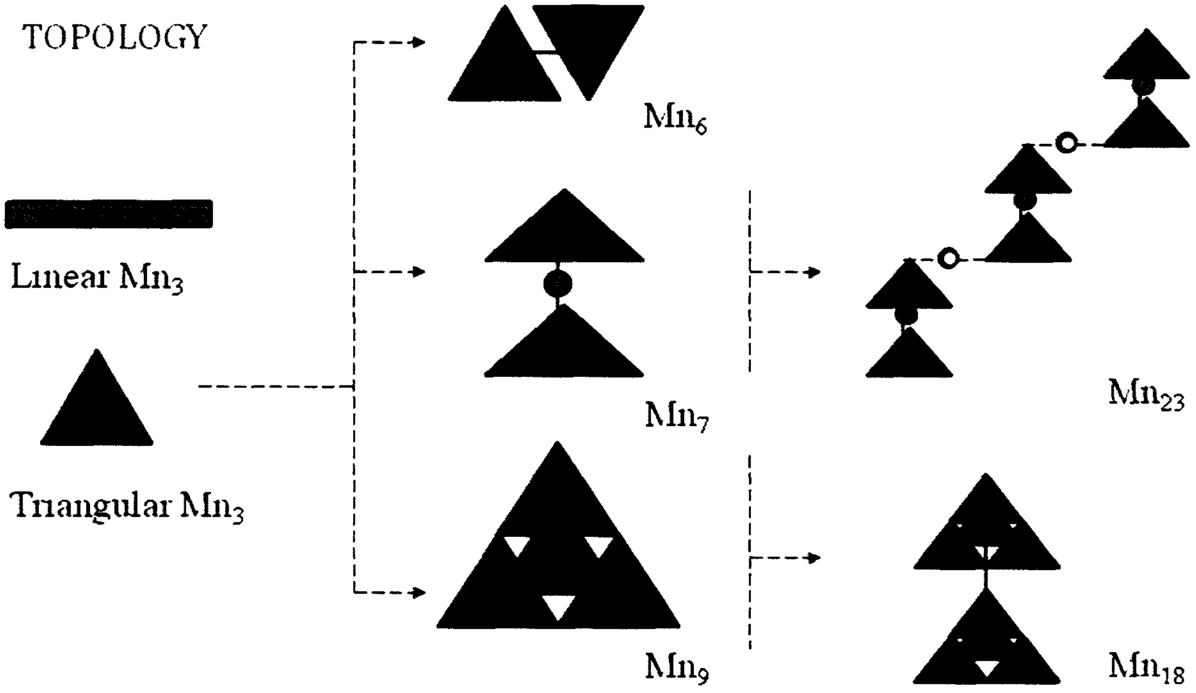

Figure 87. Topology chart depicting the basic repeating units.

A total of 21 manganese complexes were synthesized in an attempt to achieve high energy barrier SMMs. In order to accomplish this, one needs to understand the true origin of ferromagnetism and magnetic anisotropy. It is essential for a magneto-chemist to be able to synthetically control the structural growth, and in turn, achieve large spin ground state as well as uniaxial magnetic anisotropy. Each chapter was discussed in regards to achieving SMM behaviour by tweaking one or both requirements.

In chapter 2, three linear Mn_3 complexes were reported. All three Mn ions in complex **1** and **2** are in the 4+ oxidation states that are ferromagnetically coupled giving rise to $S_T = 9/2$. However, both compounds do not exhibit SMM behaviour due to the absence of magnetic anisotropy. In an attempt to introduce anisotropy to the central Mn ion, an alternate multi-dentate ligand was employed in the presence of sodium hydroxide. This resulted in the isolation of **3** with the central Mn ion being in the 3+ oxidation state ferromagnetically coupled to two manganese 4+ ions resulting in $S_T = 5$. After introducing anisotropy, there is clear evidence that **3** exhibits SMM properties with a tail of a peak for ac magnetic susceptibility with an out-of-phase component.

In chapter 3, eight triangular Mn_3 complexes were characterized structurally and magnetically. A systematic approach to synthesizing the $Mn(III)_3$ triangles was employed, where the ferromagnetic interactions were induced by means of ligand modification. Complexes **4 - 10** are antiferromagnetically coupled to give rise to $S_T = 0 - 2$ with no signs of SMM behaviour. By switching the equatorial ligand to a six-membered chelating ring with a methyl group on the C1 position, complex **11** was isolated with $S_T = 6$. By increasing the spin ground state of the molecule, **11** was shown to exhibit SMM behaviour with $U_{eff} = 39$ K. This chapter essentially demonstrates that ferromagnetism arises from two factors; a six-membered coordination ring and a high dihedral angle along the oxime bridge, Mn-NO-Mn.

In chapter 4, two Mn_6 complexes were reported. Complexes **12** and **13** contain the triangular Mn_3 unit linked side on *via* four methoxide bridges. Both complexes exhibit ferromagnetic interactions within the Mn_6 units resulting in $S_T = 11$. There is negligible anisotropy which generally arises from the Mn(III) ions, however, both Jahn-Teller axes are perpendicular to one another thereby cancelling out the anisotropy. Hence no SMM behaviour was observed in the magnetic measurements.

In chapter 5, four Mn_7 clusters and one Mn_{23} complex were reported. The focus of this chapter was to essentially show that it is possible to link the Mn_3 units using 1,2 diol molecules in solution. This allows the Jahn-Teller axes to be aligned in one direction giving rise to large anisotropy. The two sets of Mn_3 units are linked through three 1,2 diols which are coordinated to Mn(IV) ion and hence allow the two units to communicate. Complexes **14** - **17** exhibit antiferromagnetic interaction with an $S_T = 5/2$ where the Jahn-Teller axes are aligned in near parallel arrangement. However, no ac out of phase component was observed due to minimal spin ground state. Complex **18** contains three Mn_7 units which are linked through two monomeric Mn(II) ions resulting in a Mn_{23} cluster. Magnetically, it is equivalent to the Mn_7 unit. These units do not communicate with each other and again the Mn_7 unit exhibits antiferromagnetic interaction.

In chapter 6, two Mn_9 and one Mn_{18} complex were reported. Complexes **19** and **20** contain the basic repeating Mn_3 unit which are arranged in stacked formation with Mn ions in two different planes. Complex **19** exhibits antiferromagnetic interaction with an $S_T = 13/2$. By switching the equatorial ligand to H_2salox-Et, complex **21** was isolated which contains two Mn_9 units linked by 3 acetate molecules. Complex **21** exhibits dominant antiferromagnetic interaction with no signs of ac peak for the out of phase component.

Linear Mn_3 Complexes:

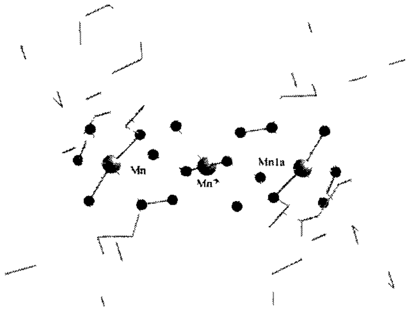

[1]

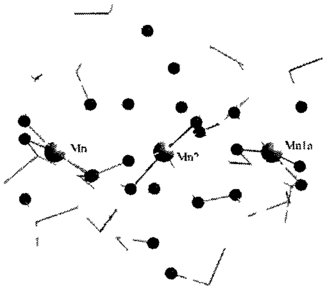

[2]

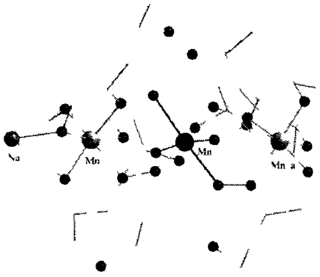

[3]

Triangular Mn_3 Complexes:

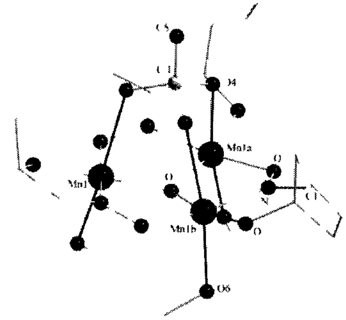

[4]

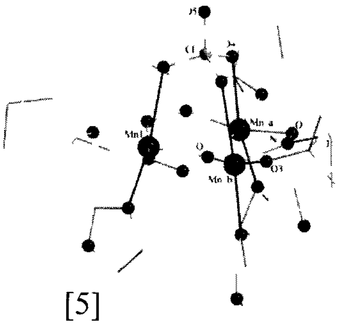

[5]

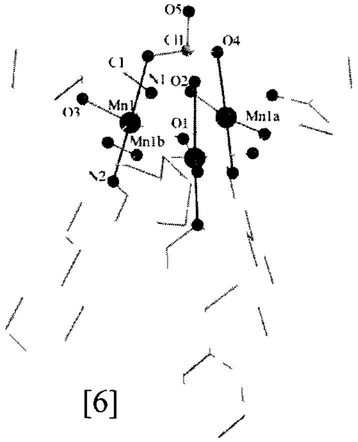

[6]

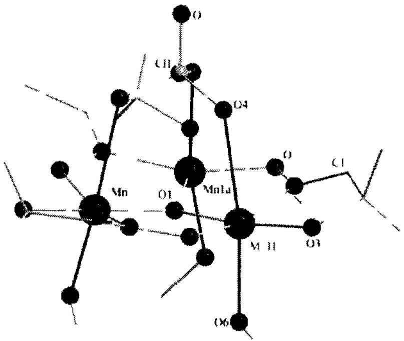

[7]

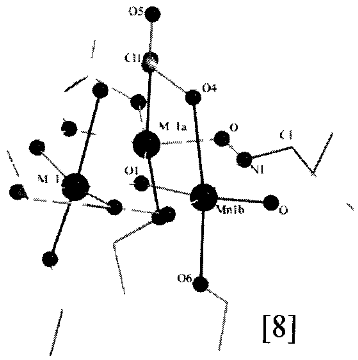

[8]

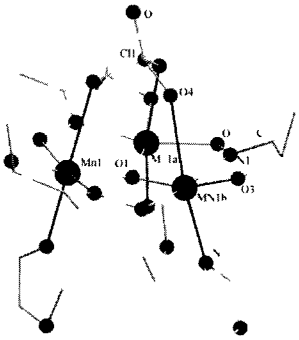

[9]

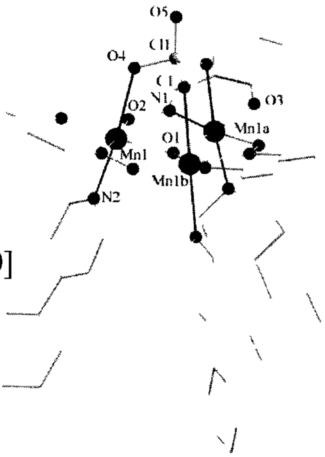

[10]

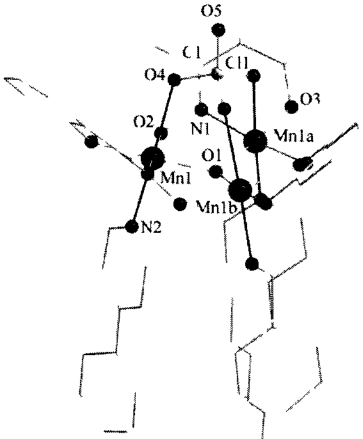

[11]

Mn$_6$ Complexes:

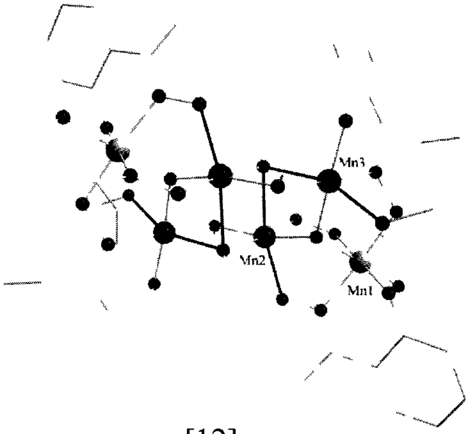

[12]

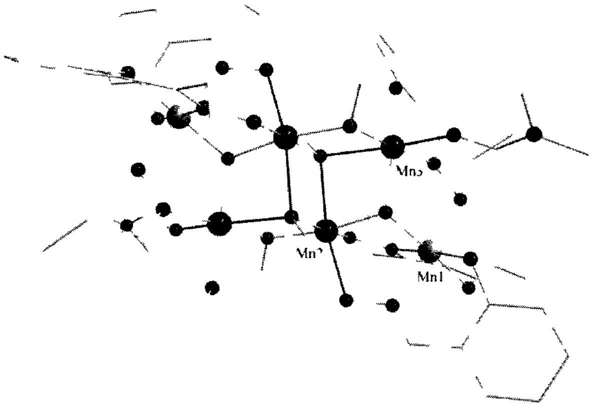

[13]

Mn$_7$ Complexes:

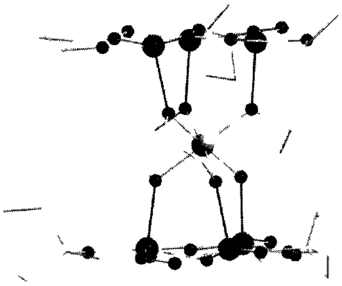

[14]

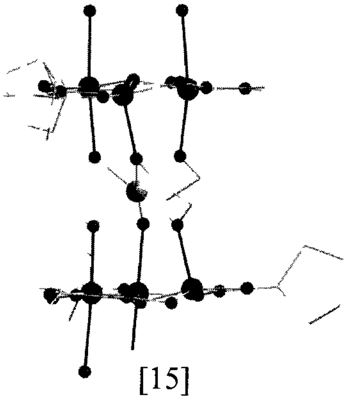

[15]

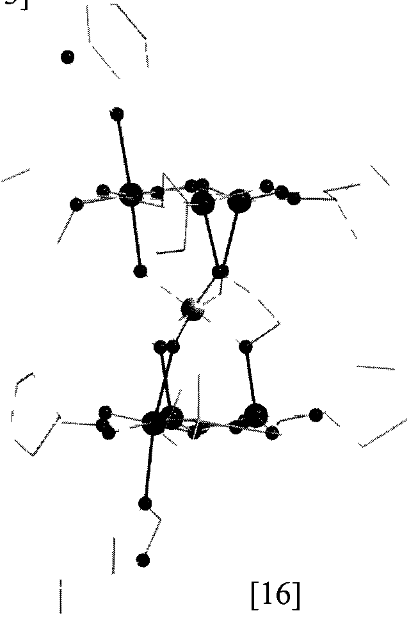

[16]

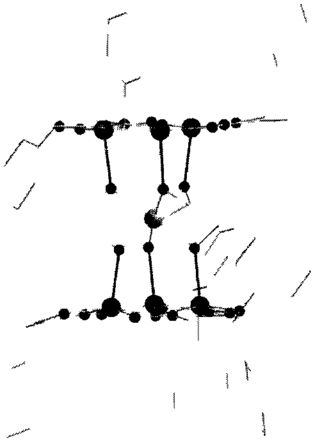

[17]

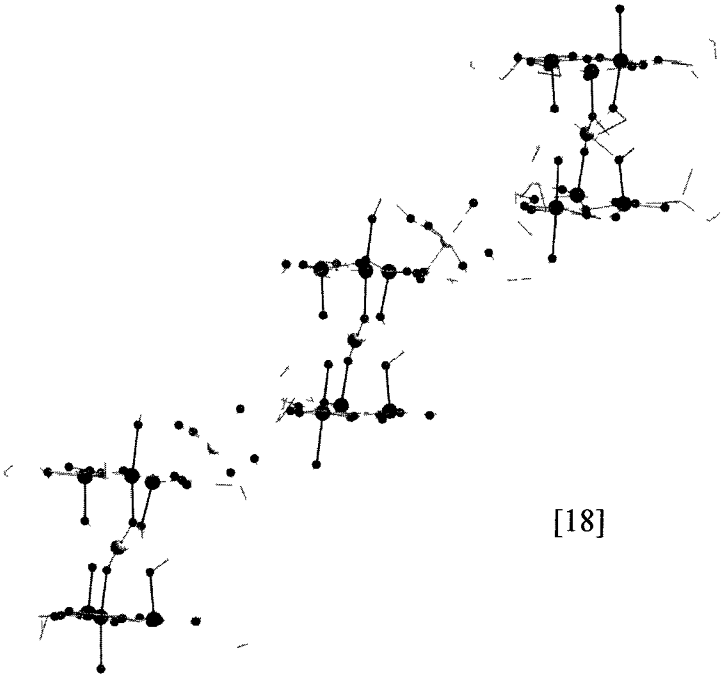

[18]

Mn_9 Complexes:

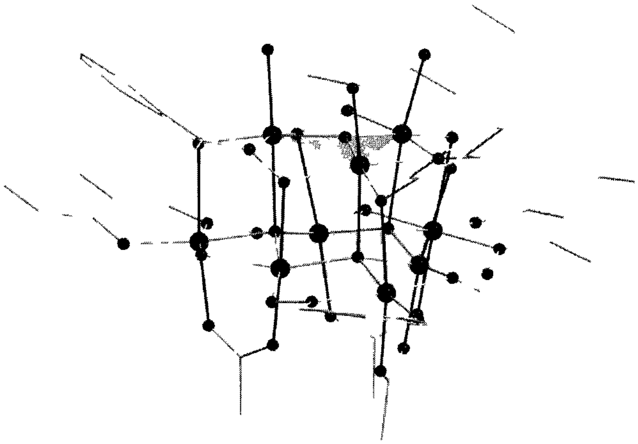

[19]

[20]

Mn_{18} Complex:

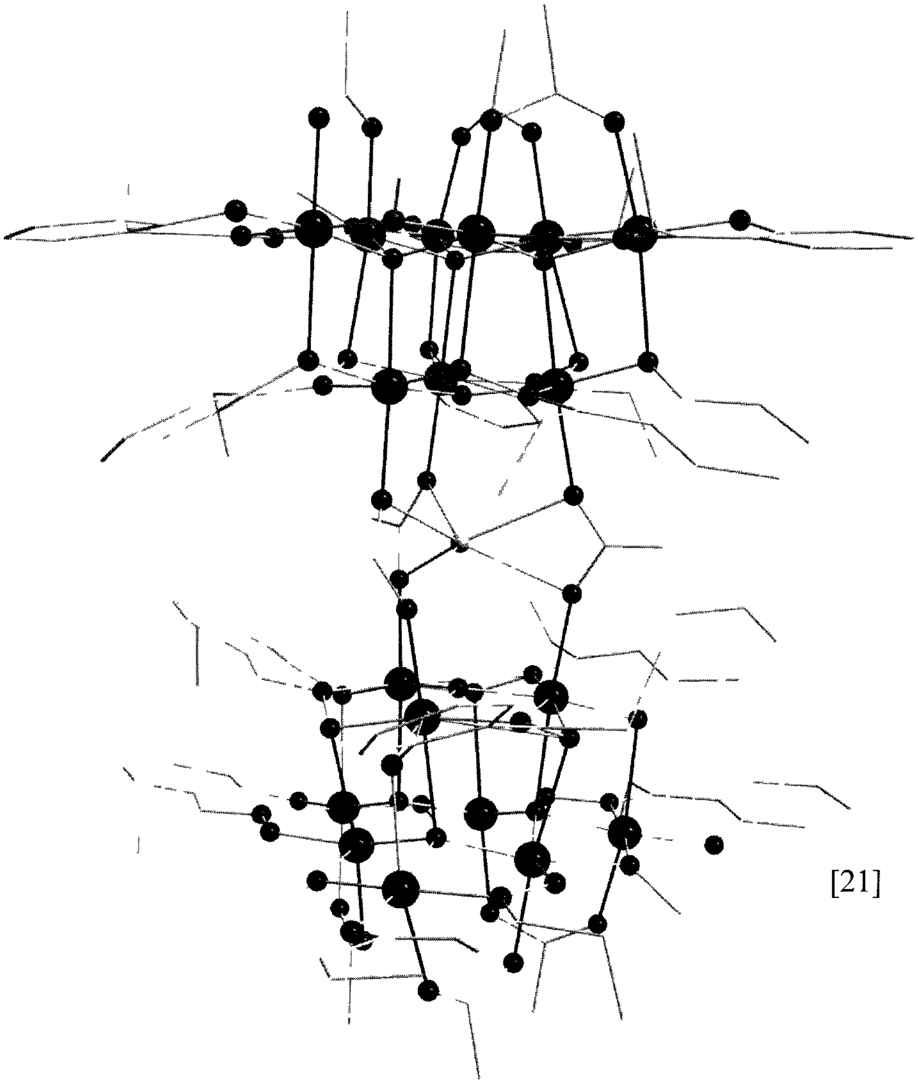

[21]

Chapter 8

8.1 Experimental

8.1.1 NMR Spectroscopy

The NMR measurements were conducted using the Bruker Avance 400 MHz spectrometer.

8.1.2 Infra-Red Spectroscopy

Infrared spectroscopy was performed on a Magna-IR 550 spectrometer in the 4000-700 cm^{-1} region.

8.1.3 Elemental Analysis

Elemental analyses for C, N and H were carried out using the Perkin-Elmer Series II 2400.

8.1.4 X-ray Crystallography

Single crystals **1**- **21** suitable for X-ray diffraction measurements were mounted on a glass fibre. In order to obtain a diffraction pattern, a beam of X-ray (wavelength ranging from 10 - 0.1 nm) strikes a crystal which is placed on a goniometry and diffracts into many directions. From the angle and intensity, a crystallographer can produce a 3-D image of the density of electrons. A typical wavelength used for crystallography is 1.0 Å, which is an excellent resolution since it is in the scale of a covalent chemical bond and a radius of a single atom.[17] Unit cell measurements and intensity data collections were performed on a Bruker-AXS SMART 1 k CCD diffractometer using graphite monochromatized Mo K_{α} radiation (λ = 0.71073 Å).

The data reduction included a correction for Lorentz and polarization effects, with an applied multi-scan absorption correction (SADABS). The crystal structures were solved and refined using the SHELXTL program suite.

8.1.5 SQUID Magnetometer

The variable temperature magnetic susceptibility measurements were obtained using a Quantum Design SQUID MPMS-XL magnetometer which operates between 1.8 and 300 K for dc applied fields up to 7 T. Measurements were performed on polycrystalline samples of approximately 10- 20 mg. ac susceptibility measurements were carried out under an oscillating ac field of 3 Oe and ac frequencies ranging from 1 to 1500 Hz. The magnetic data were corrected for the sample holder.

8.1.6 Density Functional Theory Calculations (DFT)

Density functional theory calculations were performed using the *Gaussian 03* program and the B3LYP exchange-correlation functional.

8.2 Organic Synthesis

8.2.1 Preparation of Ligand I: (E)-1-hydroxypropan-2-one oxime (H_2dho)

An oven-dried sealed tube (48 mL), equipped with a magnetic stir bar and a rubber septum was purged with an argon balloon for 5 minutes. Prop-2-yn-1-ol (3.16 mL, 53.56 mmol), aqueous hydroxylamine (8.2 mL of a 50 wt% solution, 133.8 mmol) and isopropanol (freshly distilled, 27 mL) were added to the reaction vessel while keeping a constant flow of argon. The rubber septum was quickly replaced by a Teflon treaded cap. The mixture was heated in a wax bath for 70 hours at 110 °C. After cooling the mixture to room temperature, the crude was concentrated under reduced pressure, purified through column chromatography (40 % EtOAc/Hexanes → 100 % EtOAc) and recrystallized from hot hexanes. Oxime, H_2dho, (R_f: 0.1 in 30 % EtOAc/Hexanes) was isolated as a white powder (3.98 g, 84 % yield). ^{1}H NMR ($(CD_3)_2CO$, 400 MHz) 9.78 (br s, 1H), 4.20 (br s, 1H), 4.03 (s, 2H), 1.84 (s, 3H); ^{13}C NMR ($(CD_3)_2CO$, 100 MHz) 155.8, 63.8, 10.0; IR (film, cm^{-1}): 3453, 2871, 1666, 1456, 1223, 1044, 1018, 951; HRMS (EI): Exact mass calcd for $C_3H_7NO_2$ [M]+: 89.0477. Found: 89.0467.

8.2.2 Preparation of Ligand II:
(E)-3-hydroxy-3-methylbutan-2-one oxime (H_2dmo)

2-Methylbut-3-yn-2-ol (5.4 mL, 54 mmol), aqueous hydroxylamine (8.2 mL of a 50 wt% solution, 133 mmol) and isopropanol (freshly distilled, 27 mL) were added to the reaction vessel while keeping a constant flow of argon. The rubber septum was quickly replaced by a Teflon treaded cap. The mixture was heated in a wax bath for 70 hours at 110 °C. After cooling the mixture to room temperature, the crude was concentrated under reduced pressure, purified through column chromatography (40 % EtOAc/Hexanes → 15 % MeOH/CH_2Cl_2) and recrystallized from hot hexanes. Oxime, H_2dho, (R_f: 0.1 in 30 % EtOAc/Hexanes) was isolated as a white solids (4.74 g, 75 % yield). ^{1}H NMR ($(CD_3)_2CO$, 400 MHz) 9.64 (br s, 1H), 4.00 (br s, 1H), 1.85 (s, 3H), 1.29 (s, 6H); ^{13}C NMR ($(CD_3)_2CO$, 100 MHz) 162.7, 73.5, 29.2, 10.3; IR (film, cm^{-1}): 3347, 2982, 2940, 1362, 1168, 943, 853, 757; HRMS (EI): Exact mass calculated for $C_5H_{11}NO_2$ [M]+: 117.0790. Not found. Exact mass calcd for $C_5H_{10}NO$ [M-OH]+: 110.0762. Found: 110.0761.

8.2.3 Preparation of Ligand III: (E)-3-ethyl-3-hydroxypentan-2-one oxime (H_2deo)

An oven-dried microwave tube (20 mL), equipped with a magnetic stir bar and a rubber septum was purged with an argon balloon for 5 minutes. 3-ethylpent-1-yn-3-ol (1.92 mL, 15.0 mmol), aqueous hydroxylamine (2.3 mL of a 50 wt% solution, 37.5 mmol) and isopropanol (freshly distilled, 15 mL) were added to the reaction vessel while keeping a constant flow of argon. The rubber septum was quickly replaced by a microwave aluminum cap. The mixture was heated in a Biotage microwave for 4hours at 140 °C. After cooling the mixture to room temperature, the crude was concentrated under reduced pressure, purified through column chromatography (25 % EtOAc/Hexanes). Oxime, H_2deo, (R_f: 0.59 in 40 % EtOAc/Hexanes) was isolated as a white powder (1.62 g, 74 % yield). ^{1}H NMR (acetone-d_6, 400 MHz) δ 9.90 (br s, 1H), 3.87 (br s), 1.78 (s, 3H), 1.68-1.50 (m, 4H), 0.74 (t, 7.4 Hz, 3H); ^{13}C NMR (acetone-d_6, 100 MHz) δ 160.0, 78.6, 33.0, 11.0, 8.9; IR (film, cm^{-1}) 3335, 2969, 2937, 2888, 1584, 1462, 1371, 1226, 1162, 1018, 967, 892, 736; HRMS (EI): Exact mass calcd for $C_7H_{15}NO_2$ $[M]^+$: 145.11028. Not Found. Exact mass calcd for $C_7H_{14}NO$ $[M]^+$: 128.1080. Found: 128.1094.

8.2.4 Preparation of Ligand IV: (E)-1-(1-hydroxycyclopentyl)ethanone oxime (H_2cpo)

1-(1-Hydroxycyclopentyl)- ethyne (1.65 g, 15.0 mmol), aqueous hydroxylamine (2.30 mL of a 50 wt% solution, 37.5 mmol) and freshly distilled isopropanol (15 mL) were transferred to a microwave reaction vessel under a constant flow of argon. The mixture was heated and stirred in a Biotage Initiator microwave for 4 hours at 140 °C. After cooling to room temperature, the crude was concentrated under reduced pressure, and recrystallized from hot 20% EtOAc/hexanes. Two recrystallizations afforded the oxime, H_2cpo, as a white powder (1.76 g, 81 % yield). TLC R_f 0.52 (50 % EtOAc/Hexanes); ^{1}H NMR ($CDCl_3$, 300 MHz) δ 8.12 (br s, 1H), 3.00 (br s), 1.98-1.79 (m, 7H), 1.79-1.60 (m, 4H); ^{13}C NMR ($CDCl_3$, 75 MHz) δ 161.0, 84.5, 39.4, 25.3, 11.3; IR (film, cm^{-1}) 3344, 2968, 1736, 1367, 1223, 1216, 725; HRMS (EI): Exact mass calcd for $C_7H_{12}NO$ $[M\text{-}OH]^+$: 126.092. Found: 126.0929.

8.2.5 Preparation of Ligand V: (E)-1-hydroxy-1,1-diphenylpropan-2-one oxime (H_2dpo)

An oven-dried microwave tube (10 mL), equipped with a magnetic stir bar and a rubber septum was purged with an argon balloon for 5 minutes. 1,1-diphenylprop-2-yn-1-ol (1.25 g, 6.0 mmol), aqueous hydroxylamine (0.92 mL of a 50 wt% solution, 15.0 mmol) and isopropanol (freshly distilled, 6 mL) were added to the reaction vessel while keeping a constant flow of argon. The rubber septum was quickly replaced by a microwave aluminum cap. The mixture was heated in a CEM microwave for 4 hours at 140 °C. After cooling the mixture to room temperature, the crude was concentrated under reduced pressure, purified through column chromatography (7.5 % EtOAc/Toluene). Oxime, H_2dpo, (R_f: 0.21 in 10 % EtOAc/hexane) was isolated as a white powder (1.05 g, 78 % yield). ^{1}H NMR (DMSO-d_6, 300 MHz) δ 10.90 (s, 1H), 7.31-7.30 (m, 8H), 7.28-7.18 (m, 2H), 6.41 (s, 1H), 1.81 (s, 3H); ^{13}C NMR (DMSO-d_6, 75 MHz) δ 159.6, 145.1, 127.4, 127.3, 126.5, 80.9, 12.0; IR (film, cm^{-1}): 3332, 1659, 1602, 1488, 1443, 1374, 1051, 1013, 968, 880, 758, 728, 694; HRMS (EI): Exact mass calcd for $C_{15}H_{14}NO$+[M-OH]+: 224.1070; found: 224.1053.

8.2.6 Preparation of Ligand VI: (E)-1-(dimethylamino)propan-2-one oxime (Hndo)

An oven-dried sealed tube (75 mL), equipped with a magnetic stir bar, was purged with argon for 5 minutes. 3-(Dimethylamino)-1-propyne (3.24 mL, 30.0 mmol), aqueous NH_2OH (2.76 mL of a 50 wt% solution, 45.1 mmol) and isopropanol (freshly distilled, 30 mL) were added to the reaction vessel under a constant flow of argon. The mixture was heated in a wax bath for 48 hours at 100 °C. After cooling to room temperature, the mixture was concentrated under reduced pressure and recrystallized from hot hexanes. Oxime, Hndo, was isolated as clear transparent crystals (2.47 g, 71 % yield); ^{1}H NMR (DMSO-d_6, 300 MHz) δ 9.39 (br, s, 1H), 2.95 (s, 2H), 2.22 (s, 6H), 1.93 (s, 3H); ^{13}C NMR (DMSO-d_6, 75 MHz) δ 156.4, 63.6, 45.3, 12.3; IR (KBr pellet, cm^{-1}): 2964 (s), 2877 (s), 2839 (s), 2724 (br), 1853 (w), 1657 (w), 1470 (s), 1279 (s), 1258 (s), 1181 (m), 1041 (s), 959 (s), 933 (s), 850 (s), 674 (m). HRMS (EI): Exact mass calcd for $C_5H_{11}NO$ $[M]^+$: 116.0950, Found: 116.0941.

8.2.7 Preparation of Ligand VII:
(E)-2-hydroxybenzaldehyde oxime (H_2salox-H)

Commercially available and can be purchased from Aldrich. CAS #: 94-67-7

8.2.8 Preparation of Ligand VIII:
(E)-1-(2-hydroxyphenyl)ethanone oxime (H_2salox-Me)

To a solution of ketone (6.80 g, 50.0 mmol) in ethanol (20 mL) kept under argon with constant stirring was added hydroxylamine hydrochloride (6.95 g, 22.0 mmol) and sodium acetate (12.3 g, 150 mmol) in 1:1 ethanol: water (40 mL). The mixture was heated at 60 °C for 3 hours, and then concentrated under reduced pressure. As the ethanol was removed, the product precipitated from water and was filtered to afford the crude product as a slightly pink solid. The crude was recrystallized from boiling water (200 mL) and filtered. A minor product crystallized as pink chunks in the bottom and was manually removed from the filtered crystals. Oxime, H_2salox-Me, was obtained as a white powder (5.80 g, 77 % yield). TLC R_f: 0.42 (20 % EtOAc/Hexanes); ^{1}H NMR (DMSO-d_6, 300 MHz) δ 11.57 (s, 1H), 7.48 (ap d, J = 7.75 Hz, 1H), 7.24 (ddd, J= 1.55, 7.72, 7.82 Hz, 1H), 6.88 (ap dd, J = 7.60, 7.60 Hz, 2H), 2.26 (s, 3H). Already synthesized in the literature, spectroscopic data is in accordance with reported data in the following: Adam, W.; Hadjiarapoglou, L.; Mosandi, T.; Saha-Moller, C.R.; Wild, D. *J. Am. Chem. Soc.*, **1991**, *113*, 8005.

8.2.9 Preparation of Ligand IX:

(E)-1-hydroxypropan-2-one oxime (H_2salox-Et)

To a solution of ketone (3.00 g, 20.0 mmol) and sodium acetate (4.91 g, 59.9 mmol) in MeOH (reagent grade, 40 mL) kept under argon with constant stirring was added hydroxylamine hydrochloride (1.53 g, 22.0 mmol). The mixture was heated at 50 °C for 3 hours, and then concentrated under reduced pressure (rotary evaporator and high-vacuum pump) to afford the crude product as a slightly pink solid. The crude was recrystallized from boiling water (20 mL), filtered and collected. Resulting crystals were further purified by trituration with hexanes (3 x 10 mL), filtered, rinsed with small amounts of cold hexanes, and dried on the high vacuum. Oxime, H_2salox-Et, was obtained as a white powder (2.69 g, 81 % yield). TLC *R*f 0.63 (30 % EtOAc/hexane); ^{1}H NMR (DMSO-*d*$_6$, 300 MHz) δ 11.57 (s, 1H), 7.47 (d, J = 7.84 Hz, 1H), 7.23 (dd, J = 7.70, 7.70 Hz, 1H), 6.88 (ap dd, J = 7.53, 7.53 Hz, 2H), 2.79 (q, 7.47 Hz, 2H), 1.08 (t, 7.47 Hz, 3H); ^{13}C NMR (DMSO-*d*$_6$, 75 MHz) δ 162.1, 157.6, 130.1, 127.7, 119.0, 118.1, 116.7, 17.7, 11.0.

8.2.10 Preparation of Ligand X: (E)-2,5-dihydroxy-2,5-dimethylhexan-3-one oxime (H_3oxol)

2,5-Dimethylhex-3-yne-2,5-diol (4.27 g, 30.0 mmol), aqueous NH_2OH (2.76 mL of a 50 wt% solution, 45.1 mmol) and isopropanol (freshly distilled, 30 mL) were added to the reaction vessel. The mixture was heated in a wax bath for 24 hours at 100 °C. After cooling to room temperature, the mixture was concentrated under reduced pressure and recrystallized from hot hexanes. Oxime, H_3oxol, was isolated as clear transparent crystals (2.89 g, 55 % yield); ^{1}H NMR (DMSO-*d*$_6$, 300 MHz) δ

10.57 (s, 1H), 5.74 (s, 1H), 5.55 (s, 1H), 3.35 (s, 1H), 2.60 (s, 1H), 2.10 (s, 1H), 1.25 (s, 1H), 1.15 (s, 6H), 1.15 (s, 6H); IR (film, cm^{-1}) 3412, 2990, 1649, 1630, 1291, 1268, 927, 756; HRMS Calcd for $C_9H_{11}NO_2$ (MH+): 165.07898; Found: 165.0868.

8.2.11 Preparation of Ligand XI: (2E,2'E)-1-(((E)-2-(hydroxyimino)propyl)((Z)-2-(hydroxyimino) propyl)amino)propan-2-one oxime (H_3tri-ox)

An oven dried microwave tube (20 mL), equipped with a magnetic stir bar and a rubber septum was purged with an argon balloon for 5 minutes. Tripropargylamine (2.12 mL, 15.0 mmol), aqueous hydroxylamine (2.3 mL of a 50 wt% solution, 37.5 mmol) and freshly distilled isopropanol (5 mL) were added to the reaction vessel while keeping a constant flow of argon. The rubber septum was replaced by a microwave aluminum cap. The mixture was heated in a Biotage microwave for 2 hours at 130 °C. The crude was concentrated under reduced pressure and azeotroped with isopropanol (4 x 20 mL), until a white powder was obtained. After heating the solid in 15 mL of boiling isopropanol (never fully dissolves), the mixture was cooled in ice, filtered and rinsed with minimum amounts of ice-cooled isopropanol (3 x 5 mL) to afford the oxime, H_3tri-ox, (1.38 g, 40 % yield). (R_f: 0.08 in 5 % MeOH/DCM); ^{1}H NMR (DMSO-d_6, 300 MHz,) δ 10.60 (s, 3H), 2.91 (s, 6H), 1.75 (s, 9H); ^{13}C NMR (DMSO-d_6, 75 MHz) δ 153.48, 57.06, 12.1; IR(film, cm^{-1}) 2964, 2918, 2850, 1698, 1653, 1455; HRMS Calcd for $C_9H_{18}N_4O_3$ (MH+): 230.1379; not found. Calcd for $C_9H_{17}N_4O_2$ (M-OH): 213.1350; found: 213.1351.

8.3 Inorganic Synthesis

8.3.1 Preparation of $[Mn^{IV}_3(dpo)_6]\bullet 2MeCN$, **1**

The reaction of $Mn(ClO_4)_2\bullet 6H_2O$ (0.25 mmol, 91mg) with H_2dpo (0.5 mmol, 121 mg) and Et_3N (0.25 mmol, 35μL) in 10: 10 mL of MeOH: MeCN gave a dark-brown opaque solution. After 4 days, black rectangular crystals suitable for X-ray crystallography were isolated in 45 % yield with respect to Mn. Selected IR (KBr pellet, cm^{-1}): 3451 (br), 3074 (m), 1600 (m), 1501 (m), 1450 (m), 1077 (m), 1026 (s), 1000 (s), 949 (m), 916 (w), 775 (w), 750 (w), 705 (s), 690 (s).

8.3.2 Preparation of $[Mn^{II}(Imz)_4OH][Mn^{IV}_3(Hoxol)_6]\bullet MeCN$, **2**

The reaction of $Mn(ClO_4)_2\bullet 6H_2O$ (0.25 mmol, 91 mg) with H_3oxol (0.5 mmol, 88 mg) and Et_3N (0.25 mmol, 35μL) in 20 mL of MeCN gave a dark-brown opaque solution. While stirring imidazole (1.25 mmol, 85 mg) was added to the solution until dissolution. After two weeks, black needle- like crystals suitable for X-ray crystallography were isolated in 35 % yield with respect to Mn. Selected IR (KBr pellet, cm^{-1}): 3275 (br), 2975 (w), 2934 (s), 1607 (s), 1382 (s), 1179 (m), 1121 (s), 1069 (m), 1048 (m), 968 (s), 869 (s), 757 (s), 691 (s).

8.3.3 Preparation of $[Na[Mn^{IV}_2Mn^{III}(Hoxol)_6]\bullet MeOH\bullet H_2O]_n$, **3**

The reaction of $Mn(CH_3COO)_2\bullet 4H_2O$ (0.25 mmol, 71 mg) with H_3oxol (0.25 mmol, 44 mg) and NaOH (1.0 mmol, 40mg) in 5 mL of MeOH and 10 mL of MeCN gave a dark-brown opaque solution. After one week, black needle- like crystals suitable for X-ray crystallography were isolated in 32 % yield with respect to Mn. Selected IR (KBr pellet, cm^{-1}): 3440 (br), 2975 (m), 2924 (m), 1605 (w), 1465 (w), 1350 (m), 1155 (s), 1118 (s), 1056 (s), 974 (s), 890 (w), 865 (w).

8.3.4 Preparation of $[Mn^{III}_3(\mu_3\text{-}O)(cpo)_3(ClO_4)(MeOH)_3]$, **4**

Reaction of $Mn(ClO_4)_2$•$6H_2O$ (0.25 mmol, 91 mg) and H_2cpo (0.25 mmol, 29 mg) in the presence of Et_3N (0.25 mmol, 35 μL) in 20: 5 mL of MeCN: MeOH. This resulted in a dark brown solution which was stirred for 15 minutes. The solution was filtered and slowly diffused with Et_2O overnight, producing large shiny black cubic crystals in 80 % yield with respect to Mn. Anal. Calcd (Found) for **4** ($C_{24}H_{45}ClMn_3N_3O_{14}$): C, 35.68 (28.12); H, 5.60 (5.69); N, 5.20 (5.79). Selected IR (KBr pellet, cm^{-1}): 3398 (br), 2955 (w), 1613 (m), 1436 (w), 1371 (w), 1117 (s), 1091 (w), 1011 (m), 970 (w), 887 (w), 804 (w), 722 (w).

8.3.5 Preparation of $[Mn^{III}_3(\mu_3\text{-}O)(cpo)_3(ClO_4)(Imz)_3]$, **5**

5 was synthesized in a similar fashion to **4**, however, MeCN was used as the solvent. Imidizole (Imz: 1.25 mmol, 85.0 mg) was added to the reaction mixture and stirred for 30 minutes to yield a dark brown solution, which was then filterted and slowly diffused with Et_2O for 3 days producing cubic crystals in 62 % yield with respect to Mn. Anal. Calcd (Found) for **5** ($C_{30}H_{45}ClMn_3N_9O_{11}$): C, 39.68 (51.29); H, 5.00 (6.90); N, 13.88 (17.91). Selected IR (KBr pellet, cm^{-1}): 3435 (br), 3130 (m), 2970 (m), 1626 (s), 1445 (w), 1129 (s), 1077 (s), 762 (m), 664 (s).

8.3.6 Preparation of $[Mn^{III}_3(\mu_3\text{-}O)(cpo)_3(ClO_4)(Phpy)_3]\bullet 4.5MeCN$, **6**

6 was synthesized in a similar to that of **5** using MeCN as the solvent to dissolve both starting material. 4-phenylpyridine (Phpy: 0.25 mmol, 35 mg) was added to the reaction mixture and stirred for 30 minutes to produce a dark brown solution. After 3 days, black cubic crystals suitable for X-ray were obtained in 70 % yield with respect to Mn. Anal. Calcd (Found) for **6** ($C_{54}H_{60}ClMn_3N_6O_{11}$): C, 47.90 (54.27); H, 4.46 (4.87); N, 6.20 (6.37). Selected IR (KBr pellet, cm^{-1}): 3422 (br), 2950 (w), 2360 (w), 1610 (s), 1419 (m), 1113(s), 1020 (s), 767 (m), 697 (m), 653 (m).

8.3.7 Preparation of $[Mn^{III}_3(\mu_3\text{-}O)(dmo)_3(ClO_4)(MeOH)_3]$, **7**

A dark brown solution resulted from the reaction of $Mn(ClO_4)_2\bullet 6H_2O$ (0.25 mmol, 91 mg), H_2dmo (0.25 mmol, 29 mg), and Et_3N (0.25 mmol, 35 μL) in 20 mL of MeOH. Slow diffusion of Et_2O (3 mL) occurred over a period of one week yielding black cubic crystals in 60 % yield with respect to Mn. Anal. Calcd (Found) for **7** ($C_{18}H_{39}ClMn_3N_3O_{14}$): C, 30.00 (27.80); H, 5.44 (5.53); 5.82 (5.54). Selected IR (KBr pellet, cm^{-1}): 3422 (br), 1611 (m), 1359 (w), 1139 (m), 1122 (m), 1071 (s), 968 (m), 885 (w), 684 (s).

8.3.8 Preparation of $[Mn^{III}_3(\mu_3\text{-}O)(dmo)_3(ClO_4)(EtOH)_3]$, **8**

8 was synthesized in a similar fashion to **7** in which the solvent was replaced by EtOH. Slow diffusion of Et_2O (3 mL) occurred over a period of one week yielded large black cubic crystals with 84 % yield with respect to Mn. Anal. Calcd (Found) for **8** ($C_{21}H_{45}ClMn_3N_3O_{14}$): C, 33.02 (32.69); H, 5.93 (6.14); N, 5.50 (5.39). Selected IR (KBr pellet, cm^{-1}): 3420 (br), 2970 (w), 1613 (m), 1361 (m), 1191 (w), 1113 (s), 1077 (s), 964 (s), 881 (m), 809 (m), 685 (s).

8.3.9 Preparation of $[Mn^{III}_3(\mu_3\text{-}O)(dmo)_3(ClO_4)(Imz)_3]$, **9**

A similar procedure to **7** was used where MeCN (20 mL) was the sole solvent and imidazole (Imz: 1.25 mmol, 85.0 mg) was added after stirring the reaction mixture for 10 minutes. The mixture was then filtered and allowed to stand for 3 days to yield black cubic crystals with 70 % yield with respect to Mn. Anal. Calcd (Found) for **9** ($C_{24}H_{39}ClMn_3N_9O_{11}$): C, 34.73 (34.73); H, 4.73 (4.85); N, 15.19 (15.27). Selected IR (KBr pellet, cm^{-1}): 3421 (br), 3125 (w), 2928 (w), 1615 (m), 1362 (w), 1140 (s), 1072 (s), 974 (m), 757 (w), 674 (s).

8.3.10 Preparation of $[Mn^{III}_3(\mu_3\text{-}O)(salox\text{-}H)_3(ClO_4)(Phpy)_3]$, **10**

Reaction of $Mn(ClO_4)_2 \cdot 6H_2O$ (0.25 mmol, 91 mg) and H_2salox-H (0.25 mmol, 40 mg) in the presence of Et_3N (0.25 mmol, 35 μL) in 25 mL of MeCN afforded a dark green solution to which 4-phenylpyridine (Phpy: 0.25 mmol, 35 mg) was added and stirred for 30 minutes. The dark solution was then filtered and slowly diffused with Et_2O overnight to produce large shiny black cubic crystals with 75 % yield with respect to Mn. Anal. Calcd (Found) for **10** ($C_{54}H_{42}ClMn_3N_6O_{11}$): C, 56.34 (53.29); H, 3.67 (3.65); N, 7.30 (6.85). Selected IR (KBr pellet, cm^{-1}): 3420 (br), 3037 (w), 1605 (s), 1537 (m), 1445 (s), 1294 (s), 1201 (m), 1062 (s), 923 (s), 678 (s).

8.3.11 Preparation of $[Mn^{III}_3(\mu_3\text{-}O)(salox\text{-}Me)_3(ClO_4)(Phpy)_3]\cdot 0.5MeCN$, **11**

11 were synthesized in a similar fashion to **10**, where H_2salox-H was replaced with H_2salox-Me (0.25 mmol, 40 mg) resulting in a dark green solution to which 4-phenylpyridine (Phpy: 0.25 mmol, 35 mg) was added and stirred for 30 minutes. The resulting reaction mixture was allowed to slowly diffuse with Et_2O yielding dark cubic crystals with a 79 % yield with respect to Mn. Anal. Calcd (Found) for **11** ($C_{58}H_{49.5}ClMn_3N_{6.5}O_{11}$): C, 57.39 (56.45); H, 4.11 (4.12); N, 7.50 (7.46). Selected IR (KBr pellet, cm^{-1}): 3420 (br), 1595 (s), 1525 (s), 1430 (s), 1320 (s), 1245 (w), 1140 (m), 1070 (s), 965 (m), 765 (s), 670 (m).

8.3.12 Preparation of $[Mn^{III}_4Mn^{IV}_2(salox\text{-}Et)_6(\mu_3\text{-}O)_2(\mu_3\text{-}MeO)_2(\mu\text{-}MeO)_2(MeOH)_2]$, **12**

Reaction of $Mn(Cl)_2\cdot 4H_2O$ (0.75 mmol, 147 mg) and H_2salox-Et (1.00 mmol, 168 mg) in the presence of Et_3N (0.75 mmol, 105 μL) in 15: 5 mL of MeOH: DMF afforded a dark black solution. The dark green solution was filtered and slowly diffused with Et_2O for seven days yielding 30 % shiny brown cubic crystals with respect to Mn. Selected IR (KBr pellet, cm^{-1}): 3445 (br), 2916 (m), 536 (s), 1431 (m), 1304 (m), 1254 (s), 1132 (m), 1107 (m), 1000 (m), 951 (m), 858 (s), 761 (m), 668 (m).

8.3.13 Preparation of $[Mn^{III}_4Mn^{IV}_2(salox\text{-}Et)_6(\mu_3\text{-}O)_2(\mu_3\text{-}MeO)_2(\mu\text{-}MeO)_2(DMF)_2]\cdot MeOH$, **13**

Reaction of $Mn(ClO_4)_2\cdot 6H_2O$ (0.25 mmol, 91 mg) and H_2salox-Et (0.25 mmol, 42 mg) in the presence of Et_3N (0.25 mmol, 35 μL) in 15: 5 mL of MeCN: MeOH afforded a dark black solution. The dark black solution was filtered and slowly diffused with Et_2O for over a week yielding 25 % black plate-like crystals with respect to Mn. Selected IR (KBr pellet, cm^{-1}): 3445 (br), 2940 (w), 1650 (s), 1590 (m), 1564 (w), 1520 (w), 1430 (m), 1375 (w), 1310 (s), 1250 (w), 1138 (m), 1098 (s), 1031 (w), 938 (s), 860 (w), 750 (s), 680 (m).

8.3.14 Preparation of $[Mn^{III}_6Mn^{IV}(\mu_3\text{-}O)_2(cpo)_6(diol)_3]$, **14**

Reaction of $Mn(CH_3COO)_2{\bullet}4H_2O$ (0.25 mmol, 71 mg) and H_2cpo (0.25 mmol, 29 mg) in the presence of Et_3N (0.25 mmol, 35 μL) in 10 mL of DMF. To this solution, 1,2 diol (1.25 mmol, 70 μL) was added dropwise. This resulted in a dark brown solution which was stirred for 15 minutes. The solution was filtered and slowly diffused with Et_2O overnight, producing large shiny black cubic crystals in 55 % yield with respect to Mn. Selected IR (KBr pellet, cm^{-1}): 3456 (br), 2929 (m), 1613 (m), 1436 (w), 1371 (w), 1117 (s), 1091 (w), 1011 (m), 970 (w), 887 (w), 804 (w), 722 (w).

8.3.15 Preparation of $[Mn^{III}_6Mn^{IV}(\mu_3\text{-}O)_2(cpo)_6(diol)_3(MeOH)_2(H_2O)_2]$, **15**

Reaction of $Mn(CH_3COO)_2{\bullet}4H_2O$ (0.50 mmol, 142 mg) and H_2cpo (0.25 mmol, 29 mg) in the presence of Et_3N (0.25 mmol, 35 μL) in 10 mL of MeOH. Once dissolved, 15 mL of MeCN and 1,2 diol (1.25 mmol, 70 μL) was added dropwise to the solution. This resulted in a dark brown solution which was stirred for 5 minutes. The solution was filtered and slowly diffused with Et_2O overnight, producing large shiny black hexagonal crystals in 61 % yield with respect to Mn. Selected IR (KBr pellet, cm^{-1}): 3435 (br), 2954 (w), 1625 (w), 1429 (w), 1387 (w), 1180 (w), 1043 (s), 1018 (s), 971 (w), 900 (w), 654 (s).

8.3.16 Preparation of $[Mn^{III}_6Mn^{IV}(\mu_3\text{-}O)_2(cpo)_6(diol)_3(benzIm)_2]\cdot 4MeCN$, **16**

Reaction of $Mn(ClO_4)_2\cdot 6H_2O$ (0.25 mmol, 91 mg) and H_2cpo (0.25 mmol, 29 mg) in the presence of Et_3N (0.25 mmol, 35 μL) in 20 mL of MeCN. This resulted in a dark brown solution which was stirred for 5 minutes until dissolution. To this solution 1,2 diol (1.25 mmol, 70 μL) and benzimidazole (benzIm: 1.25 mmol, 148mg) was added sequentially and allowed to stir for an additional 5 minutes. Finally, the solution was filtered and slowly diffused with Et_2O overnight, producing large shiny black cubic crystals in 45 % yield with respect to Mn. Selected IR (KBr pellet, cm^{-1}): 3440 (br), 2960 (m), 2840 (m), 1600 (m), 1490 (w), 1425 (m), 1362 (m), 1300 (w), 1263 (w), 1175 (w), 1108 (s), 1046 (s), 1015 (s), 901 (s), 741 (s).

8.3.17 Preparation of $[Mn^{III}_6Mn^{IV}(\mu_3\text{-}O)_2(dpo)_6(diol)_3(MeOH)_2]\cdot 4MeOH$, **17**

Reaction of $Mn(ClO_4)_2\cdot 6H_2O$ (0.25 mmol, 91 mg) and H_2dpo (0.25 mmol, 60 mg) in the presence of Et_3N (0.75 mmol, 105 μL) and 1,2 diol (1.25 mmol, 70 μL) in 30 mL of MeOH resulted in a dark brown solution which was stirred for 15 minutes. The solution was filtered and slowly diffused with Et_2O overnight, producing large shiny black hexagonal crystals in 40 % yield with respect to Mn. Selected IR (KBr pellet, cm^{-1}): 3440 (br), 1600 (m), 1486 (m), 1444 (m), 1356 (m), 1096 (s), 1080 (m), 1040 (s), 1000 (m), 951 (m), 894 (m), 784(s), 761(s), 704(s), 664(s).

8.3.18 Preparation of $[Mn^{II}_2Mn^{III}_{18}(\mu_3\text{-}O)_6(cpo)_{18}Mn^{IV}_3(C_2H_4O_2)_{13}(MeCN)_4(H_2O)_6]^{2+}\bullet[(MeOH)(MeCN)(C_2H_6O_2)]$, **18**

Reaction of $Mn(ClO_4)_2\bullet6H_2O$ (0.50 mmol, 182 mg) and H_2cpo (0.25 mmol, 29 mg) in the presence of Et_3N (0.75 mmol, 105 μL) and 1,2 diol ($C_2H_6O_2$: 1.25 mmol, 70 μL) in 15: 5 mL of MeOH: MeCN resulted in a dark brown solution. The solution was filtered and slowly diffused with Et_2O overnight, producing black hexagonal crystals in 20 % yield with respect to Mn. Selected IR (KBr, cm^{-1}): 3440 (br), 1600 (m), 1486 (m), 1444 (m), 1356 (m), 1096 (s), 1080 (m), 1040 (s), 1000 (m), 951 (m), 894 (m), 784(s), 761(s), 704(s), 664(s).

8.3.19 Preparation of $[Mn^{III}_9(\mu_3\text{-}O)(\mu_4\text{-}O)_3(\text{salox-Me})_6(MeO)_3(CH_3COO)_3(H_2O)_3]^+$, **19**

Reaction of $Mn(CH_3COO)_2\bullet4H_2O$ (0.25 mmol, 91 mg) and H_2salox-Me (0.25 mmol, 38 mg) in the presence of Et_3N (0.25 mmol, 35 μL) in 15: 5 mL of MeCN: MeOH afforded a dark green solution. The dark green solution was filtered and slowly diffused with Et_2O for over 3 nights yielding 45 % shiny black cubic crystals. Selected IR(KBr pellet, cm^{-1}): 3400bw, 2900w, 1550s, 1440s, 1320s, 1240m, 1150w, 1050m, 1000m, 950m, 850m, 740m and 680s.

8.3.20 Preparation of $[Mn^{III}_9(\mu_3\text{-}O)(\mu_4\text{-}O)_3(\text{salox-Me})_6(MeO)_3(CH_3COO)_6(MeOH)_2(Phpy)]^+$, **20**

Reaction of $Mn(CH_3COO)_2\bullet4H_2O$ (0.25 mmol, 91 mg) and H_2salox-Me (0.25 mmol, 38 mg) in the presence of Et_3N (0.25 mmol, 35 μL) in 15: 5 mL of MeCN: MeOH afforded a dark green solution. Phenylpyridine (Phpy: 0.25 mmol, 35 mg) was added to the solution while stirring. The dark green solution was filtered and slowly diffused with Et_2O for over 3 nights yielding 40 % shiny black hexagonal crystals. Selected IR (KBr pellet, cm^{-1}): 3450 (br), 1560 (s), 1440 (s), 1308(s), 1250 (m), 1125 (m), 1052 (s), 1025 (s), 980 (s), 871 (m), 758 (m), 758 (m), 678(s).

8.3.21 Preparation of $[Mn^{III}_{18}(\mu_3\text{-}O)_2(\mu_4\text{-}O)_6(\text{salox-Et})_{12}(CH_3COO)_9(OCH_3)_6Cl]$, **21**

Reaction of $Mn(CH_3COO)_2{\bullet}4H_2O$ (0.25 mmol, 91 mg) and H_2salox-Et (0.25 mmol, 42 mg) in the presence of Et_3N (0.25 mmol, 35 μL) in 15: 5 mL of MeCN: MeOH afforded a dark green solution. The dark green solution was filtered and slowly diffused with Et_2O for over 3 nights yielding 35 % shiny black cubic crystal. Selected IR (KBr pellets, cm^{-1}): 3425 (br), 1557 (s), 1525 (m), 1439(s), 1320 (m), 1255 (w), 1136 (w), 1060 (m), 1017 (m), 950 (m), 857 (m), 760 (m), 680(s), 661(s).

Chapter 9

9.1 Crystal Structure Data

	1	**2**	**3**
Formula	$C_{94}H_{90}Mn_3N_6O_{14}$	$C_{62}H_{110}Mn_4N_{14}O_{21}$	$C_{49}H_{96.5}Mn_3N_6NaO_{20.25}$
FW, g mol^{-1}	1692.54	1607.40	1281.63
crystal system	Monoclinic	Orthorhombic	Monoclinic
space group	P2(1)/n	Pbcn	P 2(1)/c
T, K	202(2)	203(2)	200(2)
λ, Å	0.71073	0.71073	0.71073
a, Å	19.684(12)	17.366(6)	21.961(4)
b, Å	13.141(8)	24.340(9)	23.236(4)
c, Å	32.695(19)	20.909(8)	14.024(2)
α, °	90	90	90
β, °	102.86	90	90.26
γ, °	90	90	90
V, Å^3	8245(8)	8838(5)	7156(2)
Z	4	4	4
ρ_{calcd}, g cm^{-3}	1.364	1.208	1.190
μ (Mo, Kα), mm^{-1}	0.522	0.625	0.591
F(000)	3532	3392	2722
measd/indep	43974/ 11793	5382/ 60873	7264/ 31666
(R_{int}) reflns	(0.2099)	(0.2607)	(0.1637)
[a]$R1(I > 2\sigma(I))$	0.0764	0.0995	0.1044
[b]$wR2\ (I > 2\sigma(I))$	0.1685	0.2584	0.2441
GOF on F^2	0.959	1.045	1.060
$\triangle\rho_{\text{max,min}}$, e Å^3	0.531, -0.445	1.245, -0.476	1.422, -0.440

	4	**5**	**6**
Formula	$C_{24}H_{45}ClMn_3N_3O_{14}$	$C_{30}H_{45}ClMn_3N_9O_{11}$	$C_{54}H_{60}ClMn_3N_6O_{11}$
FW, g mol^{-1}	807.90	908.02	1354.09
crystal system	trigonal	hexagonal	hexagonal
space group	R-3c	P31c	R-3
T, K	203(2)	201(2)	203(2)
λ, Å	0.71073	0.71073	0.71073
a, Å	14.267(4)	14.819(2)	16.520(12)
b, Å	14.267(4)	14.819(2)	16.520(12)
c, Å	55.852(17)	10.320(2)	42.037(6)
α, °	90	90	90
β, °	90	90	90
γ, °	120	120	120
V, $Å^3$	9845(5)	1962.7(6)	9935.0(17)
Z	12	2	6
ρ_{calcd}, g cm^{-3}	1.635	1.536	1.358
μ (Mo, Kα), mm^{-1}	1.289	1.085	0.669
F(000)	5016.0	936	4230.0
measd/indep	24087/1931	20032/2699	31583/4047
(R_{int}) reflns	(0.1161)	(0.0832)	(0.1006)
$^{a}R1(I > 2\sigma(I))$	0.0506	0.0603	0.0529
$^{b}wR2\ (I > 2\sigma(I))$	0.1235	0.1474	0.1226
GOF on F^2	1.080	1.134	1.115
$\triangle\rho_{max,min}$, e $Å^3$	1.070, -0.400	1.093, -0.560	0.514, -0.607

	7	**8**	**9**
Formula	$C_{18}H_{39}ClMn_3N_3O_{14}$	$C_{21}H_{45}ClMn_3N_3O_{14}$	$C_{24}H_{39}ClMn_3N_9O_{11}$
FW, g mol^{-1}	721.29	763.87	829.91
crystal system	trigonal	hexagonal	monoclinic
space group	R-3	R-3	P2(1)/c
T, K	201(2)	202(2)	200(2)
λ, Å	0.71073	0.71073	0.71073
a, Å	13.9638(7)	13.875(14)	10.094(14)
b, Å	13.9638(7)	13.875(14)	18.670(3)
c, Å	26.825(3)	28.707(6)	18.891(3)
α, °	90	90	90
β, °	90	90	92.13(2)
γ, °	120	120	90
V, Å^3	4529.8(6)	4786.2(12)	3557.5(9)
Z	6	6	4
ρ_{calcd}, g cm^{-3}	1.588	1.590	1.550
μ (Mo, Kα), mm^{-1}	1.389	1.319	1.189
F(000)	2232.0	2376	1704
measd/indep	11947/1774	12499/2022	37083/7320
(R_{int}) reflns	(0.0531)	(0.0730)	(0.0578)
$^aR1(I > 2\sigma(I))$	0.0365	0.0418	0.0479
$^bwR2\ (I > 2\sigma(I))$	0.0862	0.0911	0.1208
GOF on F^2	1.078	1.046	1.048
$\triangle\rho_{max,min}$, e Å^3	0.520, -0.255	0.503,-0.330	0.668, -0.444

	10	**11**	**12**
Formula	$C_{54}H_{42}ClMn_3N_6O_{11}$	$C_{58}H_{49.5}ClMn_3N_{6.5}O_{11}$	Res file.
FW, g mol^{-1}	1151.21	1213.81	
crystal system	hexagonal	hexagonal	
space group	P-3	P-3	P-1
T, K	203(2)	203(2)	203(2)
λ, Å	0.71073	0.71073	0.71073
a, Å	15.869(14)	12.944(15)	11.785(3)
b, Å	15.869(14)	12.944(15)	12.703(4)
c, Å	12.997(9)	18.544(4)	23.534(7)
α, °	90	90	92.93
β, °	90	90	94.48
γ, °	120	120	98.18
V, Å^3	2835(4)	2690.9(8)	3469.59
Z	2	2	6
ρ_{calcd}, g cm^{-3}	1.349	1.498	
μ (Mo, Kα), mm^{-1}	0.766	0.812	
F(000)	1176	1246	
measd/indep	24797/3014	27170/3427	
(R_{int}) reflns	(0.0795)	(0.0798)	
$^{a}R1(I > 2\sigma(I))$	0.0607	0.0491	
$^{b}wR2\ (I > 2\sigma(I))$	0.1605	0.1183	
GOF on F^2	1.067	1.063	
$\triangle\rho_{max,min}$, e Å^3	0.826, -0.479	0.628, -0.281	

	13	**14**	**15**
Formula	$C_{65}H_{84}Mn_6N_8O_{21}$	$C_{48}H_{78}Mn_7N_6O_{20}$	$C_{54}H_{60}ClMn_3N_6O_{11}$
FW, g mol^{-1}	1645.06	1443.74	
crystal system	triclinic	Hexagonal	hexagonal
space group	P-1	R-3c	C 2/c
T, K	203(2)	199(2)	203(2)
λ, Å	0.71073	0.71073	0.71073
a, Å	11.2069(14)	12.6859(15)	14.631(4)
b, Å	12.2430(15)	12.6859(15)	25.405(6)
c, Å	13.3115(16)	63.028(14)	21.353(5)
α, °	78.059(2)	90	90
β, °	86.856(2)	90	103.143
γ, °	87.717(2)	120	90
V, Å^3	1783.4(4)	8784(2)	7729.02
Z	1	6	
ρ_{calcd}, g cm^{-3}	1.532	1.638	
μ (Mo, Kα), mm^{-1}	1.108	1.537	
F(000)	850	4458	
measd/indep	18396/6273	1717/ 25809	
(R_{int}) reflns	(0.0930)	(0.0831)	
$^aR1(I > 2\sigma(I))$	0.0778	0.0680	
$^bwR2(I > 2\sigma(I))$	0.1975	0.1593	
GOF on F^2	1.053	1.198	
$\triangle\rho_{max,min}$, e Å^3	1.408, -0.723	0.622, -0.935	

	16	**17**	**18**
Formula	$C_{74}H_{108}Mn_7N_{16}O_{20}$	$C_{102}H_{114}Mn_7N_6O_{26}$	$C_{168}H_{108}Cl_4Mn_{23}N_{24}O_{96}$
FW, g mol^{-1}	1926.34	2224.57	
crystal system	Monoclinic	Hexagonal	Monoclinic
space group	C2/c	R-3	C2/c
T, K	203(2)	203(2)	203(2)
λ, Å	0.71073	0.71073	0.71073
a, Å	15.251(7)	17.731(3)	14.7751(17)
b, Å	26.585(12)	17.731(3)	25.645(5)
c, Å	22.133(10)	57.581(12)	62.786(7)
α, °	90	90	90
β, °	100.148(6)	90	90.085(2)
γ, °	90	120	90
V, Å^3	8833(7)	15677(5)	23790.1
Z	4	6	4
ρ_{calcd}, g cm^{-3}	1.448	1.414	
μ (Mo, Kα), mm^{-1}	1.042	0.894	
F(000)	3996	6906	
measd/indep	40041/7490	42774/4977	
(R_{int}) reflns	(0.1329)	(0.1610)	
$^aR1(I > 2\sigma(I))$	0.0953	0.0894	
$^bwR2\ (I > 2\sigma(I))$	0.2142	0.2117	
GOF on F^2	1.122	1.108	
$\triangle\rho_{max,min}$, e Å^3	0.958, -0.539	1.539, -0.869	

	19	**20**	**21**
Formula	Res. file	$C_{76}H_{86}Mn_9N_9O_{29}$	Res. file
FW, g mol^{-1}		2084.0	
crystal system		triclinic	
space group		P-1	R-3c
T, K	203(2)	200(2)	203(2)
λ, Å	0.71073	0.71073	0.71073
a , Å	25.8156(18)	13.291(5)	22.55(3)
b , Å	25.8156(18)	14.113(5)	22.55(3)
c , Å	25.8156(18)	24.614(9)	57.64(9)
α , °	90	91.540(5)	90
β , °	90	102.652(5)	90
γ , °	90	107.976(5)	90
V, Å^3	17204.7	4263(3)	25388.2
Z		2	
ρ_{calcd}, g cm^{-3}		1.536	
μ (Mo, Kα), mm^{-1}		1.085	
F(000)		936	
measd/indep		40663/14983	
(R_{int}) reflns		(0.1779)	
$^aR1(I > 2\sigma(I))$		0.0766	
$^bwR2\ (I > 2\sigma(I))$		0.1452	
GOF on F^2		0.946	
$\triangle\rho_{max,min}$, e Å^3		1.194, -0.778	

References

1 (a) Gatteschi, D.; Caneschi, A.; Pardi, L.L; Sessoli, R.; *Science*, **1994**, 265, 1054. (b) Kahn, O.; Martinez, C.J.; *Science*, **1998**, 279, 44. (c) Karotsis, G.; Evangelisti, M.; Dalgarno, S.J.; Brechin, E.K., *Angew. Chem. Int. Ed.*, **2009**, 48, 9928. (d) Ritchie, C.; Ferguson, A.; Nojiri, H.; Miras, H.N.; Song, Y-F.; Long, D-L.; Burkholder, E.; Murrie, M.; K'gerler, P.; Brechin, E.K.; Cronin, L., *Angew. Chem. Int. Ed.*, **2008**, 47, 5609.

2 (a) Ilios, C.J.; Vinslava, A; Wernsdorfer, W.; Moggach, S.; Parsons, S.; Perlepes, S.P.; Christou, G.; and Brechin E.K., *J. Am. Chem. Soc.*, **2007**, 129, 2754. (b) Wang, G.; Zhu, H.; Fan, J.; Slebodnick, C., Yee G.T., *Inorg. Chem.*, **2006**, 45, 1406.

3 (a) Christou, G., *Acc. Chem. Res.*, **1989**, 22, 328. (b) Christou, G., *Polyhedron*, **2005**, 24, 2065.

4 Vincent, J. B.; Folting, K.; Gatteschi, D.; Christou, G.; Hendrickson, D. N., *J. Am. Chem. Soc.* **1993**, 115, 1804.

5 (a) Armstrong, F.A., *Phil. Trans. R. Soc. B*, **2008**, 363, 1263. (b) Spiro, T.G.; Bargar J.R., Sposito, G.; Tebo, B.M., *Chemical Research*, **2010**, 43, 4.

6 Wispes, J.R.; Barbara, B.; Warner J.; Chitta, R. C.; Neuman, D.J.; Glasser, S.W., Rapog, D.C, Changg, L-Y.; Whitsett, J.A., *The Journal of Biological Chemistry*, **1992**, 33, 23937.

7 Leslie, M.; *Science*, **2009**, 323, 1286.

8 (a) Ferreira, K.N.; Iverson, T.M.; Maghlaoui, K.; Barber, J.; Iwata, S., *Science*, **2004**, 303, 1831. (b) McEvoy, J.P.; Brudvig, G.W.; *Chem. Rev.*, **2006**, 106 ,4455.

9 Loll, B.; Kern, J.; Saenger, W.; Zouni, A.; Biesiadka, J., *Nature*, **2005**, 438, 1040

10 Yano, J.; Kern, J.; Sauer, K.; Latimer, M.J.; Pushkar, Y.; Biesiadka, Y.; Loll, B.; Saenger, W.; Messinger, J.; Zouni, A.; Yachandra, V.K., *Science*, **2006**, 314, 821

11 Miller, J.S.; Epstein, A.J., *Molecule-Based Magnetic Materials*, ACS Symposium Series, 1996.

12 Kahn, O., *Molecular Magnetism*, Wiley, Weinheim, 1993.

13 Milios, C.J.; Vinslava, A.; Wernsdorfer, W.; S. Moggach, S.; Parsons, S.; Perlepes, S.P.; Christou, G.; Brechin, E.K., *J. Am. Chem. Soc.*, **2007**, 129, 2754.

14 (a) Christou, G.; Gatteschi, D.; Hendrickson, D. N.; Sessoli, R., *MRS Bulletin* **2000**, *25*, 66. (b) Thomas, L.; Lionti, L.; Ballou, R.; Gatteschi, D.; Sessoli, R.; Barbara, B., *Nature,* **1996**, *383*, 145.

15 Sessoli, R.; Ysai, H-L.; Schake, A.R.; Wang, S.; Vincent, J.B.; Folting, K.; Gatteschi, D.; Christou, G.; Hendrickson, D.N., *J. Am. Chem. Soc.,* **1993**, 115, 1804.

16 (a) Beauchemin, A.M.; Moran, J.; Lebrun, M.; Seguin, C.; Dimitrijevic, E.; Zhang, L.; Gorelsky, S.I., *Angew. Chem. Int. Ed.*, **2008**, 47, 1410. (b) Moran, J.; Gorelsky, S.I.; Dimitrijevic, E.; Lebrun, M-E.; Bedard, A-C.; Seguin, C.; Beauchemin, A.M., *J. Am. Chem. Soc.*, **2008**, 130, 17893.

17 Barlow, W., *Nature*, **1883**, 29, 205.

18 Mukhopadhyay, S.; Mandal, S.K.; Bhaduri, S.; Armstrong, W.H., *Chem. Rev.*, **2004**, 104, 3981.

19 Pathmalingam, T.; Gorelsky, S.I.; Bedard, A-C.; Burchell, T.J.; Beauchemin, A.; Clerac, R.; Murugesu, M., *Chem. Commun.*, **2008**, 2782.

20 (a) Price, D.J.; Batten, S.R.; Berry, K.J.; Moubaraki B.; Murray, K.S., *Polyhedron*, **2003**, 22, 165. (b) Johnson, B.F.G.; Sieker, A.; Blake A.J.; Winpenny, R.E.P., *J. Am. Chem. Soc.*, **1993**, 1345. (c) Birkelbach, F.; Florke, U.; Haupt, H.J.; Butzlaff, C.; Trautwein, A.X.; Wieghardt, K.; Chaudhuri, P., *Inorg. Chem.*, **1998**, 37, 2000.

21 Frisch, M. J. *et al., Gaussian 03, Revision C.01*, Gaussian, Inc.: 2003.

22 (a) Myers, B.E.; Berger, L.; Friedberg, S.J., *J. Appl. Phys.*, **1969**, 40, 1149. (b) O'Connor, C.J., *Prog. Inorg. Chem.*, **1982**, 29, 203.

23 J. H. van Vleck, *The Theory of Electric and Magnetic Susceptibility*, Oxford University Press, Oxford, 1932.

24 Kambe, K., *J. Phys. Soc. Jpn.* **1950**, 5, 48.

25 Scott, R.T.W.; Parsons, S.; Murugesu, M.; Wernsdorfer, W.; Christou, G.; Brechin, E.K., *Chem. Commun.*, **2005**, 2083.

26 (a) Vincent, J.B.; Chang, H-R.; Folting, K.; Huffman, J.C.; Hendrickson, D.N., *J. Am. Chem. Soc.* **1987**, 109, 5703. (b) Milios, C.J.; Wood, P.A.; Parsons, S.; Foguet-Albiol, D., Lampropoulos, C.; Christou, G.; Perlepes, S.P.; Brechin, E.K., *Inorganica Chimica Acta*, **2007**, 360, 3932. (c) Stoumpos, C.C., Inglis, R., Karotsis, G., Jones, L.F., Collins, A., Parsons, S., Milios, C.J., Papaefstatiou, G.S., Brechin, E.K., *Crystal Growth and Design*, **2009**, 9, 24. (d) Inglis, R.; Jones,L.F.; Mason, K.; Collins, A.; Moggach, S.A.; Parsons, S.; Perlepes, S.P.; Wernsdorfer, W.; Brechin, E.K., *Chem. Eur. J.* **2008**, 14, 9117. (e) Jones, L.F.; Rajaraman, G.;

Brockman, J.; Murugesu, M.; Sanudo, E.C.; Raftery, J.; Teat, S.J.; Wernsdorfer, W.; Christou, G.; Brechin, E.K.; Collison, D., *Chem. Eur. J,*. **2004**, 10, 5180. (f) Stamatatos, T.C.; Foguet-Albiol, D.; Lee, S-C.; Stoumpos, C.C.; Raptopoulou, C.P.; Terzis, A.; Wernsdorfer, W.; Hill, S.O.; Perlepes, S.P.; Christou, G., *J. Am. Chem. Soc.* **2007**, 129, 9484. (g) McCusker, J.K.; Jang, H.G.; Wang, S.; Christou, G.; Hendrickson, D.N., *Inorg. Chem.* **1992,** 31, 1874.

27 (a) Stamatatos, T.C.; Foguet-Albiol, D.; Stoumpos, C.C.; Raptopoulou, C.P.; Terzis, A.; Wernsdorfer, W.; Perlepes, C.P.; Christou, G., *J. Am. Chem. Soc.* **2005**, 127, 15380. (b) Inglis, R.; Jones, L.F.; Karotsis, G.; Collins, A.; Parsons, S.; Perlepes, S.P.; Wernsdorfer, W.; Brechin, E.K., *Chem. Commun.* **2008**, 5924. (c) Yang, C-I.; Wernsdorfer, W.; Cheng, K-H.; Nakano, M.; Lee, G-H.; Tsai, H-L., *Inorg. Chem.* **2008**, 47, 10184. (d) Lampropoulos, C.; Abboud, K.A.; Stamatatos, T.C.; Christou, G., *Inorg. Chem.* **2009**, 48, 813. (e) Feng, P.L.; Koo, C.; Henderson, J.J.; Nakano, M.; Hill, S.; Barco, E.D.; Hendrickson, D.N., *Inorg. Chem.* **2008**, 47, 8610.

28 (a)Sessoli, R.; Ysai, H-L.; Schake, A.R.; Wang, S.; Vincent, J.B.; Folting, K.; Gatteschi, D.; Christou, G.; Hendrickson, D.N., *J. Am. Chem. Soc.*, **1993**, 115, 1804. (b) Brechin, E.K.; Soler, M.; Davidson, J.; Hendrickson, D.N.; Parsons, S.; Christou, G., *Chem. Commun.*, **2002**, 2252. (c) Murugesu, M.; Wernsdorfer, W.; Abboud, K.A.; Christou, G., *Angew. Chem. Int. Ed.,* **2005**, 44, 892. (d) Murugesu, M.; Raftery, J.; Wernsdorfer, W.; Christou, G.; Brechin, E.K., *Inorg. Chem.,* **2004**, 43, 4203. (e) Murugesu, M.; Habrych, M.; Wernsdorfer, W.; Abboud K.A.; Christou, G., *J. Am. Chem. Soc.,* **2004**, 126, 4766. (f) Jones, L.F.; Rajaraman, G.; Brockman, J.; Murugesu, M.; Sanudo, E.C.; Raftery, J.; Teat, S.J.; Wernsdorfer, W.; Christou, G.; Brechin, E.K.; Collison, D., *Chem. Eur. J.,* **2004**, 10, 5180. (g) Soler, M.; Rumberger, E.; Folting, K.; Hendrickson, D.N.; Christou, G., *Polyhedron,* **2001**, 20, 1365.

29 Cano, J.; Cauchy, T.; Ruiz, E.; Milios, C.J.; Stoumpos, C.C.; Stamatatos, T.C.; Perlepes, S.P.; Christou, G.; Brechin, E.K., *Dalton Trans.*, **2008**, 234.

30 (a) Myers, B.E.; Berger L.; Friedberg, S., *J. Appl. Phys.* **1969**, *40*, 1149. (b) O'Connor, C. J., *Prog. Inorg. Chem.,* **1982**, *29*, 203.

31 R. Boca, *Theoretical Foundations of Molecular Magnetism*, Elsevier Ed, 1999.

32 (a) Borrás-Almenar, J. J.; Clemente-Juan, J. M.; Coronado, E.; Tsukerblat, B. S., *Inorg. Chem.,* **1999**, 38, 6081. (b) Borrás-Almenar, J. J.; Clemente-Juan, J. M.; Coronado, E.; Tsukerblat, B. S., *J. Comput. Chem.,* **2001**, 22, 985.

33 Xu H-B.; Wang B-W.; Pan F.; Wang Z-M.; Gao S., *Angew. Chem. Int. Ed.,* **2007,** *46*, 7388.

34 Milios, C.J.; Piligkos, S.; Brechin, E.K., *Dalton Trans.*, **2008**, 1809.

Acknowledgement

First of all,

I would like to formally thank Fatemah Habib from the bottom of my heart for being a good friend and a great colleague. She has worked alongside me on various projects, more specifically, the Mn_3 triangle project and I would like to thank her for her great contributions and effort.

Po-Heng Lin has been a great moral support in and outside the lab, you are a great friend to have around. I would like to thank the Murugesu lab members, Jerome Long, Didier Savard, Maxim Hajek, Frederick Perras and Ahmed Farghal for their support as well. I would like to especially thank Mohammed Rashid and Melanie Brulotte for working on my projects.

A special thanks to Anne-Catherine Bedard, Francis Loiseau and Andre Beauchemin for their collaborations and providing us with the organic materials to conduct the inorganic syntheses.

These results would be next to impossible without the help of our X-ray crystallographers Tara Burchell and Ilia Korobkov whom we dearly depend on for crystal structures.

I would like to thank Rodolphe Clerac for all the magnetic measurements and his analyses.

Serge Gorelsky has conducted all of the DFT calculations and I would like to thank him for his insights regarding various projects, especially the Mn_3 project.

I would like to thank Cory M. Widdifield and David L. Bryce for conducting solid-state NMR on the $NaCo_2$ compound.

Most importantly, I would like to thank my supervisor, Muralee Murugesu for giving me the opportunity to pursue my graduate studies. This would not be possible without your supervision and support.

Finally, I would like thank my love, Thivisha for her support and encouragement throughout this graduate program.